Effects of Biochar Electrode Structure, Dimension, and Surface Properties on Electrochemical Double-Layer Capacitor Performance

by

Daniel Alexander Yanchus

A thesis submitted in conformity with the requirements
for the degree of Master of Applied Science
Department of Chemical Engineering and Applied Chemistry
University of Toronto

Effects of Biochar Electrode Structure, Dimension, and Surface Properties on Electrochemical Double-Layer Capacitor Performance

Daniel Alexander Yanchus
Master of Applied Science
Department of Chemical Engineering and Applied Chemistry
University of Toronto
2017

Abstract

Supercapacitors, or electrochemical double-layer capacitors (EDLCs), are high power density storage devices that are able to complement or replace conventional batteries in niche energy storage situations. This thesis investigates the characterization and performance of monolithic biochar, produced from woody-biomass precursors, as an alternative supercapacitor electrode material in three parts. First, the electron deceleration scanning electron microscope technique is applied to biochar specimens, enabling the clear resolution of nanoscale surface features and their locations within the biomass precursor. Second, monolithic biochar electrodes are compared to their powder thin film structured counterparts, demonstrating equivalent device specific capacitance performances while electrode thickness increases up to 5 mm. Third, the influence of pyrolysis conditions on electrochemical performance is explored, revealing that while increasing the temperature improves conductivity and microporosity development, capacitive storage is hindered. Although capacitive performance appears relatively low, monolithic biochar's unique structure and associated capabilities afford future opportunities as an electrode material.

Acknowledgements

To my supervisors, Professor Don Kirk and Professor Charles Jia – I cannot thank you enough for your continuous guidance, patience, and support over the past two years. I always come away from our meetings with new perspectives and ideas that reinvigorate my interest for this field; it has been a lot of fun working together.

A special thank you to PhD candidate and group member Johnathon Caguiat for the time spent helping me understand complex problems, and doing so much of the initial legwork in this field before I arrived. I would also like to thank Professor Shitang Tong for his optimism, research suggestions, and support in the lab. Debby Repka, your contagious passion for better writing will be appreciated by all those who read this thesis.

I'd like to recognize Sal Boccia and Dr. Rana Sodhi, as well as the Department of Materials Science and Engineering, and the Ontario Centre for the Characterization of Advanced Materials for their assistance with microscopy and x-ray photoelectron spectroscopy analyses, respectively. A big thank you to the administrative staff of the Department of Chemical Engineering and Applied Chemistry, who have worked diligently behind the scenes and always been available to offer support when needed. Last but not least, I'd like to thank my family for their support and encouragement throughout this endeavor.

Table of Contents

List of Figures

List of Tables

List of Acronyms

EDLC	Electrical Double-Layer Capacitance
EDL	Electrical Double-Layer
KOH	Potassium Hydroxide
SEM	Scanning Electron Microscopy
XPS	X-ray Photoelectron Spectroscopy
CV	Cyclic Voltammetry
GC	Galvanostatic Cycling
EIS	Electrical Impedance Spectroscopy
SSA	Specific Surface Area

1. Introduction

1.1 Motivation

With the onset of climate change and the global movement towards renewable power generation, energy storage is becoming increasingly important in power systems of all scales. From handheld devices to windfarms of 1,000's of megawatts, stricter environmental regulations and the need for higher efficiency storage devices require new technologies to replace traditional solutions. While there is currently no clear front-runner in the energy storage landscape, electrochemical systems have garnered significant attention and their production at the commercial scale is rapidly growing.

Despite the diverse chemistries and resulting properties available within battery technology, power densities of these devices are limited by their reaction kinetics [1] (Figure 1.1). As a complement, or replacement to batteries for niche high power systems, supercapacitors are an attractive energy storage solution due to their high-power density capability and minimal performance degradation with charge/discharge cycling. While batteries store energy chemically, energy in supercapacitors is stored by the physical adsorption of electrolyte ions onto oppositely charged surfaces of electrodes – the formation of an electrical double layer capacitance (EDLC). Currently, the widespread application of supercapacitors is primarily prevented by their relatively low energy densities and high material costs [2]. In an attempt to improve these devices, new electrode materials and their surfaces are being investigated.

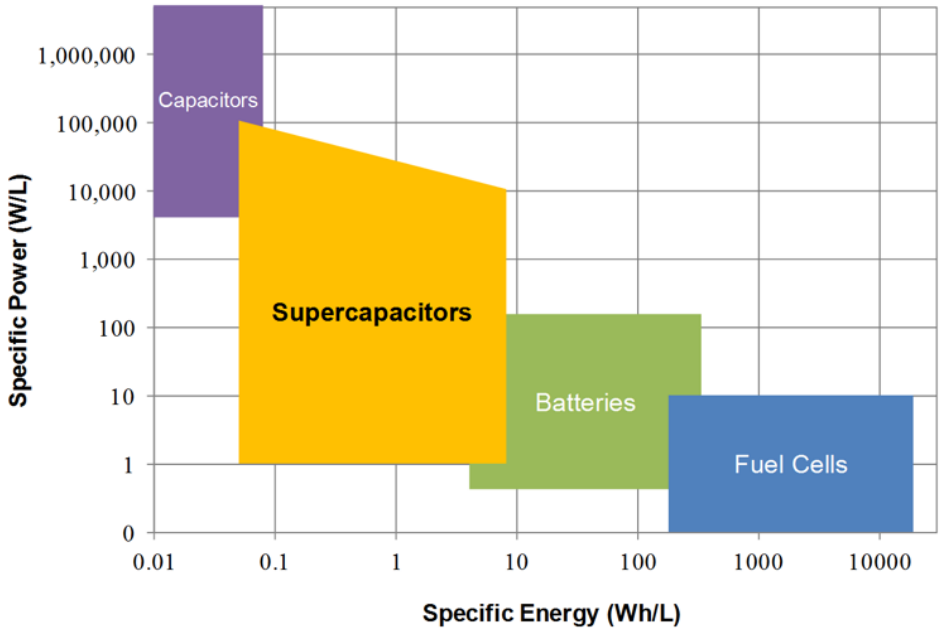

Figure 1.1 Ragone Plot

Ideal characteristics for supercapacitor electrodes are high specific surface area and high conductivity. Pore size distribution has also shown to be an important factor with regards to optimizing the double layer capacitive performance, and certain surface chemistries can provide pseudocapacitive contributions [2], [3]. Currently, most commercial electrodes are made from activated carbon powders which are held together with a binder material that is often non-conductive. This mixture is compressed into a thin film, on the order of a few 100's of microns thick, and placed on top of a foil current collector. A separator material is placed between the carbon thin films of opposing electrodes, and the entire setup is rolled into a conventional supercapacitor cell. Since the electrodes are very thin, the devices require a high ratio of ancillary components to active electrode material, hindering energy density.

A carbon material of increasing interest in a wide range of fields is biochar [4]. Biochar is produced from the pyrolysis of biomass precursors. Pyrolysis is the process in which biomass is heated to several hundred degrees Celsius in the absence of oxygen, and the organic components such as cellulose, hemicellulose, and lignin are chemically converted to char, tars/oils, and volatiles [4]. Biochar is inexpensive, readily available, and non-toxic. The cost per Farad stored of biochar is estimated to be ~100 times less than that of activated carbon; 0.001 $/F compared to 0.1 $/F [5].

Biochar can be produced as large monolithic pieces, and these can be readily shaped into electrode geometries much larger than the powder thin film status quo. The macrostructures of woody biomass used to transport water and nutrients are retained in biochar, and these may facilitate ion transportation during rapid charge/discharge cycles. Although the pyrolysis process reactions and the formation of nanoscale morphologies are not yet wholly understood, carbonaceous biochar does provide adequate specific surface area for capacitive charge storage [6]. While initial investigations indicate lower SSAs compared to activated carbons, the development of chemical activation methods has been able to improve this limitation in powdered biochar electrodes through either increased SSA, or the introduction of pseudocapacitive surface groups [5], [7], [8]. The benefits associated with the application of biochar, particularly of monolithic structure, as a supercapacitor electrode warrants further research into its viability.

1.2 Thesis Objectives

The overarching theme of this thesis is an investigation of how woody biochar electrode structure and dimension from macro to nano scales affect supercapacitor device performance. An underlying interest and goal is to evaluate the viability of large monolithic biochar as a competitor to conventional electrode materials.

Five main objectives and their associated studies are reported within:

1. Improve the current understanding of biochar microstructures through the application of advanced scanning electron microscopy (SEM) techniques.
2. Compare capacitive performance and device impedance between powder thin film and monolithic electrodes made from the same biochar.
3. Investigate the response of capacitive performance and device impedance when electrode thickness is increased for both thin film and monolithic structures.
4. Investigate the capacitive performance and device impedance of biochar electrodes produced from softwood (pine) and hardwood (maple) biomass precursors pyrolyzed at different temperatures.
5. Better understand and quantify ion mass transport processes during charge/discharge cycling.

1.3 Organization of Thesis

This thesis contains a combination of published and unpublished work. Chapter 3 is a paper that was recently submitted to *BioEnergy Research* (as of September 2017), and the information included has mostly been left unchanged. Chapter 4 is based on a paper published in the Electrochemical Society's *ECS Transactions* journal. This work was presented at the 231st ECS Meeting in New Orleans, Louisiana in May of 2017. Additional data has been included in this chapter to offer a more complete analysis. Chapter 5 contains unpublished work, and is a continuation of the study started in Chapter 4.

A general literature review of topics that relate to all of the chapters is conducted in Chapter 2, and each individual chapter has a more in-depth introduction section. Effort has been put forth to avoid overlapping information.

2. Literature Review

2.1 Supercapacitor Energy Storage

2.1.1 Electrical Double-Layer Capacitance

Electrical double-layer capacitance (EDLC) is an energy storage mechanism in which oppositely charged electrolyte ions adsorb onto a charged electrode surface. The "double-layer" refers to the formation of adjacent charged planes at the solid-liquid interface. In order to balance total charge within the system, positively and negatively charged electrodes are separated by an insulating porous membrane that permits ion migration.

The widely accepted Stern model for EDLC formation on a positively-charged flat electrode is shown in Figure 2.1(c). The Stern model combines the Helmholtz layer from the original EDL theory, as well as the diffuse layer from the Gouy-Chapman model (Figure 2.1 (a) and (b), respectively). A counter-ion rich layer of solvated ion molecules forms at the Inner Helmholtz Layer (IHL, or Stern layer), and the concentration of counter ions decreases exponentially extending outwards in the diffuse layer, until the charge-neutral bulk electrolyte is reached [9].

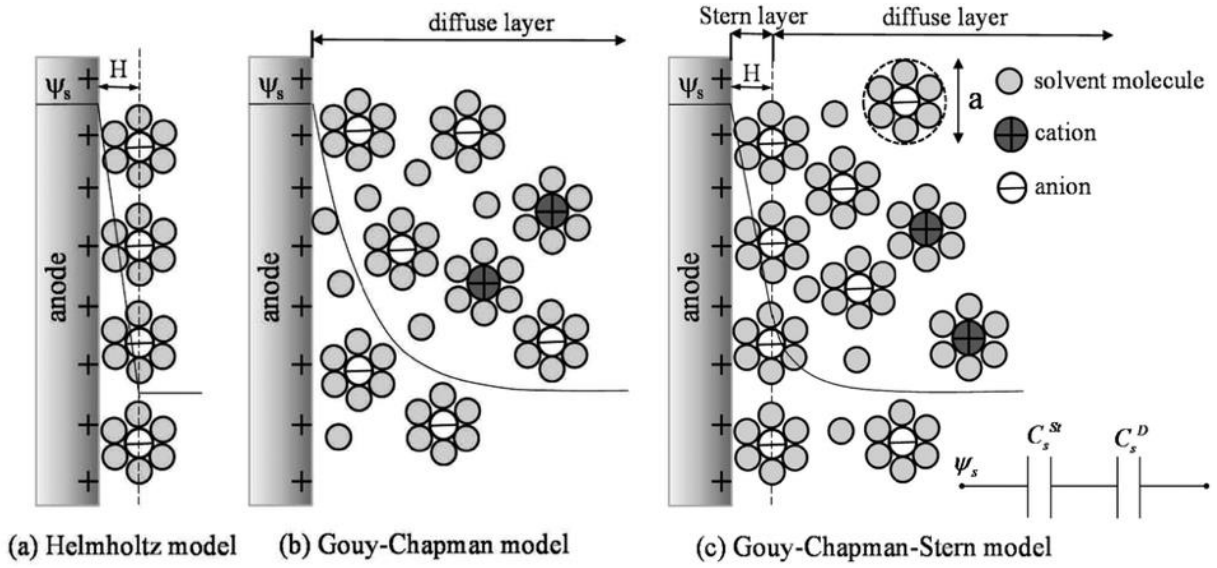

Figure 2.1 Helmholtz (a), Gouy-Chapman (b), and Stern (c) models of EDLC from [9]

Increasing the surface area of the EDL, and reducing the distance between the electrolyte ions and the electrode surface generally results in a higher total capacitance, which is measured in Farads. As a result, highly nanoporous materials with specific surface areas (SSAs) upwards of 2000 m^2/g are currently employed in commercial supercapacitor devices [10]. However, the EDLC mechanism becomes much more complex in confined pores and is still not fully understood as the interactions take place beyond current imaging capabilities [1]. The relationship between SSA and specific capacitance is not always positively correlated [11]. Mass transport of ions through tortuous microporous networks must also be considered in developing new electrodes, and this should be made as easy as possible in order to facilitate ion migration during charge/discharge cycling.

2.1.2 Pseudocapacitance

Pseudocapacitances are rapid faradaic reactions that take place at the surface of the electrode and within the same time scales as EDLC processes. They exist when electrodes are functionalized with chemical surface groups that form redox pairs with ions in the electrolyte [12]. Pseudocapacitances contribute to the total energy storage capacity of supercapacitors and help to improve energy density [13].

Pseudocapacitances are usually identified as sharp peaks in cyclic voltammetry scans, whereas an ideal, purely EDL capacitor will have a rectangular shaped response with no peaks. This is because the faradaic reactions of the redox pairs occur at specific voltages [12]. These reactions are most often reversible, but their energy storage contributions sometimes degrade faster than EDLC with repeated cycling [14].

In this work, highly concentrated (4M) aqueous potassium hydroxide (KOH) electrolyte was employed. Although aqueous electrolytes do not have as broad a voltage range as organic alternatives, they are much less expensive, less toxic, have smaller ions, and are more conductive [15]. In alkaline electrolyte, carboxyl and phenol oxygen surface groups have been found to result in pseudocapacitances [16], [17]. These acidic oxygen groups can react with the negative hydroxide ions in solution. In contrast, the quinone and carbonyl basic oxygen groups create

pseudocapacitive contributions through reactions with the hydrogen ions in acidic electrolyte solutions. A range of capacitance values have been reported for the contributions of these redox pairs.

2.2 Carbon as an Electrode Material

Regardless of the carbon type used in supercapacitors, a well-developed microporosity is a key component to its successful application [11]. Pores and their associated surfaces exist in a wide range of sizes. Within the microporosity spectrum are macropores of > 50 nm diameter, mesopores from 2 – 50 nm diameter, and micropores that are < 2 nm diameter. Of course, organizing these based on "diameters" is a somewhat loose method, as many different pore geometries occur. The three most commonly described groups of pore geometries are slit pores, which tend to be the smallest, as well as cylindrical and spherical pores.

2.2.1 Optimal Pore Size and Pore Accessibility

Electrode pore size selection and their accessibility to electrolyte ions is a complex, multidimensional problem. A thorough review of existing findings is required in order to draw accurate conclusions from experimental results with heterogeneous materials.

Several authors have reported an increase in EDL capacitance performance when carbon pores are the same size as the electrolyte ions [3], [18]–[20]. By tailoring the pore size within their electrodes to be uniform and approximately match that of the electrolyte's solvated ions (~ 0.6 nm), Chmiola et al. saw an increase of specific capacitance from 100 F/g to 140 F/g [3]. Their proposed model demonstrated that in these small pores, the hydration shell surrounding the ions becomes distorted by the rigid pore structures, akin to a balloon being squeezed, thus reducing the separation distance between the electrode and the charged ion. Since these processes occur beyond our imaging capabilities, Molecular Dynamics (MD) simulations are often relied upon and are compared to empirical data. MD work has shown that for sub-nanometer pores, the average coordination number of the hydrated ions decreased from 7 to 4, enabling ions to get closer to the electrode surface [21]. Ohkubo e al. demonstrated that a restabilization of hydrated ions occurs in the nano-space. When opposite pore walls are so close together, the liquid becomes more restricted and has

less freedom of motion compared to the bulk [22]. The molecules in these spaces are more tightly ordered which enables them to stabilize with lower coordination numbers.

There is still a lower limit to ion accessibility in electrode pores. Many authors have reported poor EDLC performance in carbon materials with small pore diameters relative to solvated ion size [18], [23], [24]. The inaccessibility of liquid electrolyte molecules into pores has been termed "ion sieving effects". Salitra et al. compared different aqueous electrolytes and found that surface area normalized capacitance in carbon electrodes with an average pore size smaller than an N_2 molecule (0.36 nm) increased with decreasing solvation shell size [18]. In addition, organic electrolytes, with larger solvation shells than aqueous electrolytes, were unable to fill the same-sized carbon pores [18]. As a general trend, pores with smaller diameters make larger contributions to SSA [25]. Therefore, while high SSA is desirable, these surfaces must be accessible to the electrolyte in order to contribute to the EDLC energy storage.

The question, "how small is too small?" with regards to pore diameters and capacitive storage capability, is not readily answered however. Kalluri et al. experimentally found that increasing the potential window of cyclic voltammetry scans resulted in higher specific capacitance performance exclusively to electrodes with sub-nanometer pores [26]. MD simulations illustrated that when the potential driving force surpasses a threshold, the solvation shells are either distorted or partially removed, enabling the ion to squeeze into pores in which it is not thermodynamically stable [26]. Electrolyte properties also come into play here, as the strength of the hydration shell can determine the driving force required for removal.

Charge/discharge rate also plays a large role in the pore accessibility of supercapacitor electrodes. Smaller pores and pores that are deep within the pore network only participate in EDLC processes when ample time is provided for ion migration during charge/discharge cycles as these present greater difficulties to ion mobility [27], [28]. At faster charge rates, both lower resistances and capacitances were seen and attributed to less of the material's surfaces participating in ion electroadsorption [27]. Despite the unexpected increase in specific capacitance seen in sub-nanometer pores by Chmiola et al., they did mention that the time required to discharge the energy was larger than for electrodes with larger pores [3].

With all these factors in mind, it is not surprising that suggestions have been made to tailor electrode pore size distribution to the desired application. Larger pore size distributions would better serve high power needs, while pore sizes similar to the electrolyte ion size would maximize total energy density so long as lengthy charge/discharge timescales are permitted. As a one-size-fits-all alternative, electrodes with hierarchal pore distributions have also been suggested [28], [29]. In these cases, larger pores can act as ion transport highways for fast diffusion processes, while smaller pores dispersed throughout would bolster energy density. Lastly, some authors have implied that there is an apparent limit to the effect of increasing BET SSA on EDLC performance, which is believed to be approximately 1500 m^2/g [11]. Above this value, it is argued that conflicting electric fields reduce overall electroadsorption [11].

2.2.2 Wettability

Unactivated graphitic carbon surfaces are very hydrophobic and this can make them difficult to fill with aqueous electrolyte solution [30]. Often micropores in carbons have been found not to be fully wetted [31]. While various heteroatoms typically appear in the material due to incomplete carbonization processes of the precursor, oxygen surface groups are regarded as the most important impurities as they can drastically enhance the affinity for water adsorption [32]. Simulations of the water adsorption mechanism on graphite slit pores show that water molecules cluster at oxygen surface sites within graphite, and that nearby surrounding oxygen surface groups can promote bridging of multiple clusters to propel the pore filling process [30]. Without the surface oxygen, capillary condensation, which requires high pressures, is needed to fill nanoscale slit pores [30]. Increasing the wettability of carbon electrode surfaces with oxygen groups can improve pore accessibility and the corresponding EDL specific capacitance, regardless of whether or not these oxygen groups provide pseudocapacitive contributions [32].

Experimentally, it is not easy to directly determine the wettability of porous carbon materials, which is usually achieved through contact angle measurements [33]. For this reason, analysis of surface chemistries through x-ray photoelectron spectroscopy (XPS) is applied.

2.3 Biochar

Biochar is the solid, primarily carbon product of pyrolyzed biomass. It is produced by heating biomass in the absence of oxygen (typically in a nitrogen environment) up to several hundred degrees Celsius. There is growing interest in biochar as a material for a wide range of applications. Recent developments in literature have promoted its application as a catalyst, gas adsorbent, soil amendment, and electrochemical cell electrode [4], [34]. Within these fields, the successful application of biochar is largely due to the characteristics of its nanostructures – specifically the pore geometries, pore accessibility, and total surface areas; as well as its surface chemistry.

This thesis investigates biochar produced from sugar maple (a hardwood) and white pine (a softwood) wood precursors. These woods are made of internal structures with different arrangements and chemical compositions of the molecular building blocks cellulose, lignin (and/or pectin), and hemicellulose [35]. The approximate total amounts of the three primary molecular building blocks are similar for hard and soft woods – 44% and 42% cellulose, 28% and 27% hemicellulose, and 24% and 28% lignin, in hard and softwood respectively, with the remainder (4% and 3%) extractives [36].

2.3.1 Pyrolysis production process

During pyrolysis, biomass is converted into 3 main products: solid char (biochar), liquid bio-oil condensate, and gases. Undesired ash can also be produced in biochar; however, it tends to appear in negligible amounts when woody biomass precursor materials are used [37]. Pyrolysis process conditions are tailored to maximize the yield of the desired end product and as such, they can range widely with regards to residence time and temperature. Fast-pyrolysis processes, on the order of seconds to minutes, optimize the yield of liquid products, or bio-oils which are used as fuel sources [38]. Slow-pyrolysis processes can require up to several days to complete and promote the yield of char [38], [39]. Often, a slow-pyrolysis process has multiple steps with different temperature ramp rates and residence times. All biochar studied in this work was produced with slow-pyrolysis processes.

Some experiments conducted within this thesis use in-house pyrolyzed biochar. This biochar was pyrolyzed in a tubular furnace up to the desired final temperature according to the thermal treatment schedule outlined in expired U.S. Patent 6,124,028 by Byrne and Nagle (Table I) [39]. This process is significant, because it affords a method to convert large cuts of woody precursor into uniformly treated, crack-free, highly carbonized monolithic structures [40]. The process causes some dimensional shrinkage, but overall the dimensions of the starting cut of wood remain proportionate in the biochar product.

Table I. Amended pyrolysis process thermal treatment schedule outlined by expired U.S. Patent 6,124,028 [39]

Temperature Range (°C)	Heating Ramp Rate (°C/min)	Hold Time at Upper Temperature (min)
25 – 90	0.83	180
90 – 200	0.25	6
200 – 400	0.13	6
400 – 600	0.33	6
600 – 800	0.33	6
800 – 1000	0.33	6

After developing their patent, Byrne and Nagle carried out the characterization of tulip poplar wood biochar at different final pyrolysis temperatures. For final pyrolysis temperatures between 600 – 1000°C, all dimensions of the biochar were found to shrink compared to the precursor [40]. Within this range of temperatures, the degree of shrinkage ranged from 16 – 21% in the wood axial direction, 26 – 32% in the radial direction, and 37 – 42% in the tangential direction [40]. Carbon yield of the biochar product decreases from 27 – 25% within the 600 - 1000°C final pyrolysis temperature range, with more significant losses occurring at temperatures below 600°C [40]. As can be seen in Table I, the total residence time is tied to the desired final temperature of the pyrolysis process. Therefore, the effects of residence time versus temperature on the biochar cannot be decoupled for this slow-pyrolysis process. Despite the shrinkage and mass loss, the biochar macrostructures remain mostly intact. Structural components within the wood such as tracheids and vessels are clearly visible in biochar products.

Individually, the cellulose, lignin, and hemicellulose molecules react differently to the pyrolysis process resulting in diverse chemical properties of the respective char [37], [41]–[43]. For

example, amorphous hemicellulose molecules have much lower thermal stability compared to highly crosslinked lignin molecules or crystalline cellulose structures [43]. As a result, various pyrolysis reactions take place at different temperatures. Proposed molecular reaction pathways and intermediates' structures during pyrolysis have attempted to bridge the knowledge gap of the cause-and-effect relationship affecting biochar properties with limited certainty. Despite the existing characterization work completed on the different building blocks of biomass, none have reported differences in biochar microporosity due to molecular composition.

The conductivity of biochar has only recently attracted attention and there is very limited data on the subject, especially from controlled experiments. As a testament to this, a PhD candidate of the Green Tech Lab Group at the University of Toronto is currently dedicating his entire thesis to this field. Some studies of biochar carbonization/graphitization are available however. As expected, trends of increasing carbonization of biochar have been seen with increasing pyrolysis temperatures [40], [44], [45]. These carbons are arranged as disordered graphite crystals as determined by Raman Spectroscopy [34]. Furthermore, aromatic carbon cluster size increase has been observed with increasing pyrolysis temperature in maple wood biochar [46]. It is hypothesized that higher pyrolyzation temperatures and longer residence times will enhance the organization of graphite crystals and therefore conductivity in biochar, but this is unconfirmed.

3. Connecting nanoscale morphologies of biochar to biomass molecular compositions via high-resolution Scanning Electron Microscopy

3.1 Introduction – Biochar nanostructures and their characterization

Microporous features of biochar and their associated surface areas are key aspects for application as an electrochemical cell electrode, a catalyst, a soil amendment, and a filtration membrane. Despite the recent growth of biochar research, there is still a severe lack of knowledge of its nanoscale morphology. Fortunately, improvements in microscopy techniques are continually being developed to enable higher resolution and contrast. Improving the ability to accurately characterize biochar at these small scales will facilitate future technological developments.

In this chapter, the focus was on biochar produced from a slow-pyrolysis process of sugar maple wood precursor. Sugar maple, formally known as *Acer saccharum*, is a hard wood (angiosperm). Its primary macrostructure components are tracheids (sometimes referred to as fibers), vessels, and rays (Figure 3.1). Tracheid and vessel channels extend in the axial direction of the tree, while rays provide transport to water and nutrients in the radial direction. Pits are small (micron-scale) openings that occur along the walls of vessels. Pits also facilitate the radial-direction transport properties, and primarily exist in earlywood, or more recently grown wood. Despite the drastic chemical changes that occur during pyrolysis, the biomass macrostructural morphologies are largely retained and are readily identified through Scanning Electron Microscopy (SEM).

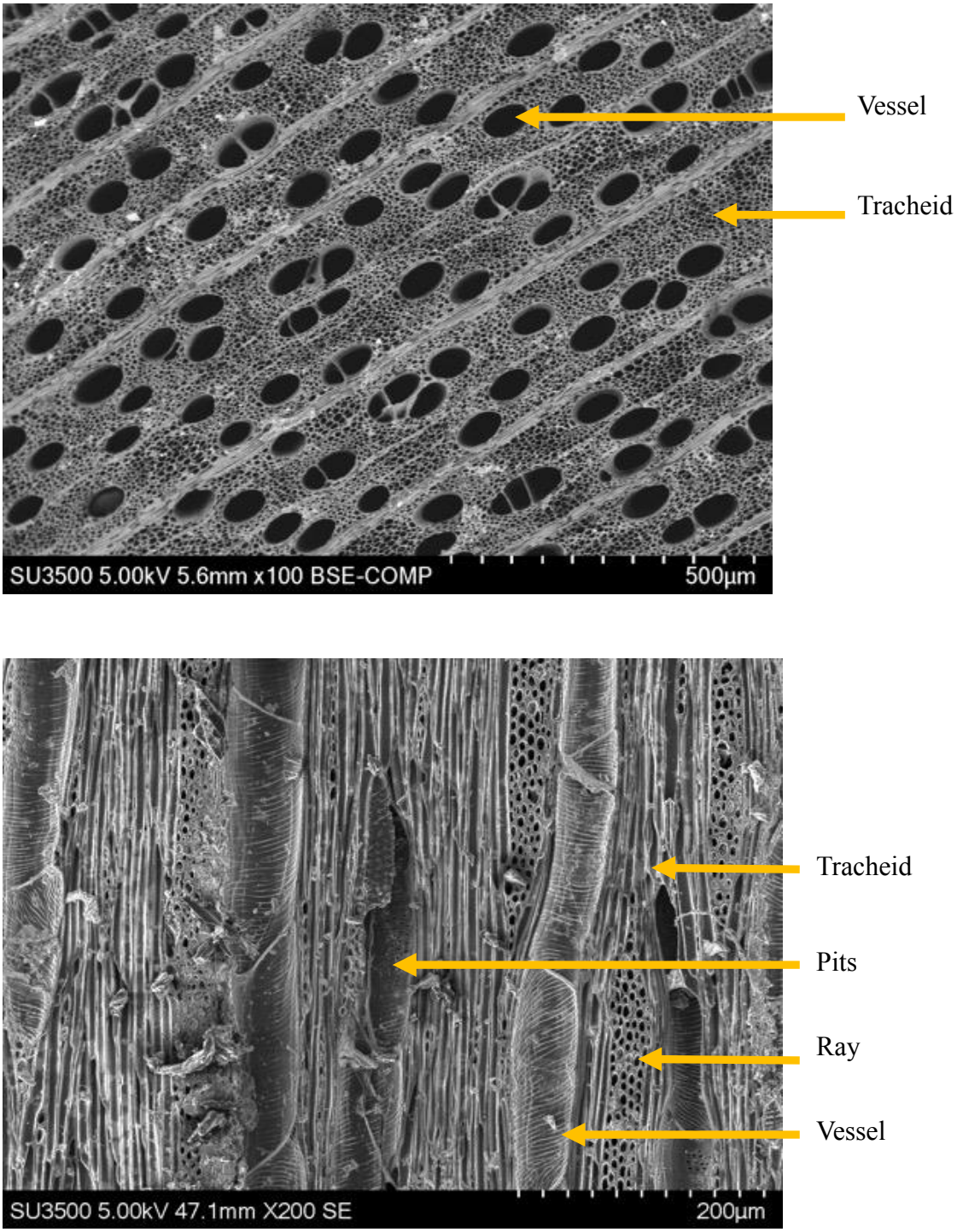

Figure 3.1 SEM images of sugar maple biochar monolith in the tree axial direction (top) and the radial direction (bottom)

Microscopy with both SEM and Transmission Electron Microscopy (TEM) are common direct characterization methods for biochar. While conventional SEMs are often cited to be able to

resolve nanometer-sized features, this is for ideal samples that are flat and smooth. Rough, porous materials such as biochar do not meet the ideal sample criteria, and as such SEMs are used primarily used to reveal the macrostructure and tortuosity of biochar at the micron scale [5], [47], [48]. TEM imaging has been used by many researchers to observe micro- and meso- pore structures in different types of biochar [7], [49]–[52]. However, because of the small particle size of biochar required for TEM, and the very high magnifications used, it is often not possible to understand the orientation or location of a pore relative to the macrostructure. Furthermore, the tiny sample sizes make it impractical to determine the frequency and number of types of nanopore structures that exist within a single biochar.

Beam deceleration is a modified SEM technique in which a negative potential bias is placed on the sample stage to induce an electric field within the microscope. This method reduces the landing energy of incident electrons from their initial acceleration voltage energy, thus limiting their penetration depth, enabling better resolution, contrast, and signal detection efficiency [53]. With a powerful SEM device, resolutions that were previously impossible to achieve at such low electron beam energies are realizable, enabling more detailed topographical images at higher magnifications [54]. Currently, no attempt to apply beam deceleration SEM imaging on biochar has been reported in the literature.

Physisorption is a common method to indirectly measure the specific surface area (SSA) and pore size distribution of biochar. Physisorption with nitrogen gas is used to probe pore sizes from ~1 – 50 nm, but tends to lose accuracy in the micropore region (< 2 nm) [55]. As such, carbon dioxide, a smaller gas molecule than nitrogen, can be applied to measure the SSA of micropores between ~0.3 – 1.6 nm. Results from both methods can then be superimposed to provide the full spectrum details [55].

Nitrogen gas SSA values are commonly calculated using either BET or Density Functional Theory (DFT) data reduction techniques. For unactivated biochar, reported BET SSA values can range anywhere from 2 – 500 m^2/g [6]. The SSA of biochar is dependent on its precursor material and the pyrolysis process conditions. Recently, DFT reduction methods have become the preferred method for analyzing microporosity [55]. When DFT is used, pore geometries must be known or

assumed to make the appropriate model selection. For example, a model for slit pores will result in a different SSA and pore size distribution compared to a model for cylindrical pores with the same raw data. Carbon dioxide physisorption requires DFT data reduction, and currently only a slit pore geometry model is available. Literature reports CO_2 determined SSA values up to several hundred m^2/g from biochar micropores [6]. The pore size distributions of biochar are relatively broad at both the macro and nano scales compared to most activated carbons [6]. As a general trend across all fields, higher microporosity and SSA are desired in biochar, therefore increasing value is being placed on the accurate characterization of biochar SSA and pore size distribution.

This study reveals the enhanced resolution capabilities of the beam deceleration SEM technique as applied to sugar maple biochar samples. From the images produced, it is possible to understand the orientation of nanoscale features, to see the range of geometries and dimensions of the features, and to determine the biochar macrostructural elements that they originate from. This new information prompts discussion on the different morphologies of nanostructures seen within the same biochar material, such as the relationship between nanostructure geometry and the original molecular building block from the biomass precursor.

3.2 Experimental

3.2.1 SEM Imaging

A Hitachi SU-8230 high resolution scanning electron microscope was used in this study. The acceleration voltage was 2.2 kV with a working distance of 2.3 mm. The deceleration mode was set to medium, with a deceleration voltage of 1.5 kV (landing voltage was 0.7 kV). The detection mode was set to SE + BSE (TU) for a high energy electron image. In this mode, the top and upper detectors collect SE and BSE signals.

A Hitachi SU-3500 scanning electron microscope was used to take low magnification images of monolithic biochar to show macrostructural components.

3.2.2 Biochar sample procurement and preparation

Commercially produced sugar maple hardwood biochar was purchased from Basques Hardwood Charcoal (Quebec, Canada). Although the precise pyrolysis conditions are not known, characterization methods show similarities to biochar pyrolyzed in-house at temperatures between 700-750°C.

For SU-8230 imaging, solid pieces of biochar were pulverized with a mortar and pestle and then sieved. Particles ranging from 53 – 212 μm were collected for imaging. Particles were stuck to a conventional pin stub specimen mount with aqueous based Alfa Aesar graphite conductive adhesive. Residual particles were blown away with compressed air.

Monolithic biochar was imaged with the SU-3500. Thin slices of biochar were polished down to appropriate size in stages using 60, 100, and 200 grit silicon carbide paper. Dimensions were approximately 7 x 7 x 2 mm (length x height x thickness), such that the piece could be clipped into a spring-loaded sample holder.

3.3 Results and Discussion

Using the SU-8230 SEM, different regions of the biochar macrostructure were identified within the particulate sample. The microstructures of these regions were then investigated with higher magnifications, and differences are reported below.

The first microstructures investigated are those that exist on the tracheid walls. A particle that was once part of a tracheid was readily identified in the sample by its geometry (Figure 3.2a); roughly circular diameters of 3-15 μm were observed for tracheids using the SU-3500 SEM. Different magnifications of this particle and its morphology are shown in Figure 3.2. At the highest magnification (Figure 3.2c), pock-mark structures are clearly seen. The diameters of these pores range from approximately 3 – 25 nm, categorizing them as mesopores. The darkness of the pores suggests that they are deeper than they are wide, classifying them as cylindrical pores.

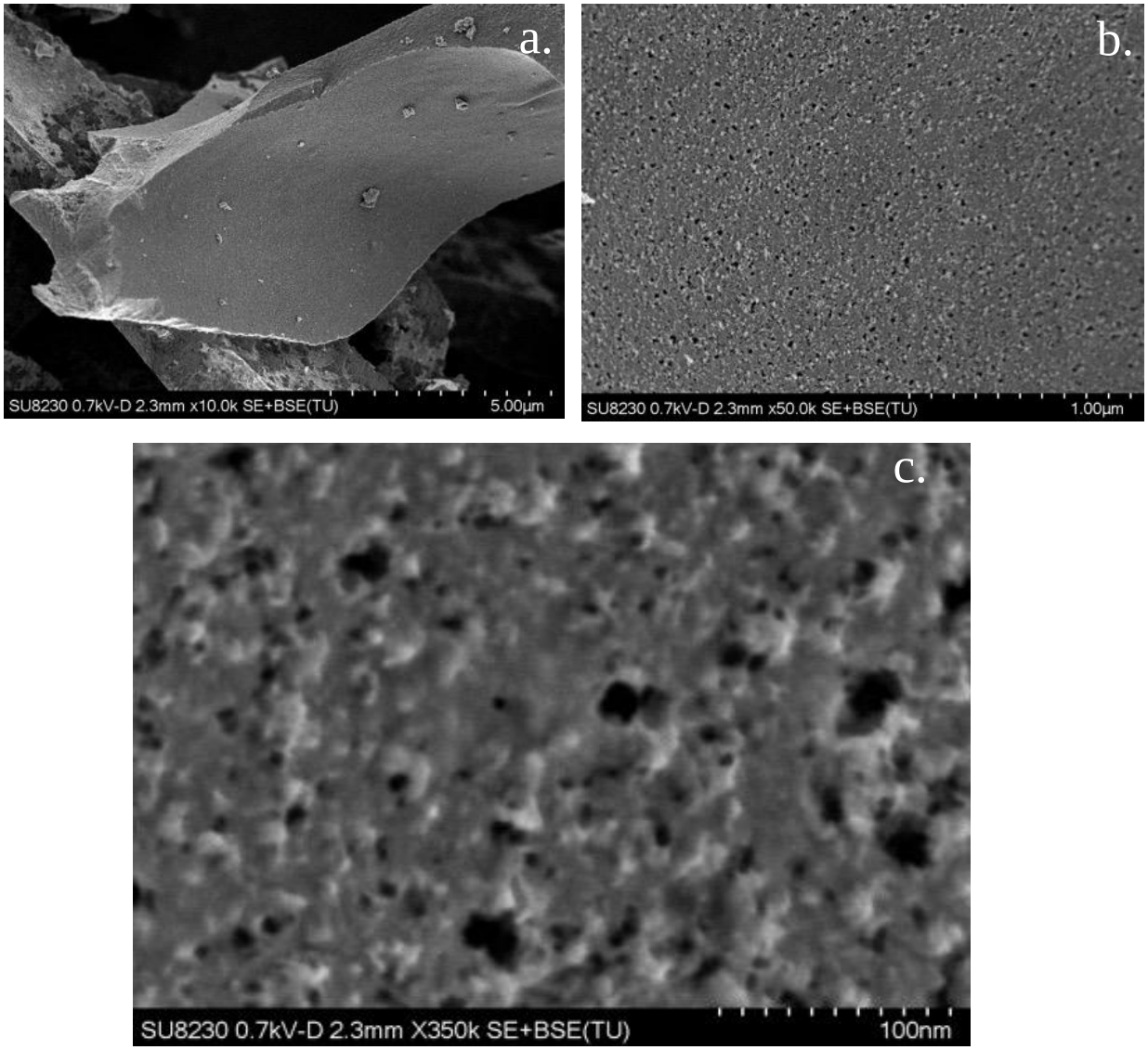

Figure 3.2 Different magnifications of a tracheid wall and its microstructures

Microstructures occurring along a vessel wall are shown in Figure 3.3b, c. The vessel wall was identified by the appearance and pattern of pits, seen in Figure 3.3a [56]. The morphology of the mesopores are similar to those seen on tracheid walls. In comparing Figure 3.3c with Figure 3.2c, a slightly lower pore density appears to exist on the vessel wall. Both of these images also contain indications of surface textures beyond the resolution capabilities of the SEM device. This is expected, as physisorption studies on a variety of biochar samples with CO_2 gas show SSA values up to several hundred m^2/g from micropores with a diameter range of approximately 0.3 – 1.6 nm [6]. Surface details of this scale currently require a TEM device to resolve.

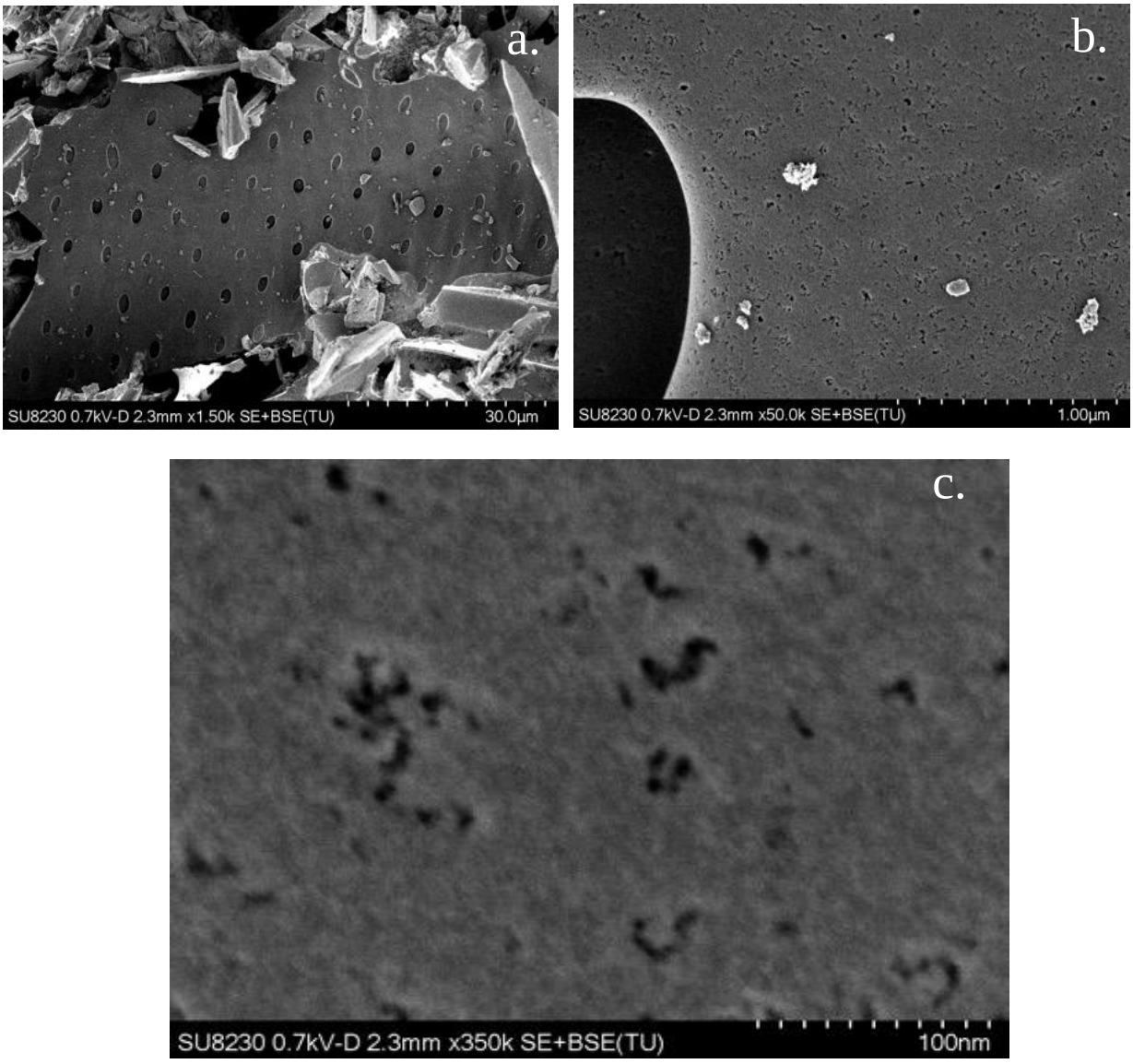

Figure 3.3 Different magnifications of a vessel wall and its microstructures

The cell walls of tracheids and vessels are known to be composed of different layers: a primary layer, and three secondary layers (S1, S2, and S3) [35]. The images in Figure 3.2 and Figure 3.3 are easily identified to be the surface of the macropores. Secondary cell wall layers are dominated by high contents of cellulose, with increasing concentration moving towards the tracheid wall surface from S1 to S3 [35]. In contrast, the primary layer of the cell wall has a lignin-rich composition (~70%) [35]. The S3 layer contains the largest fraction of cellulose within a tracheid cell wall, approximately 47% [35]. Therefore, the microstructures seen in Figure 3.2a and Figure 3.3a result from the pyrolysis of cellulose-rich biomass.

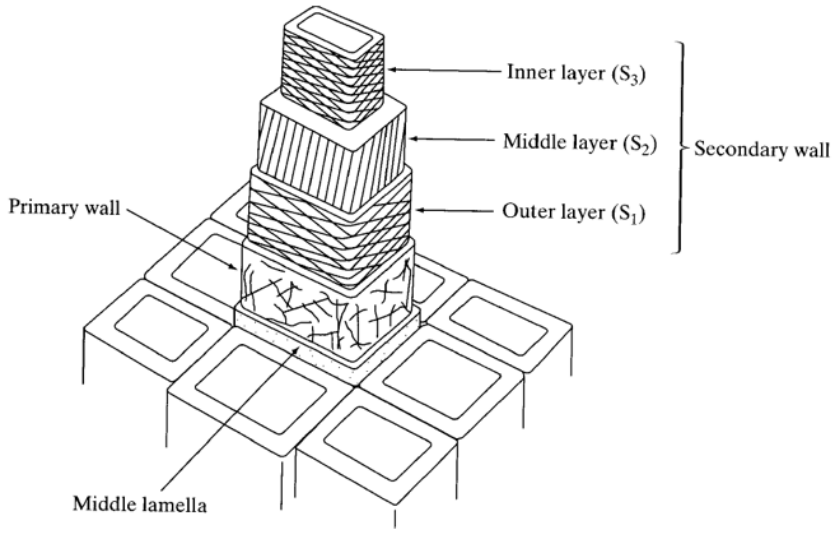

Figure 3.4 Conceptualized anatomy of tracheids in hardwood, from [57]

For the first time, a second distinctive regularly occurring microstructure was also seen in the biochar sample (Figure 3.5d). This unique morphology occurs between adjacent tracheids, in a lignin-rich element of hardwood biomass identified as the middle lamella (shown in Figure 3.4) [41]. The nanoscale morphology is very different from that seen in Figure 3.2c and Figure 3.3c. It appears highly porous and foam-like, with spherical and slit mesopore geometries. Although no relationship has been made previously between biochar nanostructures and their precursor biomass chemistries, it has been suggested that the foam-like macrostructure of lignin biochar results from a brief liquid phase and the formation of bubbles during the slow pyrolysis process [38], [58].

There is an observable decrease in foam-like porosity moving outward from the pyrolyzed middle lamella region identifiable in Figure 3.5a, as well as moving from left to right towards the tracheid wall surface in Figure 3.5b. This trend directly correlates to lignin content within the biomass precursor structure. The appearance of foam-like microstructures in the resulting biochar is tied to the proportion of lignin in the original biomass material.

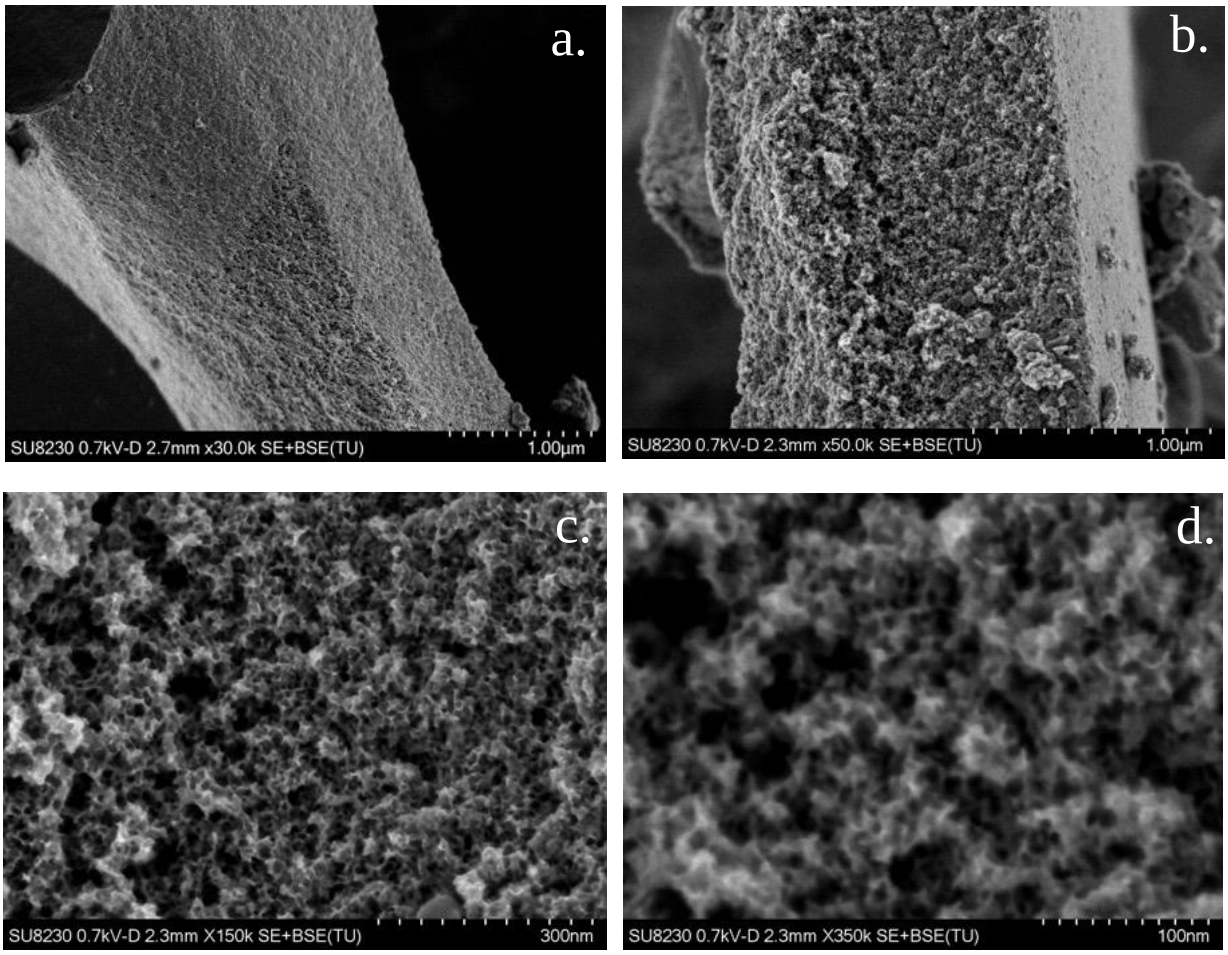

Figure 3.5 Different magnifications of a middle lamella and its microstructures

The variety of nanoscale morphologies seen throughout sugar maple biochar are believed to result from the pyrolysis of different molecular building blocks that exist throughout the precursor biomass. Although cellulose, lignin, and hemicellulose building blocks are mostly mixed within biomass, specific regions dominated with high-concentration of a single type of molecule help to identify resulting features. While the findings of this study show the physical result of different pyrolysis reactions, further investigation into the molecular structures and chemical changes may help elucidate the nanostructure formation process. Of course, this is no simple task, as multiple reaction mechanisms of different biomass molecules as well as their intermediates contribute to the final product.

3.4 Conclusion

The beam deceleration technique applied with a high-powered SEM instrument enables the resolution of nanoscale surface features of biochar down to approximately 3 nm. In the case of sugar maple slow-pyrolyzed biochar, nanostructures with slit, cylindrical, and spherical geometries were seen for the first time. In addition to clearly seeing these structures in their entirety along with their orientations, the wide range of magnification of the SEM device makes it possible to understand where these different mesopore structures exist within the biochar macrostructure.

SEM imaging and wood anatomy analysis suggest that the biochar nanostructure morphology is linked to the chemical composition of the original biomass precursor. Biomass surfaces made primarily of crystalline cellulose molecules tend to have pock-marked mesoporous features after a slow-pyrolysis treatment, whereas the highly crosslinked lignin building blocks are pyrolyzed into foam-like microstructures. While the underlying mechanism for these physical differences is not fully understood, it is most likely due to varying molecular structures and their respective chemical reactions during pyrolysis.

4. Investigation of biochar powder thin film versus monolithic electrode structures and the effects of increasing electrode thickness

4.1 Introduction – Biochar as an electrode material

Powdered biochar has been investigated by several research groups as an alternative to activated carbon powders for thin film supercapacitor electrodes and has displayed promising performance. Electrochemically-tested biochar has come from diverse precursor feedstocks, often sourced from local biomass or accessible waste materials: corn cobs, distiller dried grains, cotton stalk, peach stones, rice husks, *Sterculia lychnophora* (seeds of a tree common in parts of China), wood processing wastes, and spent coffee grounds, to name a few [8], [50], [59]–[63]. A variety of pyrolysis process conditions have been applied, and many of these biochars have been activated either post-pyrolysis, or in a one-step pyrolysis/activation process to enhance performance. In addition, different electrochemical testing conditions such as charge/discharge rates, as well as electrolyte selection and its concentration make it difficult to compare respective biochar performance. To narrow the scope of this review, details of biochar capacitive performances will be presented for woody biomass precursors that can be made into monolithic electrodes, contain minimal ash content, and come from more widely accessible materials.

Different types of woods have been applied in biochar production for thin film supercapacitor electrodes. Unactivated red cedar wood biochar pyrolyzed at 750°C with ~98% carbon content and an approximate BET SSA of 400 m^2/g achieved a specific capacitance of 14 F/g as a thin film supercapacitor electrode in a 0.5M sulfuric acid electrolyte [5]. This was further activated with dilute nitric acid to improve to a specific capacitance of 114 F/g [5]. These capacitance values were evaluated with asymmetric electrochemical cells (platinum wire as the counter electrode), through Galvanostatic Cycling (GC) measurements applying a 500 mA/g current density charge rate. Dehkhoda et al. used commercially purchased fast-pyrolyzed biochar powder particles between 40 – 150 μm from Dynamotive Energy Systems Corporation (Canada) to prepare untreated and potassium hydroxide activated electrodes for symmetric supercapacitor cells [64]. The as-received biochar had a carbon content of 63% and a BET specific surface area of only 1.66 m^2/g, which changed to 81% and 990 m^2/g, and 59% (this reported % may be an error on the low side, as the weight %'s do not add up in the paper) and 614 m^2/g when activated with 7M potassium

hydroxide solution at 675°C and 1000°C, respectively [64]. With 5 wt.% Nafion ® binder, the 675°C treated sample had a discharge specific capacitance of 55 F/g, and the 1000°C treated sample had a discharge specific capacitance of 31 F/g [64]. These values were attained in 0.1M sodium chloride and 0.1M sodium hydroxide mixed electrolyte, from GC response curves with a 2 mA discharge current over a 0.25 – 0V voltage range. The small voltage range tested may have inflated the capacitance performance results. With all the variables to consider between material preparation, electrochemical cell setup, and testing technique, it is not easy to evaluate the energy storage capabilities of biochars from different studies. The above information is supplied to provide points of reference, as well as give some insight on the types of experiments being performed in the field.

Crack-free, high carbon content, solid monolithic biochar can be produced by applying the slow-pyrolysis procedure outlined in US Patent 6,124,028 to inexpensive and readily available woody biomass [39]. From the large pieces of biochar produced, it is easy to shape monolithic electrodes that are in the cm^3 volume range, or orders of magnitude larger than thin film electrodes. With larger electrodes, it would be possible to reduce the ratio of ancillary components in the device, improving energy density. While commercial application and most research of supercapacitor devices utilizes powder thin film electrodes, a study of the same carbon material with monolithic and thin film electrode structures revealed that the monolithic electrode had a higher conductivity by two orders of magnitude, as well as a higher specific capacitance at low charging rates [65].

Only two studies of monolithic biochar electrodes have been found in the literature. In the first, nitric acid activated miniscule monolithic electrodes (~0.1 cm x 0.1 cm x 0.05 cm, and 1 mg in mass) from maple wood biochar with a BET SSA of 303 m^2/g were investigated [47]. A specific capacitance of 31 F/g was observed in 0.5M sulfuric acid electrolyte at a 500 mA/g current density charge rate, compared to 32 F/g for its powder thin film counterpart [47]. The galvanostatic cycling tests, from which capacitance was determined, were conducted over a limited voltage range however, from -0.15 – 0.25 V, and this may have resulted in inflated specific capacitance performance. In the second study, poplar wood biochar pyrolyzed at 900°C for 6 hours was shaped into 1 cm x 1 cm x 1mm monolithic electrodes. Different activation conditions with nitric acid were then applied, modifying the temperature, duration, and concentration [66]. The maximum

device specific capacitance achieved from the modified biochar was 59 F/g at a 5 mA/cm^2 charge rate in 2M KOH electrolyte with a BET SSA of 416 m^2/g [66]. While this study shows potential for monolithic electrodes, electrode thickness was relatively limited compared to what is possible to construct, and the monolithic performance was not compared to a powder thin film of the same material. By implementing larger monolithic biochar electrodes, the natural internal structures of precursor biomass used to transport water and nutrients in trees are preserved in the electrode, and these elements may facilitate the migration of ions during charge/discharge processes in larger structures.

The internal structures of different types of biomass retained in monolithic biochar have a huge diversity in anatomy. Hard and soft woods have different primary structural elements (those of maple were outlined in Section 3.1) [56]. Softwoods do not have vessels and pits, and instead have a larger number of tracheids [35]. Within the broad hard and soft wood categories, individual species have unique shapes, sizes, arrangements, and densities of internal components. Depending on the precursor, monolithic biochar can have connective channels from the internal structures with diameters up to several 100's of μm and less than 1 μm [56]. These dimensions can also vary widely within the same wood species, depending on age of the tree, growing conditions, and natural variability. When the electrode is immersed in an electrolyte solution, pores this large act as electrolyte reservoirs. Typical dimension ranges of primary structural components of hardwoods (maple) and softwoods (pine) are summarized in Table II.

Table II. Approximate Dimensions of Primary Structural Components for Hardwood and Softwood

Structural Component	Dimension	Hardwood (Maple)	Softwood (Pine)
Tracheid	**Diameter**	10 – 50 μm [67]	20 – 65 μm [68]
	Length	< 1.5 mm [67]	2 – 7+ mm [68]
Ray	**Diameter**	10 – 50 μm [69]	1 – 2 cells wide [68]
	Length	0.1 – 0.22 mm [69]	0.3 – 0.8 mm [68]
Vessel Element*	**Diameter**	5 – 500 μm [69]	N/A
	Length	0.2 – 1.3 mm [69]	N/A
Vessel Pits	**Diameter**	3-6 μm [70]	N/A

*Vessel Elements stack to 10+ cm and are separated by perforation plates permeable to water [70]

One of the application concerns with biochar, especially with a monolithic structure, is that tars and heavy oils produced during pyrolysis may get stuck and condense within the porous structure during cooling [64], [71]. If this occurs, there is a possibility that some pore blockages occur, even resulting in "dead spaces" within the electrode that are not accessible. Although blocked pores/regions may still be accessible to small CO_2 or N_2 gas molecules during physisorption measurements, revealing a specific surface area contribution, it does not necessarily mean that the pore can be accessed and filled with the electrolyte solution [10]. Comparing the performance of powder thin film and monolithic electrodes made of the same material will provide insight as to whether significant dead spaces exist and hinder performance in the monolithic structures.

Increasing the thickness of supercapacitor electrodes reduces the ratio of ancillary components in the device and can theoretically improve volumetric capacitance and energy density. Although some authors report improvements in total capacity (in Farads) of supercapacitor devices with increasing electrode thickness, a more common theme is a reduction in energy storage performance. The primary reported causes of capacitive performance degradation with increasing electrode thickness are related to mass transportation issues. As a result, conventional powder thin film supercapacitor electrodes are limited to a few 100 microns thick [1].

While increasing the thickness of powder thin film electrodes, an observed decrease in specific capacitance was attributed to longer ion migration pathways [72]. Binder content and highly-

conductive carbon additive composition of these electrodes were previously optimized in the same study, suggesting that the performance is in fact limited by mass transport processes. Porous carbon tortuosity was not an investigated variable however, and therefore improving the diffusional network through the optimization of pore size distribution may compensate for the losses associated with increasing electrode thickness. In a similar study using starburst powder thin film carbons, it was found that increasing the electrode thickness from 100 – 500 μm significantly increased the ion transport resistance in the interparticle macropores [73]. These mass transport resistances are linked to poor rate performance of the device, which is one of the main attractions for supercapacitors [74]. In addition, electrodes with a thickness of 200 μm were made with carbon particles of different diameters, and a slight increase in the transport resistance with increasing particle size demonstrates the smaller effects of intraparticle pore diffusion lengths on rate capability [73].

A monotonic increase in total capacitance with electrode thickness was seen for carbon thin film electrodes of 50 – 250 μm thick [75]. In this study however, a relatively slow charge rate was applied and rate capability was not tested; limitations caused by mass transport may not have been noticed. Regardless, an important consideration must be made for further studies of electrode thickness: while specific capacitance may decrease with increasing electrode thickness, there is still a possibility that the overall volumetric capacitance and total capacity of the device can increase.

Only single thin film electrodes have been investigated. Some authors have investigated the effects of increasing thin film thickness on capacitive performance, but it becomes difficult to maintain uniform particle packing and bulk density [73]. This chapter will therefore investigate increasing thickness of thin film electrodes by stacking them together in the cell. This way, individual thin film properties are maintained.

This chapter is broken down into two parts. In Part I, the effect of electrode structure on capacitive performance and device impedance will be investigated. Thin film and monolithic biochar electrodes made from the same biochar material will be evaluated against one another. These two electrode types have different macroporosity, tortuosity, bulk density, and carbon-carbon contacts.

Monolithic and thin film electrodes will be made from both maple wood and pine wood to investigate biochar density differences and effects of different biomass precursors. These two species have very different anatomies, therefore if the natural internal structures of the biomass play a role in charge/discharge ion diffusion processes, differences in capacitive performance should be seen. The objective of Part II is to investigate the effect of electrode thickness on capacitive performance. Thin films and monolithic electrodes will be tested with a range of thicknesses extending several times larger than those seen in current commercial devices.

4.2 Experimental

4.2.1 Pyrolysis Process

Part I of the objectives was studied using electrodes made from in-house pyrolyzed biochar. This biochar was produced by following the steps of the slow-pyrolysis process outlined in the expired US Patent 6,124,028 up to 800°C (process summarized in Section 2.3.1, and thermal treatment schedule outlined in Table I). This was completed on maple and pine wood biomass precursors, measuring approximately 2” x 1” x 6” purchased locally.

Part II of the objectives was studied using commercially purchased sugar maple hardwood biochar from Basques Hardwood Charcoal (Quebec, Canada). Although the precise pyrolysis conditions are not known, characterization methods show similarities to the in-house pyrolyzed biochar and suggest temperatures reached up to 700-750°C.

4.2.2 Electrode Fabrication

Monolithic electrodes were cut out of larger pieces of biochar. They were sanded down to desired shape and dimension using steps of 60, 100, and 200 grit silicon carbide paper. The electrodes were then rinsed with DI water to remove any loose particulates. All monolithic electrodes were oriented such that their thickness extends in the direction of the tree’s axial orientation. An illustration of the monolithic electrode geometries is shown in Figure 4.1, and a summary of the average physical properties can be found in Table III.

Pieces of the same biochar used to produce the monolith electrodes were pulverized with a mortar and pestle. Particles were sieved and those between 53-212 μm were taken for thin film processing. Biochar particles were mixed with 5 wt.% PTFE binder and 5 wt.% carbon black in small, equal amounts of DI water and isopropanol. The mixture was gently warmed to evaporate most of the liquid, then rolled into a thin film sheet approximately 0.3 mm thick with a pasta roller. Electrodes were punched out with a circular mould (Figure 4.1). Average physical properties can be found in Table III. It should be noted that porous carbons powders are highly compressible, and their thickness may vary with loading pressure when installed in the cell [32].

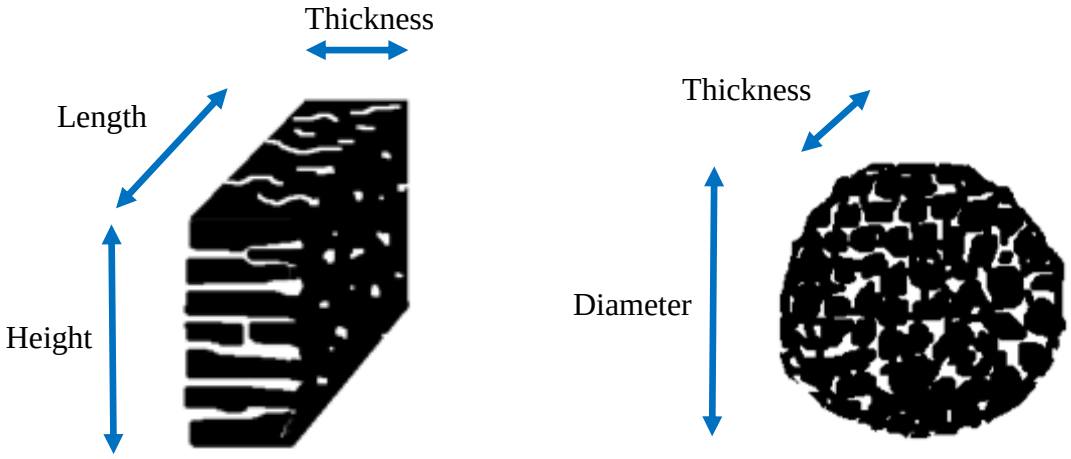

Figure 4.1. Illustrations of monolithic and thin film electrode geometries

Table III. Average Physical Characteristics of Electrodes.

Electrodes:	Mass (g)	Thickness (mm)	Length (mm)	Height (mm)	Cross Sectional Area (mm^2)	Bulk Density (g/cm^3)
Maple Monolithic	0.0528	2.0	6.7	7.0	46.90	0.58
Maple Thin Film*	0.0208	0.3	9.5	N/A	70.88	0.98
Pine Monolithic	0.0303	2.0	7.3	7.4	53.66	0.29
Pine Thin Film*	0.0212	0.3	9.5	N/A	70.88	1.00
Commercial Monolithic:						
1 mm	0.0125	0.9	6.3	4.6	28.98	0.48
2 mm	0.0253	2.0	6.3	4.7	29.38	0.43
3 mm	0.0559	3.0	8.3	4.9	40.67	0.46
5 mm	0.0413	4.8	4.7	4.8	22.56	0.38
Stacked Commercial Thin Film:						
1*	0.0172	0.3	9.5	N/A	70.88	0.81
2*	0.0326	0.6	9.5	N/A	70.88	0.77
3*	0.0619	0.9	9.5	N/A	70.88	0.97
6*	0.1338	1.8	9.5	N/A	70.88	1.05

*Lengths of the thin films are diameter values

For Part II, commercial biochar pieces were separated by their dry electrical resistance; pieces with less than 15 Ω were selected for electrode construction. Monolithic and thin film electrodes were made from the same processes as those for Part I. Monolithic electrodes were sanded to different thicknesses (summarized in Table III) for investigation. Since thin films cannot easily be made to different thicknesses without changing their bulk density or porosity, the thickness of these electrodes was increased by stacking different numbers of thin films (Table III). Stacking the thin films in the electrochemical cell results in inter-film carbon-carbon particle contacts similar to the intra thin film carbon-carbon particle contacts.

4.2.3 Electrode Materials Characterization

The complexity, size range, and arrangement of internal structural elements of the maple and pine biochar were investigated with SEM imaging in the axial orientation of biomass growth direction using the Hitachi SU3500 (Figure 4.2). Specific surface area was determined through physisorption on a Quantachrome Autosorb-1. Both nitrogen and carbon dioxide gas physisorption tests were applied to probe the micro-macropore range. Elemental analysis (CHN) was conducted

on the different biochar samples to determine the carbon content with an Exeter Analytical Inc. CE-440. Surface composition of the biochar was investigated with X-ray Photoelectron Spectroscopy (XPS) at the Ontario Center for the Characterization of Advanced Materials (OCCAM) using a Thermo Fisher Scientific K-Alpha.

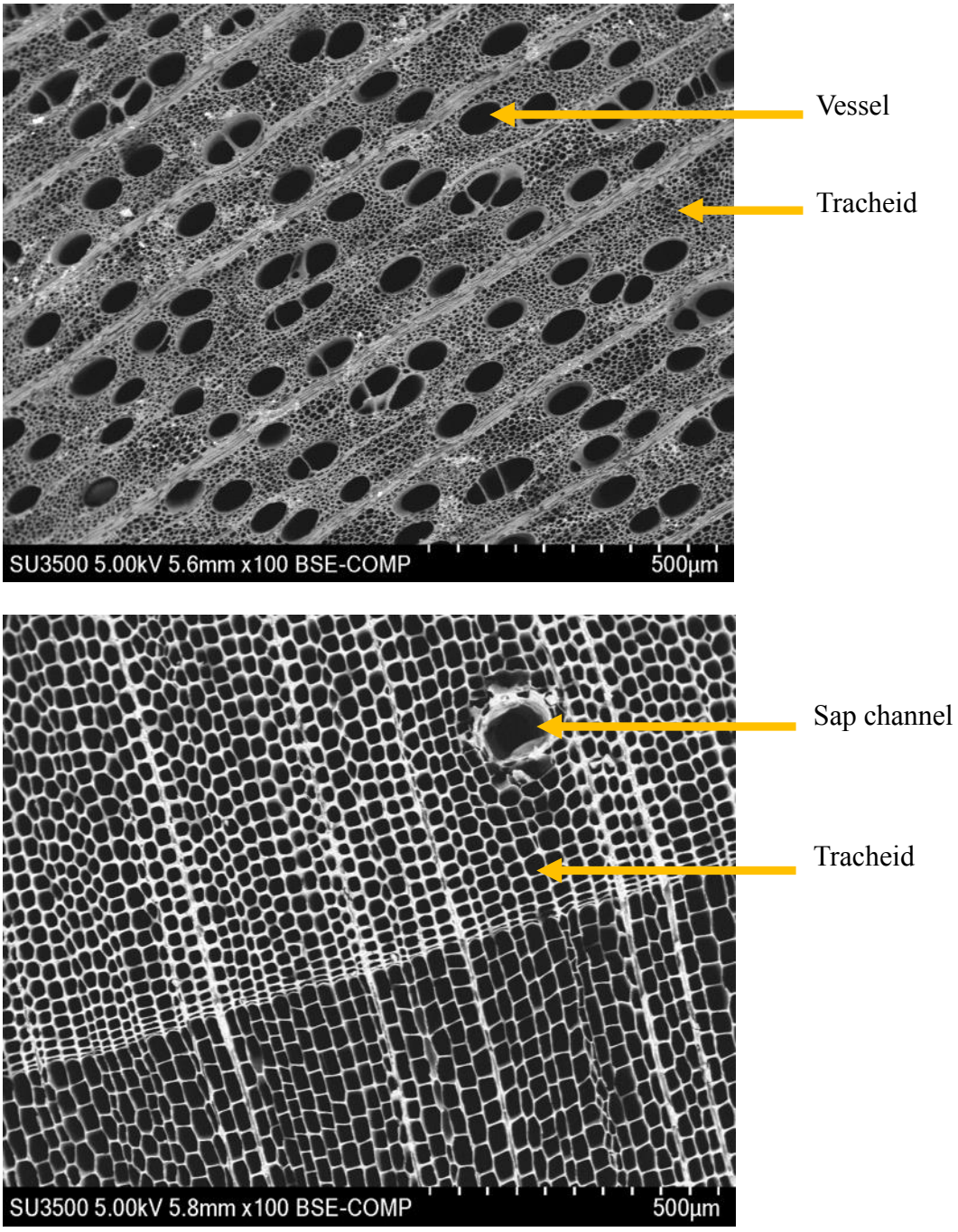

Figure 4.2 BSE SEM images down the axial direction of maple wood biochar (top) and pine wood biochar (bottom).

4.2.4 Electrochemical Characterization

A conventional supercapacitor test cell with symmetrical electrodes was used with a polyphenylene sulfide (Ryton®) porous separator and 4M KOH aqueous electrolyte (Figure 4.3). Current collectors were made of nickel mesh with the ends twisted into wire contacts for connection to the Metrohm Autolab PGSTAT302N potentiostat. The current collectors, electrodes, and separator sandwich were held together between Lucite® plates fastened with nuts and bolts. The cell was hermetically sealed in a Teflon jar and the head space continuously purged with nitrogen gas. The electrodes were allowed to sit and soak in the electrolyte for one week prior to any electrochemical testing.

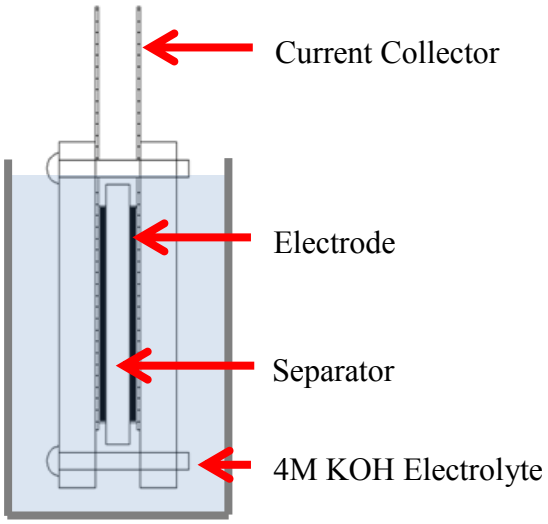

Figure 4.3. Standard supercapacitor electrochemical test cell

One of the benefits of potassium hydroxide electrolyte is its small ion size. The diameter of a bare K^+ ion is 1.33 Å, while the solvated cation has a 3.31 Å diameter [76]. The diameter of bare OH^- is approximately that of water, 2.76 Å [77]. Monovalent cations are found to adsorb in the hydrated state, whereas anions can adsorb as bare ions [24]. However, the exact pore sizes which these ions can and cannot fit into is still unclear.

A two-electrode setup was used for both a cyclic voltammetry (CV) pretreatment as well as galvanostatic cycling (GC). A CV pretreatment of 250 cycles between -0.8 V and 0.8 V at a 10 mV/s scan rate was used to electrochemically remove chemisorbed and physisorbed oxygen. The

CV curves were qualitatively analyzed for pseudocapacitive contributions [78]. GC measurements were conducted between -0.8 V and 0.8 V across a range of current densities (5-500 mA/g). Five runs were completed at each current density for data replication. Data collected from the GC measurements was used to calculate specific capacitances of the electrodes at different charge/discharge rates. Current densities were normalized to the average mass of the electrodes under review, which is a common method for supercapacitor electrodes with high specific surface areas [47]. The geometric areas of the electrodes in contact with the current collector were similar (Table III).

Ohmic drops, or iR drops, appear as instantaneous voltage losses that occur upon initial discharge in the GC cycles. They are representative of internal resistances across the device. Ohmic drops are reported for the cells of each type of electrode and were calculated using the average of the discharge voltage drops during the 100 mA/g current density run (Equation 1). The factor of 2 included in the denominator of Equation 1 is due to the switch from charge to discharge.

$$R_{Ohmic} = \Delta V_{IR}/2I_{discharge}$$

Equation 1. Ohmic drop calculation

Specific capacitances are calculated with GC data based on Equation 2, where I is the charge/discharge current (A), m is the mass of the two electrodes (g), and $\Delta t/\Delta V$ is the inverse of the GC discharge (or charge) slope after the iR drop (s/V) [79]. The charge processes occur from 0 V to 0.8 V and -0.8 V, while discharge processes occur from 0.8 V and -0.8 V to 0 V. The resulting specific capacitance, C_m, is in F/g. It is important to note that this calculated value is the device specific capacitance, not the electrode specific capacitance, which is four times larger [80]. Often, authors will report the higher electrode value in literature; clarification must be made for appropriate comparison.

$$C_m = \frac{I * \Delta t}{m * \Delta V}$$

Equation 2. Specific capacitance calculation from GC data

Electrical Impedance Spectroscopy (EIS) was implemented to investigate frequency dependent resistances, or impedances, of the different electrodes. For the EIS cell setup, a CH Instruments Hg/HgO reference electrode was placed directly behind the Lucite® sheet adjacent to the working electrode, with a small capillary drilled through the sheet to enable an electrical pathway through the highly conductive KOH solution (Figure 4.4). A 10 mV sine wave perturbation tested a frequency range of 100kHz – 0.01 Hz. Impedance measurements are of the working electrode only.

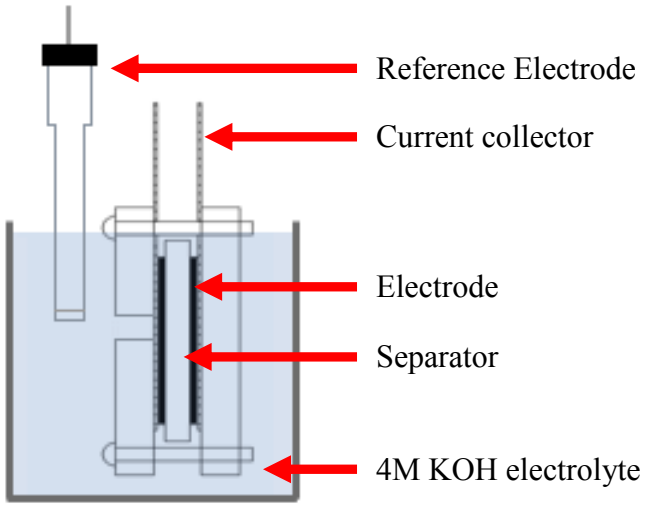

Figure 4.4 Three electrode electrochemical cell setup illustrating the reference electrode position behind the working electrode.

Electrical Impedance data was modelled using an appended version of the equivalent circuit model developed by Suss et al. for their bimodal porous carbon aerogels [81]. In their model, elements are arranged to account for the different sizes of transport pores (diameter on the order of microns) and storage pores (diameter on the order of nm). From a theoretical point of view, transport pores extend throughout the thickness of the electrode and are lined with much smaller storage pores (illustrated in Figure 4.5). Both the transport and storage pores are parameterized by a resistance and a capacitance, which are then normalized with the known physical values of the electrodes. This model assumes that pores within either of the two categories are of uniform cross section, that pores are completely filled with electrolyte, that storage pores are equally distributed along transport pores, and that the intrinsic resistance of the carbon is negligible. While biochar in this study has a broader pore size distribution than the aerogels tested by Suss et al., it has a similar structure and pore dimension. In Chapter 3, storage pores were found to occur along the cell walls

of the macrostructural elements. Other models such as those with anomalous diffusion processes ([82]) and a larger pore size distribution ([23]) were considered, but there is a trade-off between model complexity and the "realness" of the parameters. The model opted for offers a balance between simplicity of parameterization while also providing considerations for the electrode structure.

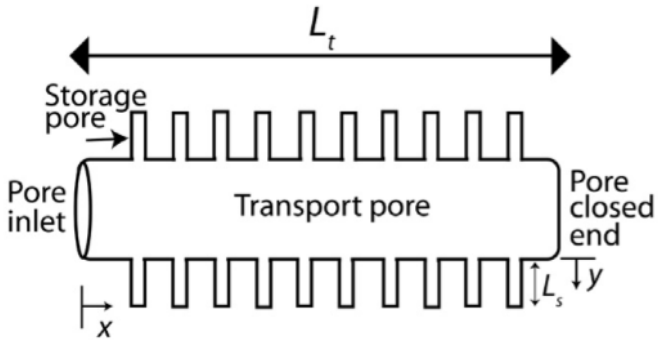

Figure 4.5. Conceptualized drawing of the bimodal pore distribution across the thickness of an electrode(L_t)

The modifications to Suss et al.'s circuit account for the equivalent series resistance and impedance of the current collector-electrode interface in the high frequency regime [83]. The equivalent series resistance includes the potentiostat wiring, connections between the potentiostat cables and the cell, and the aqueous electrolyte. A Randles circuit with a constant phase element (CPE) as the capacitive component is used to model the semi-circle Nyquist plot impedance response that arises from the current collector-electrode interface. CPEs are put in place of capacitance electrodes for rough or porous electrodes [84]. A capacitance occurs at high frequencies due to the solid-solid interface with surrounding electrolyte ions. The resistive component is largely attributed to contact resistance, which has shown dependencies on both loading pressure and surface topology [83], [85]. A power law relationship has been established between loading pressure and conductivity of rough surfaces [85]. Precautions were taken to apply uniform pressure with the nuts and bolts to all of the cells, however, it has been found that negligible capacitance improvement has resulted from increased loading pressure (capacitance values were indirectly compared in this study through CV current measurements) [86]. As a result, loading pressure is not expected to influence the specific capacitive response. The model used for the impedance response is described by Equations 3-7.

$$Z_{TOTAL} = R_{ESR} + Z_{INT} + Z_{WE}$$

$$Z_{INT} = \left[\frac{1}{R_{INT}} + Q_{INT}(i\omega)^{n\_INT}\right]^{-1}$$

$$Z_{WE} = (R_T Z_T)^{1/2} coth\left[(R_T/Z_S)^{1/2}\right]$$

$$Z_T = \frac{Z_S \omega}{i - \omega C_T Z_S}$$

$$Z_S = (1-i)\left(\frac{R_S}{2\omega C_S}\right)^{1/2} coth\left[(1+i)(\omega R_S C_S/2)^{1/2}\right]$$

Equations 3-7. System of equations for the mathematical model used to model impedance response of the working electrode, modified version of the model described by [81]

The impedance model includes 8 parameters: R_{ESR}, R_{INT}, Q_{INT}, $n_{\_INT}$, C_T, R_T, C_S, and R_S, described below. In Equations 3-7, Z_{TOTAL} is the total impedance, R_{ESR}, is the equivalent series resistance, Z_{INT} is the impedance of the solid-solid current collecter-electrode interface, and Z_{WE} is the impedance from the working electrode. Z_{INT} is made up of a resistance R_{INT} (largely a contact resistance), and a CPE capacitance, defined by Q_{INT} and $n_{\_INT}$. The impedance of the transport pores, Z_T and storage pores, Z_S, are each parameterized by a capacitance, C_T and C_S, as well as a resistance, R_T and R_S, respectively. ω is the angular frequency, $2\pi f$. The mathematical model is fitted to the raw data using a complex non-linear least squares (CNLS) algorithm. This process is mostly automated through a Python script (8.1 Appendix A). First guesses of parameter values are based on the raw Nyquist plot response and different initial values are applied to test for variation of model response. The quality of the fit is evaluated through a root mean squared error value.

Although EIS measurements provide capacitance values for a supercapacitor cell, the validity of these values has come into question by many researchers. Specifically, EIS derived capacitances are often smaller than those measured through GC or CV techniques, due to limitations of the ability to correctly model the EDL [87]. In addition, the EIS measurement process for capacitance does not relate to how the devices are charged and discharged in real-world applications. The relative values of the EIS calculated capacitances can be compared between the different electrode types and are reported, but their absolute values should not be compared beyond this scope.

Kramers-Kronig relations were analyzed to validate the collected EIS data. The Nova 1.11 software used with the potentiostat automates this process. In this analysis, the real part of the impedance is calculated from the imaginary part, and vice versa. In order to satisfy the Kramers-Kronig relations, the calculations are made based on four criteria: linearity, causality, stability, and finiteness. The calculated values are then compared to the experimental value, and the error residuals for the real (Z') and imaginary (-Z") impedance can be plotted as a percentage. The biggest potential source of poor data quality is drift, either from the reference electrode or electrode contamination. It is unlikely that nonstationary impedances will appear in this system, but if so, they will be identified by the Kramers-Kronig analysis.

4.3 Results and Discussion

4.3.1 Physical and Chemical Characterization

SEM images of the axial orientation of maple and pine wood are shown in Figure 4.2. These images include labels of the main internal structural elements of the biomass precursor. The more uniform macrostructure of pine biochar is immediately apparent. The primary transport channels in the axial direction for maple biochar are vessels which are approximately 50 – 100 μm in diameter, and tracheids, which range 2 – 20 μm in diameter. Pine wood does not have vessels; its tracheids, ranging 5 – 40 μm, have a larger average diameter than those of maple. The sap channel seen at the top of the pine SEM image of Figure 4.2 is not a regularly occurring feature. The axial direction of monolithic biochar is oriented in the direction of current flow in the supercapacitor cell, and the abovementioned elements may act as large transport pores through the thickness of the electrode.

N_2 BET physisorption data showed modest specific surface areas of 172 m^2/g, 161 m^2/g, and 95 m^2/g for in-house pyrolyzed maple, pine, and commercial biochar, respectively. These values are comparable to other non-activated biochar seen in literature [6]. The N_2 isotherms are shown in 8.2 Appendix B. The isotherm types are not readily distinguished and appear to be a cross between Type I and Type II. Other researchers have reported difficulties in N_2 measurements of biochar due to very long equilibrium times and discerned Type I isotherms with little mesoporosity [88].

The small hysteresis behavior indicates that the larger mesopores are easily accessed. Activated carbons used in commercial devices often have BET SSA's upwards of 2000 m^2/g, and therefore the specific capacitance values from the biochar are expected to be lower. Difficulties occurred when trying to fit the N_2 isotherm response to an NLDFT model, particularly in the mesoporous range, giving large fitting errors of ~10%. As a result, it was not possible to obtain accurate pore size distributions of biochar mesoporosities. Tests were repeated on different autosorb instruments at the University of Toronto with similar results.

Physisorption measurements were also made with CO_2 gas and analyzed with the ASiQwin software using the NLDFT slit pore isotherm. Carbon dioxide molecules are smaller than nitrogen, probe sub-nanometer pores much faster, and testing can be done at higher temperatures (0°C) [55]. These measurements take less time and are associated with less error [55]. Plotted pore size distributions are shown in 8.3 Appendix C. These are similar for all biochar tested, and the majority of pore volumes are from pores of 0.4 – 0.7 nm diameter. CO_2 SSA's for maple and pine in-house pyrolyzed biochar were 487 m^2/g and 527 m^2/g, respectively. Commercial biochar had a CO_2 SSA of 387 m^2/g. These values seem high compared to the negligible microporosity observed with N_2 adsorption. Either there were difficulties with the low-pressure nitrogen data, or the CO_2 probed pores are on the smaller end of the 0.3 – 1.6 nm size range, which may not be accessible to the electrolyte ions [26]. It is possible for artifacts to skew isotherm data, but errors such as these cannot be avoided [55]. Regardless, the total SSA is comparable to literature values [6].

CHN data of the maple, pine, and commercial maple biochar all show carbon contents above 90 wt.%. Hydrogen and nitrogen compositions were similar for all three materials. Slow-pyrolyzed wood biochar has low ash content, and the remaining mass contribution primarily consists of oxygen [6].

Table IV. CHN Mass % Composition Data of the Electrode Materials.

	Carbon (wt.%)	Hydrogen (wt.%)	Nitrogen (wt.%)	Remaining (wt.%)
In-house maple	93.53 ± 0.45	1.18 ± 0.02	0.31 ± 0.03	4.98 ± 0.49
In-house pine	95.69 ± 0.22	1.32 ± 0.02	0.20 ± 0.05	2.79 ± 0.18
Commercial maple	91.84 ± 2.62	1.31 ± 0.05	0.64 ± 0.02	6.23 ± 2.70

XPS results show the atomic compositions of the three biochar surfaces. The contributions to overall composition from the carbon C1s and oxygen O1s spectra are compared in Table V. The results of a more detailed investigation into the oxygen groups of the O1s spectra can be seen in Table VI.

Table V. XPS Surface Atomic Compositions of Biochar Electrode Materials.

	Carbon C1s (At. %)	Oxygen O1s (At. %)
Maple	87.06	12.94
Pine	92.73	7.27
Commercial Maple	88.16	11.84

It has been found that only certain oxygen functional groups contribute to pseudocapacitive faradaic reactions depending on the electrolyte [16], [89]. For this biochar in alkaline KOH solution, only the carboxyl group is known to contribute to pseudocapacitance. As it is difficult to deconvolute O1s spectra peaks, there may be some small contributions from latent oxygen groups, but this is likely negligible. Furthermore, the relative carboxyl atomic %'s of 1.73, 1.04, and 2.45 in maple, pine, and commercial biochar, respectively, are not expected to make significant pseudocapacitive contributions to the overall device capacitance. Any chemisorbed and physisorbed oxygen should be removed during the CV pretreatment process.

Table VI. O1s Spectra Response for Biochar Electrode Materials.

		Maple		Pine		Commercial Maple	
Oxygen Group	**Approximate Peak Binding Energy (eV)**	**At. %**	**Rel. At. %**	**At. %**	**Rel. At. %**	**At. %**	**Rel. At. %**
O1s, Carboxyl type	531.29	13.38	1.73	14.33	1.04	20.68	2.45
O1s A, Carbonyl type of ester	532.23	20.00	2.59	36.19	2.63	25.93	3.07
O1s B, Ether type in ester and anhydride	533.70	22.88	2.96	37.90	2.76	32.93	3.90
O1s C, Chemisorbed	535.65	36.14	4.68	9.13	0.66	13.25	1.57
O1s D, Physisorbed	538.57	7.6	0.98	2.45	0.18	7.21	0.85

4.3.2 Part I Electrochemical Testing

GC calculated specific capacitances are plotted against current density for the maple and pine monolithic and thin film electrodes in Figure 4.6. Specific capacitance values are normalized to the mass of the active biochar in the electrodes. For the thin films, this is 90% of the total electrode mass, as 10% is made up of carbon black and binder which do not provide significant surface area for ion adsorption. Error bars were included in the maple biochar comparison to show their relative size, but were not included in further plots as results were similar and impeded visual clarity. Examples of GC curves for a single charge/discharge process at the different current densities for each of the electrodes are shown in 8.4 Appendix D. Aside from the initial iR drop, the curves are linear for all current densities. This ensures accurate specific capacitances from the calculation method [78]. The 5 mA/g specific capacitance value for monolithic pine biochar was not collected.

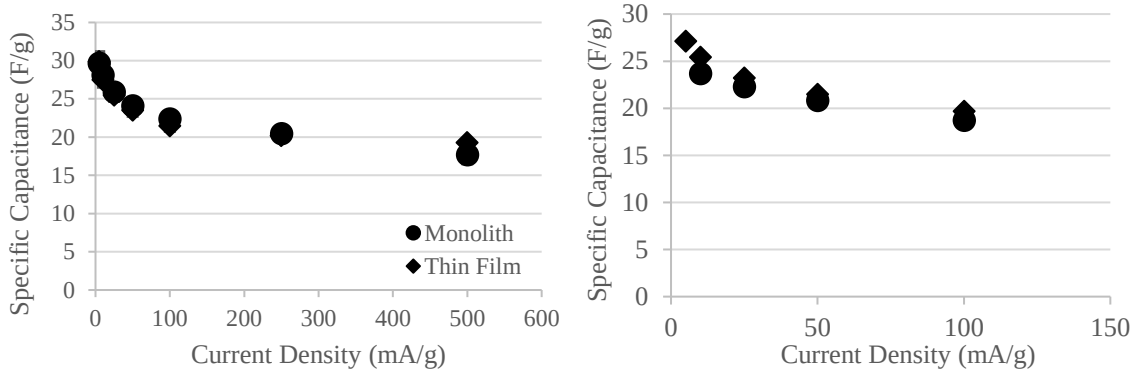

Figure 4.6 Specific capacitance versus current density for in-house pyrolyzed maple (left) and pine (right) monolithic and thin film electrodes.

No statistical specific capacitance difference was seen between the monolithic and thin film electrode structures for either the maple or pine biochar across this current density range. While the internal structural elements of precursor biomass retained in monolithic biochar electrodes do not noticeably facilitate ion migration, they also do not hinder capacitive performance.

Due to their respective sizes and shapes, the electrode structures tested in Figure 4.6 had different total masses. By multiplying the specific capacitance at a 5 mA/g current density by two times the average electrode mass, a total device capacity in Farads is calculated. This is found to be 3.13 F for the monolithic electrode, and 1.12 F for the thin film electrode. It is found that the monolithic structure maintained equivalent specific capacitance performance while also providing ~3x the total capacity stored.

A look at the volumetric capacitances versus current density in Figure 4.7 shows clear performance differences between the electrode structures. The more densely packed thin films outperform the monolithic electrode, and there is no evidence of electrolyte starvation for any of the electrode structures. A larger volumetric disparity is seen between electrodes of the pine and maple biochar, as the monolithic pine electrode has a lower bulk density than maple. Results demonstrate that the internal structures of precursor biomass are too large to actively contribute to any electrical double layer capacitance formation or diffusional processes. As such, the monolithic electrodes are volumetrically less efficient than the thin films as the electrolyte that fills these large pores does not offer additional energy storage contributions.

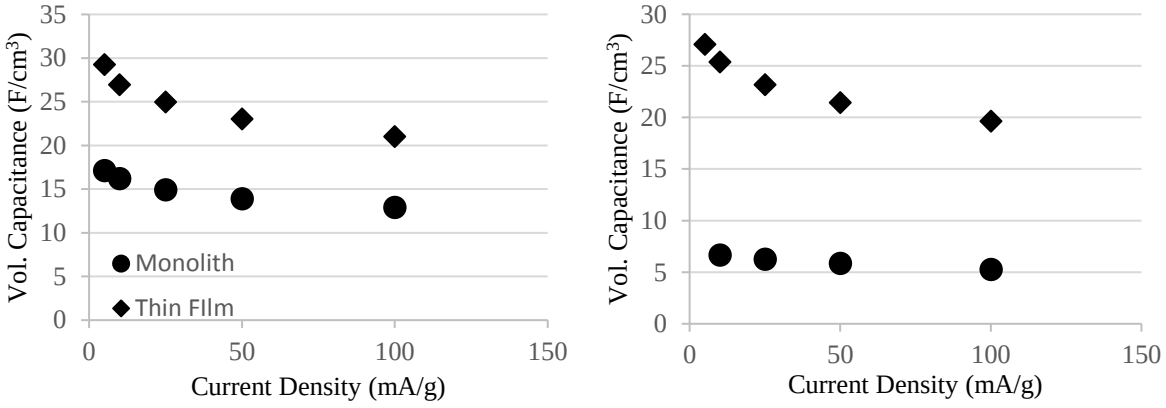

Figure 4.7 Volumetric capacitance versus current density for maple biochar (left) and pine biochar (right) monolithic and thin film electrodes.

The maple biochar consistently outperformed the pine by approximately 10% of the specific capacitance. This is likely due to its slightly higher BET SSA. Although the CO_2 physisorption showed a higher SSA for pine, these pores may be too small to be accessible to the electrolyte. The surface area of the solid-solid interface between the current collector and the electrode was ~50% different between the thin film and monolith electrodes (Table III). However, the strong agreement of specific capacitance values, especially at very low current densities (5 mA/g), suggests this does not affect the results.

Ohmic drop data in Table VII indicate that despite the addition of non-conductive binder, the Part I thin film electrodes have lower resistances across the cell than their monolithic counterparts. Clearly, the intrinsic resistivity of the carbon is not a significant contributor to this resistance. Evidence suggests that the iR drop is largely a product of the contact resistance. Porous thin film carbons are highly compressible compared to monolithic structures, enabling greater loading pressures and lower contact resistances [32], [86]. This is also supported by the EIS response data (Figure 4.8) – the high frequency semi-circle response, indicative of contact resistance, is smaller for the thin film [83]. The pine electrodes have larger iR drop values than the maple. This could be due to the density of the biochar, especially for the monolithic electrodes, as the lower density pine is more fragile than maple and less able to withstand larger loading pressures. Loading pressures applied by screws and nuts were adjusted by hand. While caution was taken to apply uniform pressures across all cells, differences in electrode structures may have facilitated human

error. However, since contact resistance appears to dictate the iR drop, this should not affect the capacitance result [86].

Table VII. Ohmic drop results for Part I electrodes

Electrode	ΔV (V)	R = ΔV/2I (Ω)
Maple Monolith	0.049	4.62
Maple Thin Film	0.017	4.06
Pine Monolith	0.10	16.53
Pine Thin Film	0.042	9.87

Nyquist plots of EIS data and associated model fit of the maple electrodes are included in Figure 4.8. A computer update that occurred during the 5 mA/g pine monolith GC run permanently changed the electrode performance and EIS could not be accurately reported. A summary of the key model parameters EDLC storage is shown in Table VIII. The first 6 data points of the EIS response were truncated, as they resulted from a high frequency artifact created by the mutual inductance of the wires connecting the potentiostat to the cell [90]–[92]. The growing deviation between the model and the raw data in the low frequency regime of the Nyquist plots is common in EIS fitting. This can arise due to differences between real life electrochemical resistances and idealized model behavior, as well as reference electrode drift. Furthermore, as a natural material, the biochar is expected to have a broader pore size distribution than synthetic materials such as carbon aerogels, and different pore sizes have different time constants [93]. A range of time constants results in a curvature of the low frequency response, which is a vertical line in the ideal case. Note that the y-axes are more compressed than the x-axes in Figure 4.8, and that the root mean squared error (RMSE) values of the monolithic and thin film maple electrode fits are quite low – 0.02 and 0.06, respectively. This suggests a good fit of the data.

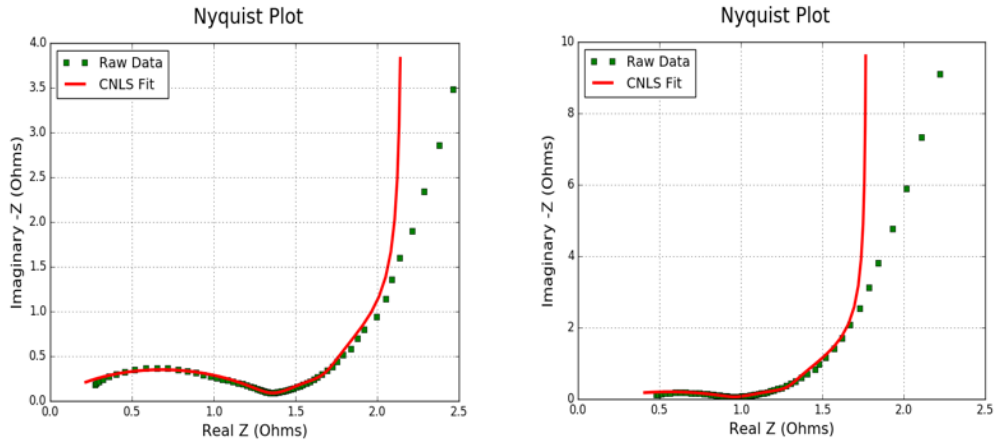

Figure 4.8 Nyquist plots of experimental EIS response and model fit for maple monolithic (left) and maple thin film (right) electrodes.

Table VIII. Summary of Key EIS Fitting Parameters Using Equivalent Circuit Model from Suss et al.

Parameter	Maple Monolithic	Maple Thin Film
R_T (Ω*cm)	6.1	34.7
C_T (F/g)	44.9	55.2
R_S (Ω/BET m^2)	0.8	2.8
C_S (F/g)	39.2	33.7
Electrode Capacitance (F/g)	84.1	88.9
Device Capacitance (F/g)	21.0	22.2
Fit Root Mean Squared Error	0.02	0.06

Resistance values from the Suss et al. circuit component of the EIS fit represent the liquid-filled pores, as solid carbon material resistances are negligible in comparison [94]. From the EIS fit parameters shown in Table VIII, the normalized transport pore resistivity (R_T), which extends the length of the electrode, was several times smaller for the maple monolithic electrode compared to the thin film. The larger resistivity of the thin film can be explained by the addition of non-conductive PTFE binder material. Therefore, even though the monolithic electrode was thicker than the thin film, it was not hindered by internal material resistivity. Device capacitance shows good agreement between the two electrode structures, which is also observed in the GC data.

The idealization of EIS data by the model in the low frequency regime will have affected the resulting C_T, R_T, C_S, and R_S parameter values. Based on the fit comparison in Figure 4.8, capacitance parameters are slightly inflated compared to the true value, while resistance

parameters are lower than reality. These errors are likely minimal however, as evidenced by the small RMSE values.

Error residuals of the real (Z') and imaginary (-Z") impedances from Kramers-Kronig analysis are plotted in Figure 4.9. Minimal error residuals validate the collected EIS results.

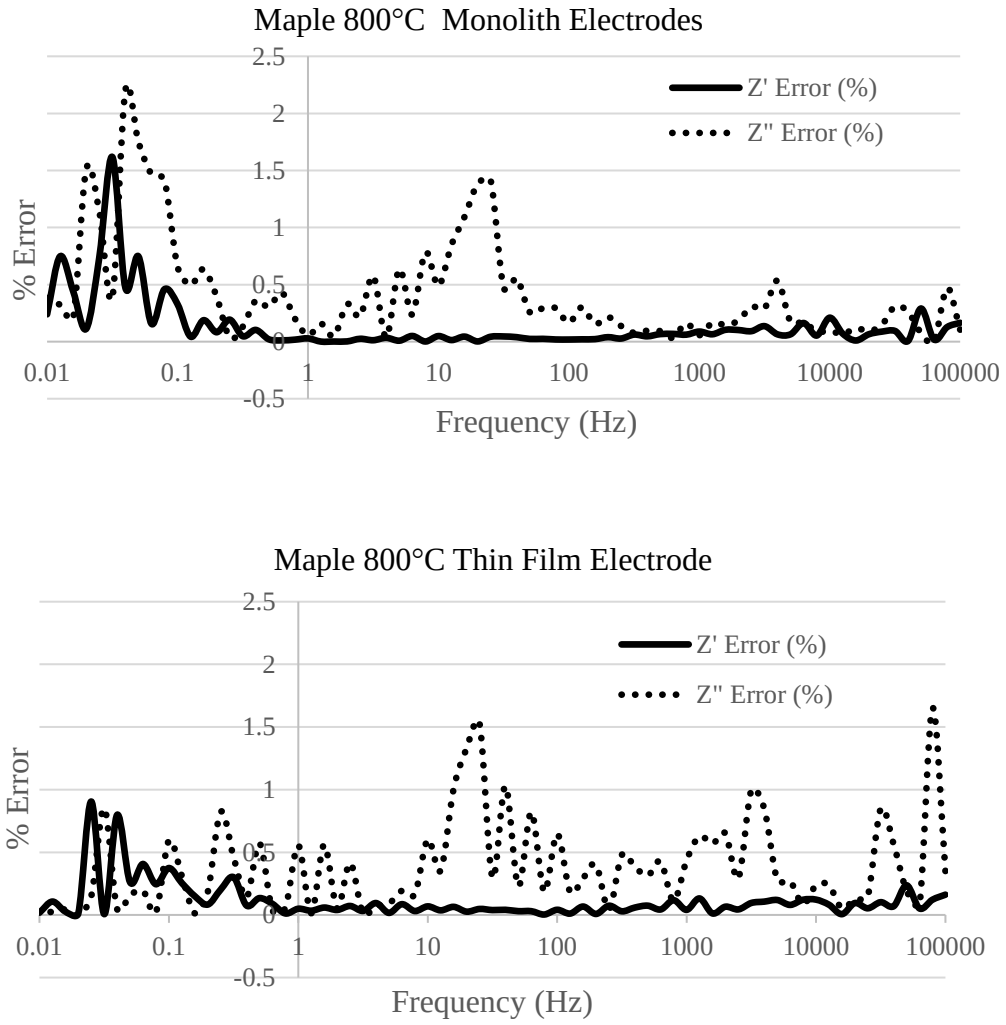

Figure 4.9. Kramers-Kronig error residuals for the EIS fit of the 800°C maple biochar electrodes

4.3.3 Part II Electrochemical Testing

GC calculated device specific capacitances are plotted against current density for monolithic and thin film commercial maple biochar electrodes of different thicknesses in Figure 4.10. Examples

of GC curves for a single charge/discharge process at the different current densities for each of the electrodes are shown in 8.4 Appendix D. All electrodes show ideal linear response; no degradation of performance was seen with regards to the GC curve behavior. Monolithic electrodes showed no change in specific capacitance performance with increasing thickness. Similarly, the 1-3 stacked thin film electrodes have clustered specific capacitances at different current densities as seen in Figure 4.11. The stack of 6 thin films produced a favorable performance anomaly. These results show that it is possible to retain specific capacitance while increasing the thickness of the electrode several times thicker than the status quo for both monolithic and thin film electrode structures.

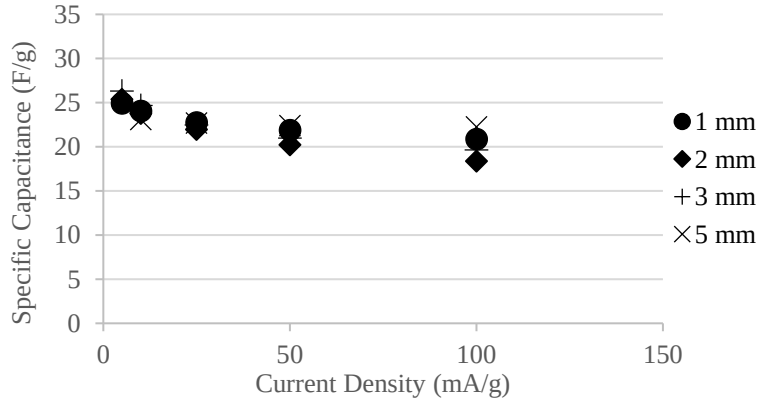

Figure 4.10 Specific capacitance versus current density for commercial maple monolithic biochar electrodes of different thicknesses

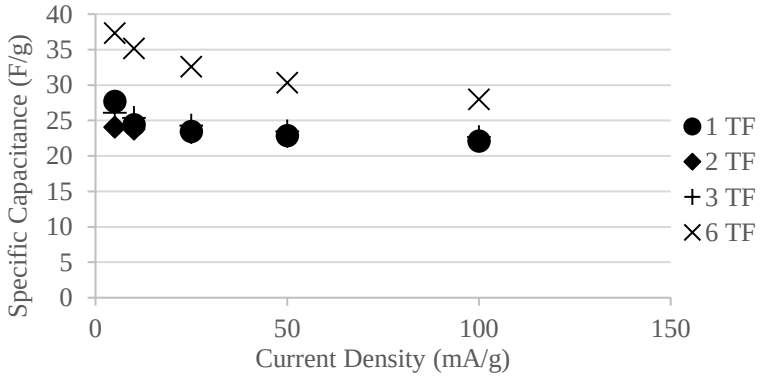

Figure 4.11 Specific capacitance versus current density for stacked commercial maple thin film biochar electrodes

EIS analysis did not show any trends between impedance and electrode thickness. Ohmic drop data is shown in Table IXTable X for the Part II electrodes of varying thicknesses. There is no clear trend between electrode thickness and ohmic resistance. Although the resistance increases

with thickness for the thin films, the monolithic electrode values appear random. This may be due to the more sensitive relationship between contact resistance and loading pressure of the monolithic electrodes.

Table IX. Ohmic drop data for the monolithic electrodes of varying thickness

Monolithic Electrodes	ΔV (V)	R = ΔV/2I (Ω)
1 mm thick	0.024	9.65
2 mm thick	0.025	4.9
3 mm thick	0.038	3.4
5 mm thick	0.061	4.74

Table X. Ohmic drop data for the thin film electrodes of varying thickness

Thin Film Electrodes	ΔV (V)	R = ΔV/2I (Ω)
1 stack	0.003	1.00
2 stacked	0.011	1.68
3 stacked	0.011	1.68
6 stacked	0.098	3.64

4.4 Conclusions

In Part I of this study, it was shown that both monolithic and thin film electrodes constructed from the same biochar material can have equivalent specific capacitance performance. The large internal structures retained in biochar show no influence on charge/discharge processes. Furthermore, the non-conductive binder did not impede specific capacitance performance across the current density range tested. Although monolithic electrodes had lower volumetric capacitance performance, a comparison between maple and pine monolithic structures suggests this could be improved by selecting a denser biomass precursor/biochar.

In Part II of this study, it was found that both monolithic and thin film electrodes can be constructed several times thicker than currently used thicknesses while retaining their specific capacitance performance. The 5 mm thick monolithic electrode is more than 10 times commercial standard.

An electrode thickness that reduced specific capacitance performance was not seen in this study. Due to the low material costs and reduced ratio of ancillary components, there may be application potential for monolithic biochar electrodes in volumetrically non-constricted applications.

5. Unpublished extensions of biochar electrode studies: investigating pyrolysis temperatures, particle sizes in thin films, and ion diffusion during charge/discharge processes

5.1 Introduction – Effects of conductivity on EDL formation

Increasing the conductivity of electrodes has demonstrated positive effects on their capacitive performance. With graphene and sodium-salt polymer derived carbon electrodes, higher conductivities enhance the degree of pore space utilization for EDLC devices, by way of facilitating charge transfer to the smaller, sub-nanometer pores [13]. Similarly, Ranade et al. observed improvements to the specific capacitance from 100 F/g to 120 F/g by increasing the percentage of highly conductive carbon material from 5% to 7% in their thin film powdered electrodes [75]. As such, there is ample reason to test the capacitive performance of more conductive biochar electrodes.

To increase the conductivity of the crack-free monolithic biochar, the upper pyrolysis temperature and process residence time must both be increased, as described by thermal schedule (Table I) of Byrne and Nagle's Patent [39][88]. However, conductivity is not the only property expected to be affected by this change. The pyrolysis process conditions also influence specific surface area, pore size distribution, and chemical composition/surface chemistry. One of the reasons this research is so complicated is due to the inability to isolate and test the effect of a single property.

As pyrolysis temperature increases, larger pores tend to increase in diameter and pore walls get thinner, while there is greater microporosity development as determined through CO_2 adsorption studies [88]. Total specific surface area increases as a result of the production of more sub-nanometer pores.

A loss of surface oxygen groups of biochar has been found to occur with increasing pyrolysis temperature [88]. As described in section 2.1.2 of the literature review, oxygen groups on the surface of biochar can participate in rapid faradaic reactions during electrochemical charge/discharge cycles, contributing to total energy storage capacity of the device. Furthermore,

oxygen groups that do not participate in faradaic reactions can help improve wettability and therefore pore accessibility for EDL formation [13]. By increasing the pyrolysis temperature and residence time, there will likely be performance trade-offs between conductivity and surface oxygen content of the biochar. Pine and maple wood will be pyrolyzed at 600°C and 1000°C, in order to compare data with the results attained from the 800°C biochar in Chapter 4.

The thin films investigated in the previous chapter had particle sizes between 53 and 212 μm. Although the thin film electrode density was almost doubled compared to the maple monoliths, and tripled compared to the pine monoliths, this particle size range still permits the retention of many macrostructural biochar elements, as evidenced by Figure 4.2. In order to test the further elimination of macrostructural elements, the performance and impedance of thin film electrodes of particles sizes less than 53 μm will be tested.

Thin film electrodes made of biochar particles <53 μm will have a higher electrode density and a reduction of the volume of inter-particle void spaces. A decrease in capacitive performance would indicate that these electrodes lack an adequate electrolyte supply for EDL formation. On the other hand, if performance remains the same or improves, it will show that the larger pores retained in the monolithic and 53 – 212 μm particle electrode structures contain significant volumetric inefficiencies.

5.2 Experimental

5.2.1 Pyrolysis Process Conditions

Like the in-house pyrolyzed maple and pine wood at 800°C introduced in section 4.2.1, pyrolysis of biochar at 600°C and 1000°C was also carried out according to the crack-free procedure outlined in the expired US Patent 6,124,028 [39]. Details of the respective temperature schedules for these pyrolysis processes can be found in Table I.

5.2.2 Electrode Fabrication

As in Chapter 4, both monolithic and powder thin film electrode structures were investigated, and followed the same fabrication procedures outlined in section 4.2.2. In addition, thin film electrodes were also made with particles of < 53 μm. The manufacturing process had all the same conditions, except that after sieving, particles of < 53 μm were collected for thin film processing. Average physical properties of the electrodes new to this study can be found in Table XI. For reference, 800°C pyrolyzed thin film (53 – 212 μm particle size) and monolithic electrodes can be found in Table III (Section 4.2.2).

Table XI. Average Physical Characteristics of Electrodes.

Electrodes:	Mass (g)	Thickness (mm)	Length (mm)	Height (mm)	Cross Sectional Area (mm^2)	Bulk Density (g/cm^3)
Maple 1000°C Monolithic	0.0434	2.0	5.3	7.2	38.16	0.59
Maple 1000°C Thin Film*	0.0198	0.3	9.5	N/A	70.88	0.93
Pine 1000°C Monolithic	0.0296	2.0	7.2	7.2	51.84	0.29
Pine 1000°C Thin Film*	0.0168	0.3	9.5	N/A	70.88	0.79
Maple 800°C Thin Film, particles <53 μm	0.0283	0.3	9.5	N/A	70.88	1.33
Pine 800°C Thin Film, particles <53 μm	0.0302	0.3	9.5	N/A	70.88	1.42

*Lengths of the thin films are diameter values

5.2.3 Electrode Materials Characterization

Electrode materials characterization was conducted using the same methods used in Chapter 4. Details of these techniques can be found Sections 4.2.3 and 3.2. In addition, dry conductivity measurements of the different electrodes were made. Single electrodes were sandwiched between two nickel mesh current collectors, and clamped together in the Lucite® cell structure. Resistance was measured using a multi-meter, and the value can be inverted to get the conductance. The resistance measured incudes the intrinsic values of the biochar and the nickel, as well as the nickel-

biochar interface contact resistances. Although it is not possible to deconvolute the contributions to resistance using this method, relative differences between the biochar can quickly be compared.

5.2.4 Electrochemical Characterization

Same as in Chapter 4. Details are found Section 4.2.4.

5.3 Results and Discussion

5.3.1 Physical and Chemical Materials Characterization

The results of CHN Elemental analysis on the 600°C and 1000°C maple and pine biochar are shown in Table XII (800°C results were shown in Table IV, Section 4.3.1). A direct correlation is seen between increasing pyrolysis temperature and carbon content, while hydrogen and oxygen (remaining) weight % decrease.

Table XII. CHN Mass % Composition Data of the 600°C and 800°C In-house pyrolyzed Electrode Materials.

	Carbon (wt.%)	**Hydrogen (wt.%)**	**Nitrogen (wt.%)**	**Remaining (wt.%)**
Maple 600°C	90.76 ± 0.17	2.86 ± 0.03	0.29 ± 0.07	6.09 ± 0.22
Maple 1000°C	97.60 ± 0.18	0.86 ± 0.08	0.32 ± 0.07	1.22 ± 0.29
Pine 600°C	90.20 ± 0.87	3.03 ± 0.11	0.18 ± 0.06	6.70 ± 0.98
Pine 1000°C	95.99 ± 0.75	0.87 ± 0.09	0.43 ± 0.19	2.71 ± 0.80

In making the monolithic electrodes, an observable difference was found in the relative brittleness of the different temperature pyrolyzed biochar. The 600°C samples were much softer and easier to shape with silicon carbide paper, while the 1000°C samples were brittle and easily chipped.

Dry conductivity measurements are summarized in Table XIII. As expected, the 1000°C pyrolyzed samples had the best results, and were an order of magnitude better than the 800°C values. Despite showing ~90 wt. % carbon through CHN analysis, the conductivity of the 600°C monolithic electrodes was several orders of magnitude worse than the 800°C or 1000°C samples. As a result,

it was not used as a supercapacitor electrode. Clearly, a critical step of the carbonization processes occurs between 600 - 800°C.

Table XIII. Average dry conductivities (in Siemens/cm) of in-house pyrolyzed monolithic biochar electrodes:

	Pyrolyzation Temperature		
Biomass Precursor	**600°C (S/cm)**	**800°C (S/cm)**	**1000°C (S/cm)**
Maple	4.97 E-07	4.22	20.01
Pine	3.51 E-07	3.70	16.04

As a general trend, the conductivity of maple biochar was slightly higher than the pine despite lower carbon content. This is likely due to the density differences and associated number of carbon-carbon contact points within the respective monoliths. The density of maple biochar is approximately double that of the pine wood due to biomass precursor structures.

The oxygen O1s spectra of the x-ray photoelectron spectroscopy analysis for the 1000°C biochar are summarized in Table XIV; full results can be found in 8.5 Appendix E. Compared to the 800°C pyrolyzed biochar the same oxygen groups occur in slightly less relative atomic percent.

Table XIV. O1s Spectra Response for 1000°C pyrolyzed Biochar

		Maple		Pine	
Oxygen Group	**Approximate Peak Binding Energy (eV)**	**At. %**	**Rel. At. %**	**At. %**	**Rel. At. %**
O1s, Carboxyl type	531.29	20.70	1.89	14.59	0.99
O1s A, Carbonyl type of ester	532.23	36.96	3.37	36.36	2.47
O1s B, Ether type in ester and anhydride	533.70	28.13	2.57	35.09	2.39
O1s C, Chemisorbed	535.65	12.30	1.12	10.60	0.72
O1s D, Physisorbed	538.57	1.91	0.17	3.36	0.23

BET N_2 physisorption results of the maple and pine pyrolyzed at 1000°C are comparable to the 800°C samples; 202 m^2/g and 157 m^2/g, respectively. Slightly higher CO_2 SSAs of 616 m^2/g for maple and 637 m^2/g for pine indicate a higher degree of microporosity, and also suggest an overall smaller average pore diameter.

5.3.2 Anomalous Pseudocapacitive Growth Observed in the 1000℃ Pyrolyzed Electrodes

0 Appendix F includes the progression of CV pre-treatments for all of the in-house pyrolyzed biochar electrodes. As mentioned, this pre-treatment, a CV run of 250 cycles between -0.8 and 0.8V at 10 mV/s, is used to remove chemisorbed and physisorbed oxygen groups, electrochemically facilitate pore filling, and ultimately achieve a stable capacitive response in the device prior to galvanostatic cyclic tests.

In an ideal supercapacitor device, the CV curve behavior appears rectangular – constant current values across the voltage range during respective charge and discharge cycles. With increasing pore filling during the CV pre-treatment, the rectangular curve produced by an ideal supercapacitor would respond by extending outward in both the positive and negative y-directions. This would reflect an increase in the electric double-layer capacitance of the electrodes. This occurred in most of the electrodes tested and is somewhat seen in Figure 5.1.

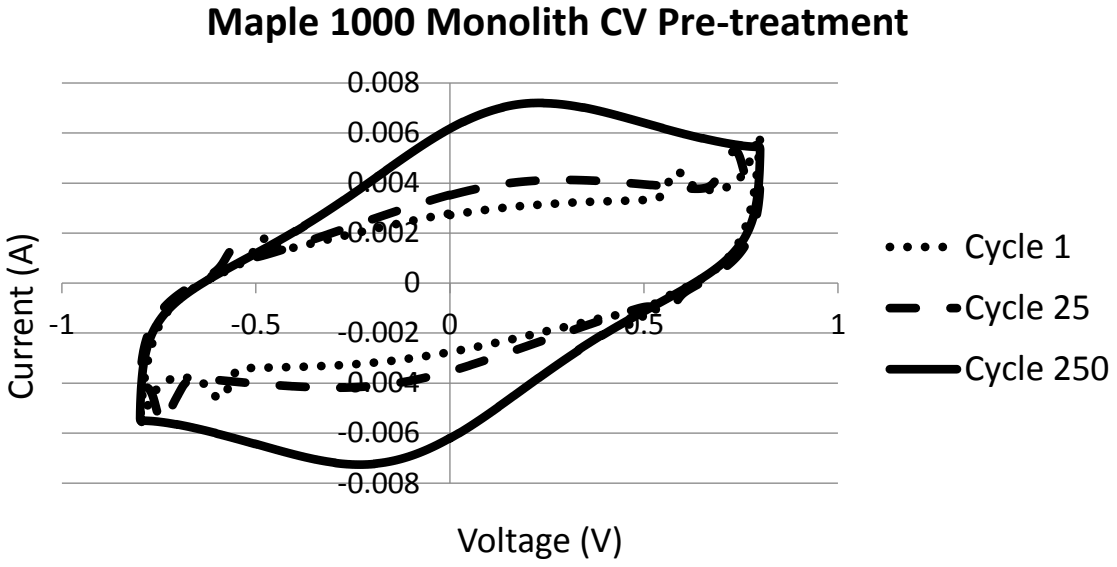

Figure 5.1. Cyclic voltammetry pretreatment cycle progression for the 1000°C maple monolith electrode cell

While an increase in the current at the extremes of the voltage range (-0.8 V and 0.8 V) confirms the growth of EDLC performance with CV progression in most of the electrodes, a broad, reversible pseudocapacitive-type peak also appears to grow with cycling. These peaks were found to center between 0 – ±0.25 V, and their growth is much more apparent in the electrodes that were pyrolyzed at 1000°C.

Although pseudocapacitive peaks are typically much more narrow than those seen in 0 Appendix F, similar broad behaviors were observed in carbon electrodes with concentrated 6M KOH electrolyte [16]. Oh et al. relate the contributions of carboxyl and phenol groups to the broad pseudocapacitive peaks in alkaline electrolyte, while sharper peaks were seen with an acidic electrolyte [16]. Although their work resolves the uncharacteristic breadth of the peaks, no one has reported pseudocapacitances increasing with cycling. This phenomenon becomes further confusing when analyzing the biochar surface chemistries. Despite having lower oxygen content, the 1000°C pyrolyzed samples have more evident pseudocapacitive peaks.

This growing pseudocapacitive anomaly is believed to be the result of a KOH chemical oxidation process enabled by the CV pre-treatment. The general mechanism of carbon oxidation is detailed in Figure 5.2. Six of the eight steps involved in the oxidation process are facilitated by the ion migration to/from the carbon surfaces during the CV cycling, as well as the adsorption/desorption energy storage/delivery mechanisms of an EDLC. Although high temperatures are typically expected for oxidation processes, reactions with oxidizing solutions can occur at room temperature [32]. Furthermore, a similar oxidation process with dilute nitric acid was reported by Jiang et al., whereby a simple overnight soak of carbon electrodes in the solution resulted in a sevenfold increase in capacitive performance [5]. XPS results of their carbon materials determined an increase in the amount of hydroxyl and carboxyl surface oxygen groups after the soak, while no change was seen in the BET surface area measurements [5]. Both KOH and nitric acid are known chemical oxidizing agents, and therefore a similar effect on carbon surfaces is likely [95].

1. Diffusion of oxygen to the outer surface of carbon particle (film diffusion).
2. Diffusion of oxygen through pores/cavities of carbon particle.
3. Adsorption of oxygen onto the carbon surface (physisorption).
4. Formation of oxygen–carbon bonds (chemisorption).
5. Breaking of carbon–carbon bonds.
6. Desorption of reaction products from the carbon surface.
7. Diffusion of reaction products through pores/cavities of carbon particle.
8. Diffusion of reaction products away from outer surface of carbon particle (film diffusion).

Figure 5.2. Generalized mechanism of carbon oxidation, from [95]

To confirm the growth of pseudocapacitive contributions in biochar electrodes, CV pre-treatment processes were repeated for the Maple and Pine 1000°C monolith electrodes. A comparison of the first and second pre-treatment processes for the Maple 1000°C monolith electrode cell is displayed in Figure 5.3. The continued growth of the pseudocapacitive peaks with cycling progression is clearly evident.

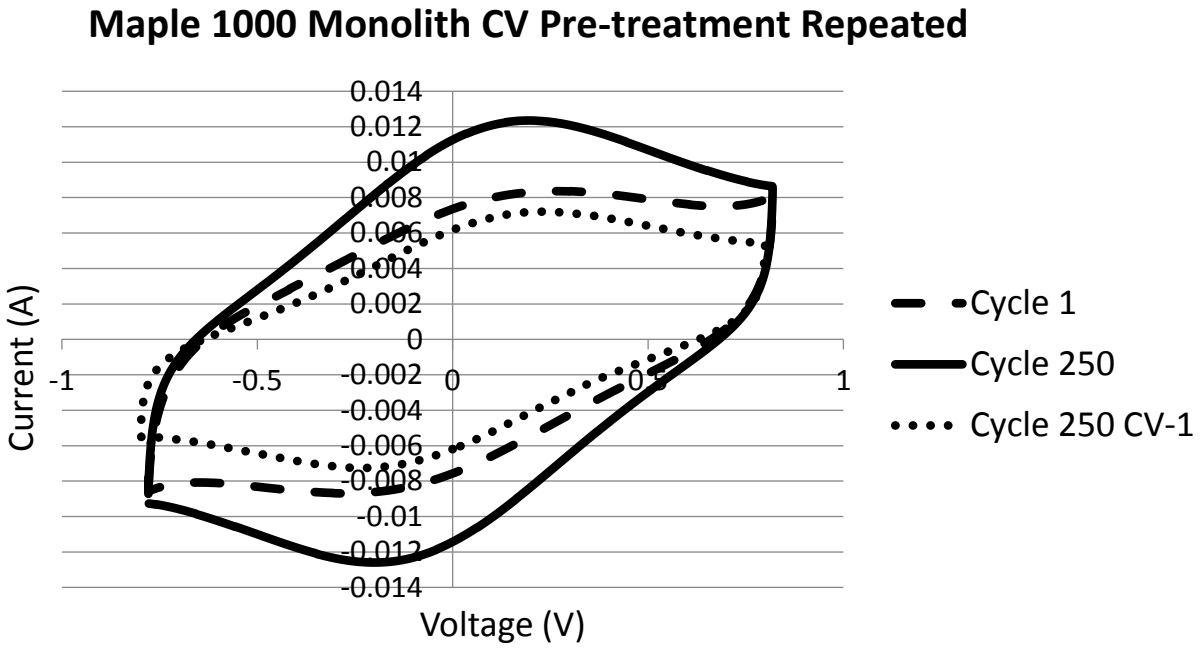

Figure 5.3. Repeated CV pre-treatment cycle progression of the maple 1000°C monolith electrode cell

In addition, XPS analysis was performed on the crushed and washed 1000°C maple and pine monolith electrodes post-CV pre-treatment to determine any change in surface chemistry from the

original biochar. Noticeable differences were observed in the carbon and oxygen surface groups. Table XV compares the XPS results for the carbon surface groups of 1000°C maple biochar. Results for pine (similar), as well as the XPS spectra can be found in 8.5 Appendix E. Initially, the 1000°C pine and maple biochar consisted of over 90% C1s graphite-type carbon. After pre-treatment, graphite-type carbon made up approximately 65% in these biochar, with the remainder composed of a variety of oxygenated carbon compounds. Total atomic oxygen increased by a factor of ~2.5 for the pine biochar, but only a slight increase (~15%) was seen for the maple biochar. Differences were also found in the respective O1s oxygen spectra, but the broad peaks of superimposed surface groups are difficult to accurately deconvolute.

Table XV. Comparison of XPS C1s spectra results for maple 1000°C biochar before and after the CV pre-treatment process

Maple 1000°C Biochar			**Maple 1000°C Biochar Post CV**		
	Peak Binding Energy	Atomic %	Carbon Group	Peak Binding Energy	Atomic %
C1s	284.78	90.76	C1s	284.61	66.08
C1s A	286.23	5.08	C1s A	285.92	16.57
C1s B	287.90	0.00	C1s B	287.54	6.34
C1s C	289.94	1.56	C1s C	289.05	4.22
C1s D	283.78	2.58	C1s D	290.74	3.88
			C1s E	283.61	2.90

From the CV curves of 0 Appendix F, the absence of an equally large pseudocapacitance growth of the 800°C electrodes is apparent. Furthermore, the 800°C electrodes curves are more representative of rectangular, ideal EDLC behavior. This is because of the higher initial amount of oxygen surface groups on the 800°C electrode samples, as shown by comparing the O1s spectra (Table VI versus Table XIV). The development of surface oxygen groups during pre-treatment cycling of the 800°C is less substantial, and these groups make smaller relative contributions to the total capacitive performance.

5.3.3 Pyrolyzation Temperature Effects on Electrochemical Performance

Examples of the GC curves of the 1000°C pyrolyzed electrodes are included in 8.4 Appendix D. The voltage versus time behavior deviates from the ideal linear EDLC response and instead show much more curvature. The curvature in the upper voltage range appears as a more aggressive voltage loss than conventional Ohmic drop, while that of the lower voltage range would include the pseudocapacitive response noticed in the 0 – ± 0.25 V range of the CV plots. As such, the calculated capacitances from the GC data are likely overestimated compared to their true value. Specific capacitances from GC measurements at different current densities are displayed in Figure 5.4 and Figure 5.5 for the 1000°C maple and pine biochar electrodes, respectively. Despite higher total surface areas, carbon contents, pseudocapacitive contribution, calculation overestimation, and dry conductivities, the 1000°C pyrolyzed maple and pine electrodes had noticeably lower capacitive performance than their 800°C counterparts (~5 F/g less, or ~20%, at 5mA/g current density). Error bars were included for all data points as they tended to be larger than in the 800°C results, particularly for the pine biochar, due to the curvature of the GC response.

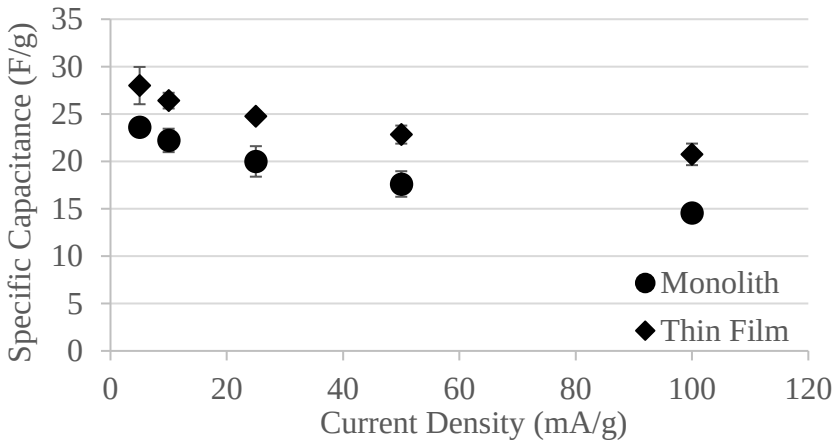

Figure 5.4 Specific capacitance versus current density for in-house pyrolyzed maple at 1000°C

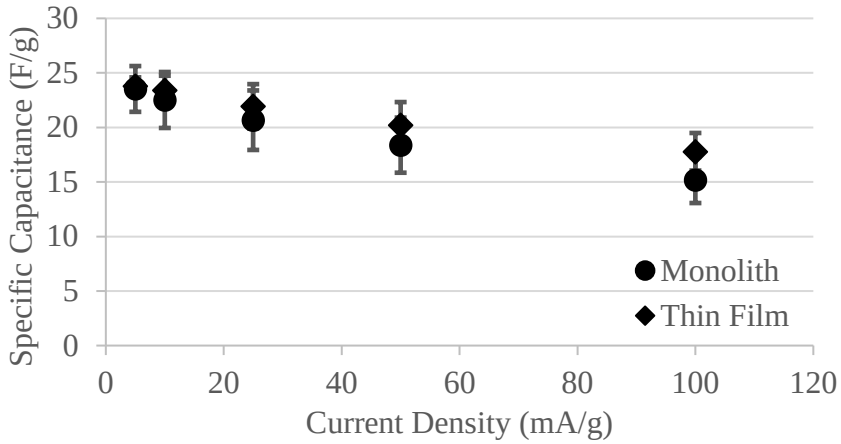

Figure 5.5 Specific capacitance versus current density for in-house pyrolyzed pine at 1000°C

There are two possible explanations for the capacitive performance difference between the 800°C and 1000°C biochar electrodes. The first is that the low concentration of polar surface oxygen groups in the 1000°C biochar results in a more hydrophobic surface, and therefore inadequate pore filling of the biochar [13], [32]. CHN results determine that the 1000°C samples contain only 1-3 wt. % oxygen, while XPS results of the C1s spectra show that graphitic carbon makes up ~90% of the biochar carbon surface chemistry (8.5 Appendix E). Inadequate pore filling with electrolyte would result in a loss of active surfaces for EDLC energy storage.

The second explanation is that some of the surfaces within the 1000°C electrodes may have limited ion accessibility due to their small pore mouth sizes. The high CO_2 measured SSA values suggest a smaller average pore diameter compared to the 800°C biochar. It has been found that the trend between SSA and specific capacitance is not linear, as small pores which contribute substantial surface areas may be inaccessible to the electrolyte [60]. To an extent, desolvation and distortion of ion shells has been found to occur with higher voltages, resulting in ions squeezing into the small pores [26]. However, the lower limit of pore size is not known.

Several authors have proposed that extended heat treatment of carbon can cause the pores to collapse and sinter [28], [60], [96]. Due to the slow pyrolysis temperature ramp rate required to achieve crack-free biochar, there is more than a 10-hour difference in heat treatment time between the 800°C and 1000°C samples (Table I). In her thesis, Zuliani found that pore collapse started to

occur during heat treatment processes where 950°C was held for more than 3 hours [96]. Distinguishing the leading cause of the reduced capacitive performance between either pore size distribution, surface wettability, or pore collapse is very difficult due to the heterogeneous nature of the carbon materials and the inability to decouple properties of carbons, which are ultimately a result of the production process [30]. It could be one or a combination of these pore accessibility concerns.

The Ohmic resistances of the 1000°C electrodes are included in Table XVI. These values are in the same range as the 800°C electrodes, supporting the claim that iR drop is largely due to contact resistance between the current collector and carbon electrode.

Table XVI. Ohmic resistance data for 1000°C electrodes

Electrode	ΔV (V)	R_{DROP} = ΔV/2I (Ω)
Maple 1000°C Monolith	0.027	2.90
Maple 1000°C Thin Film	0.014	3.45
Pine 1000°C Monolith	0.017	2.94
Pine 1000°C Thin Film	0.021	6.11

Electrochemical Impedance Spectroscopy was conducted on the 1000°C pyrolyzed electrodes. However, the modified Suss et al. equivalent circuit model had difficulties fitting their responses. The problem largely arose in the low frequency regime due to a significant deviation from the -90° phase angle representative of ideal capacitance behavior. Figure 5.6 shows the Nyquist plots of the 800°C and 1000°C maple monolithic electrodes. As a generalized ideal response for supercapacitors, when frequencies get low (< 1 Hz), the real impedance, Z', or real resistive component, stays constant while the imaginary impedance, -Z", increases (in the negative direction). This results in a phase angle that approaches -90° and a more vertical response in the Nyquist plot with decreasing frequency. The further away from vertical the response strays, the worse the rate capability of the capacitive device and the higher the device resistance. In the high frequency response, the semi-circle is much smaller for the 1000°C electrode, due to the higher intrinsic conductivity of the carbon.

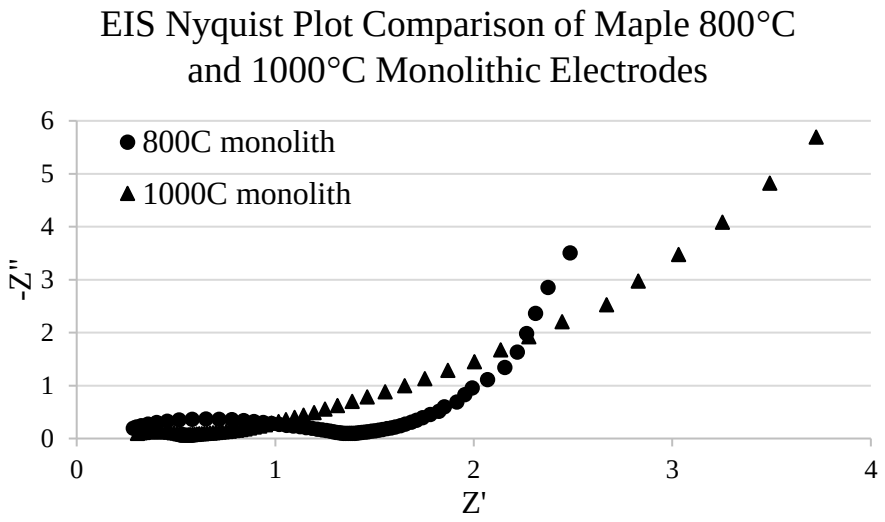

Figure 5.6. EIS Nyquist response of maple 800°C and 1000°C monolithic electrodes

The real resistance, Z', is plotted against frequency for the maple 800°C and 1000°C electrodes in Figure 5.7 to investigate the deviation from ideal EDLC behavior. At high frequencies, the 1000°C electrode has lower resistance, due to the higher conductivity of the carbon. As frequency gets lower, a more dramatic increase in the resistance is seen for the 1000°C electrode. This is indicative of resistances hindering the capacitive processes within the electrode. As a result, the assumption of the equivalent circuit model that all pores are readily accessible to the electrolyte is not upheld by the 1000°C electrode, and fails to adequately model the EIS response. The same behavior was observed for the thin film electrode structures, as well as the pine biochar.

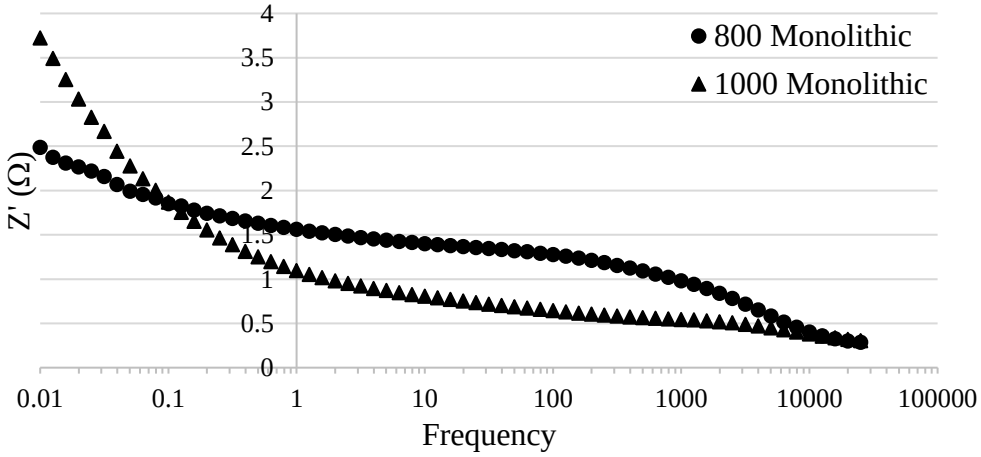

Figure 5.7. Z' versus frequency for the 800°C and 1000°C maple monolith electrodes

While pore accessibility is believed to be the cause of the low frequency resistances, it is not possible to distinguish whether wettability of the material or size of the pores plays a more important role. Ultimately, the 800°C pyrolyzed electrodes outperformed those pyrolyzed at 1000°C.

5.3.4 Rate Capability Modeling and Relationships to Ion Diffusion Processes

A new modeling approach was applied to the GC rate capability data to quantify the ease of ion diffusion to carbon surfaces for the different types of electrodes. In this analysis, specific capacitances for different current densities were converted into specific surface area normalized capacitances; the F/g value for an electrode type was divided by the sum of its N_2 BET and CO_2 SSA values (in m^2/g), resulting in a F/m^2 value. This was plotted on the y-axis, with current density on the x-axis. The resulting data was fitted by Equation 4:

$$y = a\ lnx + b$$

Equation 4. Generalized model for the SSA normalized capacitance rate capability

In this equation, b is the theoretical maximum SSA normalized capacitance for an electrode as the current density approaches zero. This value represents how efficient the carbon surfaces are at forming an EDLC. Parameter a, which is always negative, models the degradation of capacitive performance with current density. The larger the magnitude of a, the worse the rate performance of the electrode. When the same electrolyte is used, parameter a is related to the accessibility of the electrode pore surfaces to ions during charge/discharge mass transport processes. If some of the pores measured by gas adsorption are completely inaccessible to the electrolyte, the value of b will be smaller. If pores are harder to access, due to wettability or pore size constraints for example, then the magnitude of a will be larger. An example of the fitted SSA normalized capacitance data for the 800°C pine electrodes is illustrated in Figure 5.8. The plots for the rest of the electrodes tested are included in 8.7 Appendix G.

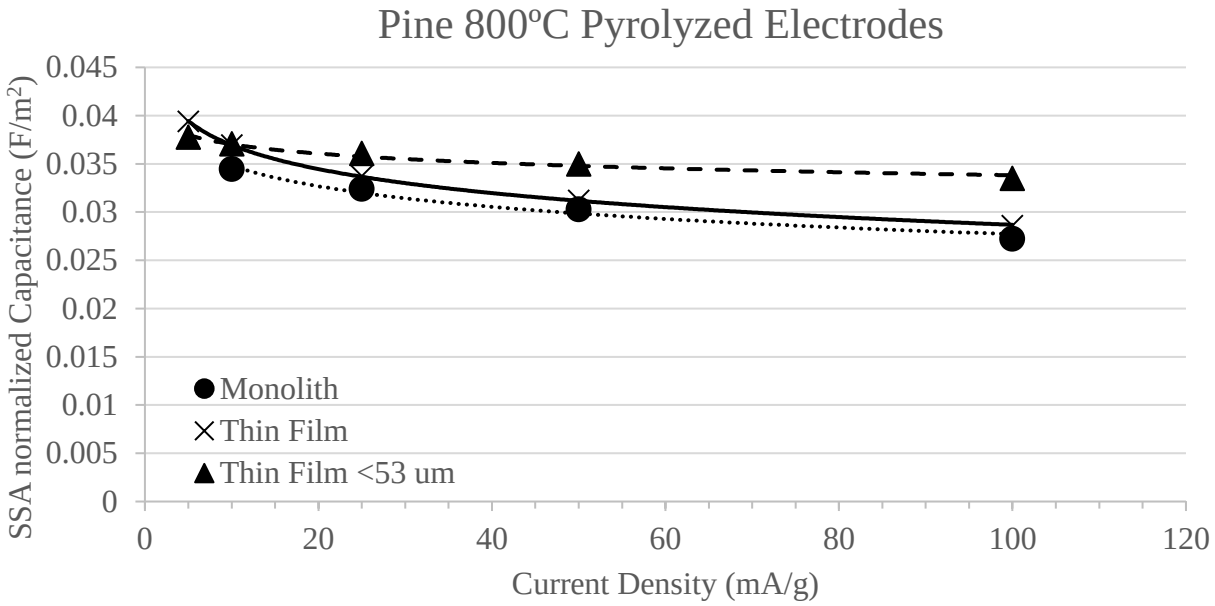

Figure 5.8. Fitted SSA normalized capacitance versus current density data for 800°C pyrolyzed pine electrodes

In addition to the in-house pyrolyzed biochar electrodes already mentioned in this thesis, this process was also carried out for 800°C maple thin film and monolithic electrodes electrochemically tested in 0.4 M KOH to investigate dilute electrolyte response, as well as 800°C maple and pine thin film electrodes with particle sizes of less than 53 μm, to test powdered biochar that retains less of the macrostructural elements and has higher electrode bulk density. A summary of the parameter values for the different types of electrodes, as well as the R-squared value for the fit are shown in Table XVII.

Table XVII. Summary of diffusion process fitted parameter values for the different electrodes

Electrode Type	a	b	R^2 of fit
Maple 800°C Monolith	-0.0037	0.0511	0.9995
Maple 800°C Thin Film	-0.0041	0.0517	0.9962
Maple 800°C Thin Film <53 μm	-0.0024	0.0458	0.9914
Maple 1000°C Monolith	-0.0036	0.0353	0.9762
Maple 1000°C Thin Film	-0.0029	0.0391	0.9902
Pine 800°C Monolith	-0.0031	0.0419	0.9747
Pine 800°C Thin Film	-0.0036	0.0452	0.9998
Pine 800°C Thin Film <53 μm	-0.0014	0.0402	0.9725
Pine 1000°C Monolith	-0.0034	0.0360	0.9525
Pine 1000°C Thin Film	-0.0025	0.0348	0.9329
Maple 800°C Monolith, 0.4M KOH	-0.0023	0.0343	0.9828
Maple 800°C Thin Film, 0.4M KOH	-0.0012	0.0336	0.9924

Some interesting trends are seen from the Table XVII data. While the a parameter values are similar for the 800°C pyrolyzed monolithic and thin film electrode structures of both maple and pine wood, the value for the thin films with particles < 53 μm has distinctly lower magnitudes. This indicates better rate capability and therefore pore accessibility in electrodes with smaller particle sizes. With smaller particle sizes, there will be smaller but more plentiful inter-particle void spaces, and a greater decentralization of the electrolyte reservoirs throughout the electrode. Clearly, the scale of diffusion lengths during charge/discharge ion mass transfer processes are much smaller than the size scale of the biochar macrostructural elements. Perhaps unexpected however is the slightly smaller b parameter values for the thin films with particles < 53 μm. Some of the small inter-particle void spaces may not contain enough electrolyte to supply the adjacent surfaces to form complete EDLs.

As expected based on the GC derived specific capacitance results, the b parameter values of the 1000°C electrodes are smaller than their 800°C counterparts. The a parameters of these electrodes are similar to the 800°C biochar.

The 800°C pyrolyzed electrodes tested with dilute electrolyte had the lowest magnitude a parameters, but also much lower b parameter values compared to the 4M test cells. During the discharge process, adsorbed ions will move away from the electrode surface, through the pore network and past counter-ions moving in the opposite direction towards the electrode surface. With a more dilute electrolyte, one could expect a lower flux of counter-ions moving against the discharged ions, facilitating the mass transport process; essentially, the analogy would be less cars on a two-way street. The b parameters are significantly smaller for dilute electrolyte, indicating worse EDLC formation efficiency despite better mass transport. When a more dilute electrolyte is used, the thickness of the Stern layer increases [97]. This results in a larger separation distance between the electrode surface and the adsorbed ion, decreasing the capacitance [98]. Dilute electrolyte ions are also likely to have higher coordination numbers and more adjacent water molecules interfering with the EDL formation at the electrode surface.

The R-squared values are very close to the ideal value of 1 for all electrodes analyzed, demonstrating the strong agreement of the model fit to the data.

EIS analysis was performed on the 800°C pyrolyzed maple thin film electrode cell with particles < 53 μm. The raw response and fitted Nyquist plot are shown in Figure 5.9, while fitting parameters from the modified Suss et al. equivalent circuit model are displayed in Table XVIII. Values are similar to the 800°C maple thin film results from Chapter 4. Kramers-Kronig analysis of error residuals can be found in 8.8 Appendix H.

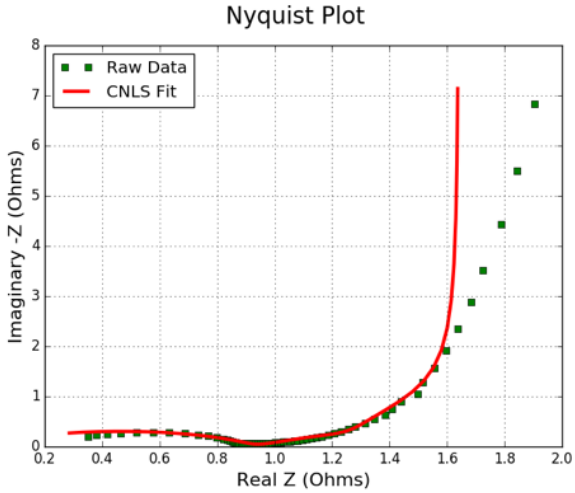

Figure 5.9. EIS Nyquist response and fit of maple thin film < 53 μm particle size electrode

Table XVIII. Parameter values for the fitted Nyquist data

Parameter	Maple Thin Film < 53 μm particle size
R_T (Ω*cm)	35.3
C_T (F/g)	48.4
R_S (Ω/BET m^2)	1.5
C_S (F/g)	30.8
Electrode Capacitance (F/g)	79.2
Device Capacitance (F/g)	19.8
Fit Root Mean Squared Error	0.04

A plot of the real impedance, Z', versus frequency is also shown for the 800°C pyrolyzed maple thin film electrode cell with particles < 53 μm (Figure 5.10). In comparing the 0.01 Hz value of Z' against those of the 800°C and 1000°C maple monolith electrodes from Figure 5.7, it is observed that the small particle thin film electrode has lower resistances in the capacitive frequency regime. These results support the work of the diffusion fitting analysis, in that a smaller value of parameter a is associated with less resistances for micropore accessibility.

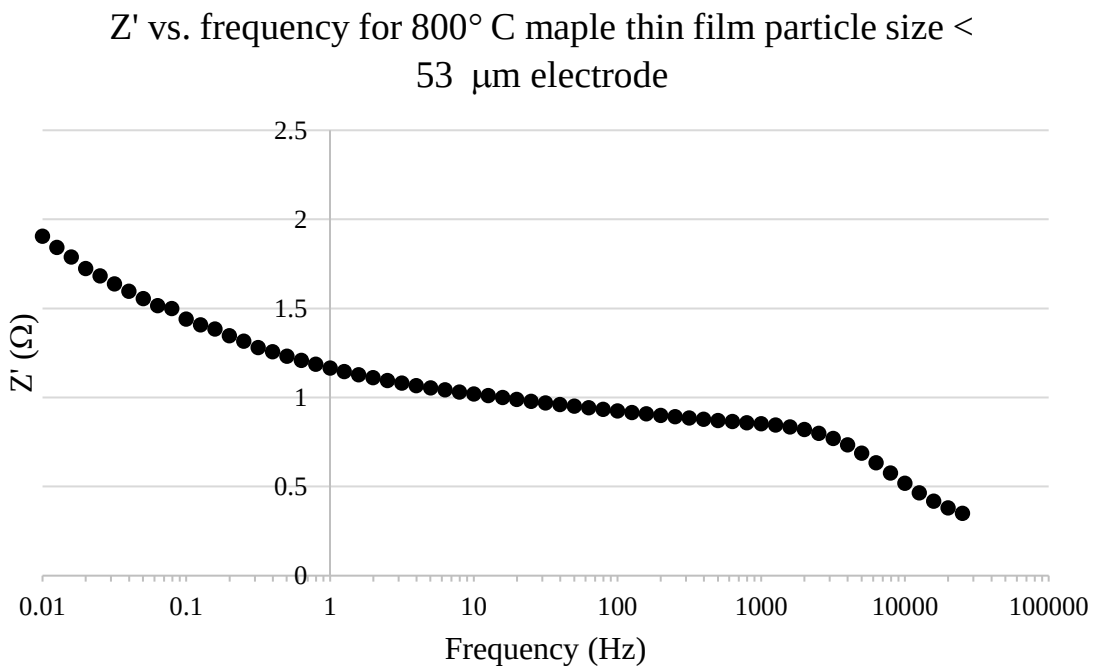

Figure 5.10. Z' versus frequency for the 800°maple thin film cell with particles < 53 μm

5.4 Conclusion

In this chapter, it was shown that biochar pyrolyzed at 1000°C had lower capacitive energy storage performance compared to biochar pyrolyzed at 800°C, despite improvements to the material's conductivity and total specific surface area. The elongated residence time and higher upper limit pyrolysis temperature remove oxygen surface groups from the biochar, which are instrumental to the wettability of the electrode and its affinity to be filled by aqueous electrolyte. Although capacitance tends to increase with increasing SSA, the high temperature pyrolysis process develops more sub-nanometer pores, which are not readily accessible to electrolyte ions. The conductivity differences between the 800°C and 1000°C pyrolyzed biochar appear negligible compared to that of the electrolyte filled pores when evaluating electrochemical capacitance.

For the same carbon material electrode, smaller particle sizes enable better rate capability performance and facilitate ion mass transport processes during charge/discharge cycling of supercapacitors. Although the current densities tested were relatively low, this effect is expected to be compounded at higher rates. As such, thin film supercapacitor electrodes with smaller particle sizes would be better suited to high power density applications.

Lastly, these results further demonstrate that the macrostructural elements of biochar are much too large to contribute to ion diffusion in supercapacitor electrodes. While they do not seem to hinder device performance, they do not appear to provide an advantage to mass transport over other carbon materials.

6. Conclusions and Recommendations for Future Work

6.1 Conclusions

Overall, the results shown in this thesis show potential for the application of monolithic biochar electrodes in supercapacitor devices. While performance is currently quite low, the lack of research conducted in this area means that there is likely significant room for improvement.

SEM electron beam deceleration proved to be a valuable technique to resolve mesoporous features of biochar, and bridge the gap between current SEM images with TEM analysis. Being able to achieve such high magnifications with an SEM device is important not only because of the high-resolution images produced, but also because the device's lower magnification range can supply complementary information such as the pore orientation and where the pore exists within the macrostructure. Furthermore, observing the mesoporosity permits validation of DFT isotherm models used to fit N_2 physisorption results. With continued developments in the field of microscopy, opportunities to clearly see sub-nanometer pores will eventually clear up ongoing confusion with the EDL formation mechanism.

In Chapter 4, monolithic biochar electrodes constructed up to 5 millimetres thick achieved the same specific capacitance performance as a 300 μm thick powdered thin film of the same material, while also having a larger mass and therefore larger total energy storage capacity. This finding demonstrates promise for the construction of electrodes many times larger than those currently applied, hopefully improving the current low standard of energy density in supercapacitors.

Chapter 4 also showed a clear, direct relationship between electrode bulk density and device volumetric capacitance performance (and therefore energy density). As such, thin film electrodes will continually be superior for high volumetric capacitance performance. Furthermore, it was demonstrated in both Chapters 4 and 5 that the internal structures retained in monolithic biochar are too large to facilitate ion mass transport processes during electrochemical charge and discharge cycles. From the information obtained, an idealized monolithic biochar structure can begin to be conceptualized for spatially unrestricted applications. This structure would look similar to the highly uniform pine wood biochar shown in Figure 4.2, except with much smaller tracheid

diameters and wall thickness. The diameter of the tracheids would be no greater than 1 μm, while the lengths of these tracheids would be as long as possible. If the monolithic biochar remained unactivated, the tracheid walls should be thin with a rough texture to maximize SSA. If the monolith was going to undergo an activation process, the walls should likely be thicker in order to withstand the process and maintain the monolithic structure. Biomass or synthetic alternatives that demonstrate these features should be investigated for supercapacitor application.

In Chapter 5, it was determined that while biochar pyrolyzed at 1000°C has higher carbon content, conductivity, and specific surface area, it's smaller average pore diameter and lack of surface oxygen groups are not conducive to efficient EDL formation on the carbon electrode surfaces. Wettability of the carbon surfaces in aqueous electrolyte appears to play a more significant role in device performance than previously thought.

Monolithic woody biochar has a very unique structure and is an exciting, carbon-neutral material. While it's heterogeneity and hard-to-isolate properties make it difficult to scientifically explore, it has a lot of potential for improvement and will eventually end up in various applications.

6.2 Future Work

In order for biochar supercapacitor electrodes to be competitive the performance has to improve. Future research efforts should be put towards investigating biochar activation methods, either for the exfoliation and increased specific surface area of carbon structures, or the creation of surface groups that can provide significant pseudocapacitive contributions to the cell. Although work of this nature has achieved promising results for biochar powdered thin film electrodes, activation of monolithic biochar while retaining the structure will present unique complications [5], [7], [8]. Preliminary work was conducted in this area, and is detailed in 8.9 Appendix I. KOH thermally activated monolithic biochar electrodes showed a ~15% increase in specific capacitance due to a more highly developed microporous specific surface area. It is believed that this increase can be substantially improved by optimizing the activation process. Other opportunities for carbon surface doping with oxygen groups as well as heavy metals for pseudocapacitive energy storage exist.

In Chapter 4, no effect of increasing electrode dimensionality was seen on the specific capacitive performance. It is hypothesized that there is a limit and so thicker electrodes should be explored, as well as more aggressive current densities that truly take advantage of what makes supercapacitors so attractive. Multi-cell devices with thicker electrodes in series should be evaluated against their thin film counterparts in the future. It is expected that the thicker electrode cells will have a larger total capacity based on how capacitances mathematically combine in series.

Finally, academic research of supercapacitors does not readily translate into real world solutions, and more effort needs to be put forth into "application relevant" empirical studies. If this fails to occur, the research will always seem interesting but will lack applicability. Demonstrations of what supercapacitors can achieve or building the devices to solve a specific energy storage problem will support their growth and development.

7. References

[1] C. Soc, G. Wang, and J. Zhang, "A review of electrode materials for electrochemical supercapacitors," *Chem. Soc. Rev.*, vol. 41, pp. 797–828, 2012.

[2] F. Béguin, V. Presser, A. Balducci, and E. Frackowiak, "Carbons and electrolytes for advanced supercapacitors," *Adv. Mater.*, vol. 26, no. 14, pp. 2219–2251, 2014.

[3] J. Chmiola, G. Yushin, Y. Gogotsi, C. Portet, and P. L. Taberna, "Anomalous Increase in Carbon Capacitance at Pore Sizes Less Than 1 Nanometer," *Science (80-.).*, vol. 7, no. 2002, pp. 1760–1763, 2005.

[4] K. Qian, A. Kumar, H. Zhang, D. Bellmer, and R. Huhnke, "Recent advances in utilization of biochar," *Renew. Sustain. Energy Rev.*, vol. 42, pp. 1055–1064, 2015.

[5] J. Jiang *et al.*, "Highly ordered macroporous woody biochar with ultra-high carbon content as supercapacitor electrodes," *Electrochim. Acta*, vol. 113, pp. 481–489, 2013.

[6] C. H. Chia, A. Downie, and P. Munroe, "Characteristics of biochar: physical and structural properties," in *Biochar for Environmental Management: Science and Technology*, J. Lehmann and S. Joseph, Eds. Routledge, 2009, pp. 63–88.

[7] A. M. Dehkhoda, E. Gyenge, and N. Ellis, "A novel method to tailor the porous structure of KOH-activated biochar and its application in capacitive deionization and energy storage," *Biomass and Bioenergy*, vol. 87, pp. 107–121, 2016.

[8] M. Genovese, J. Jiang, K. Lian, and N. Holm, "High capacitive performance of exfoliated biochar nanosheets from biomass waste corn cob," *J. Mater. Chem. A*, vol. 3, no. 6, pp. 2903–2913, 2015.

[9] R. Burt, G. Birkett, and X. S. Zhao, "A review of molecular modelling of electric double layer capacitors," *R. Soc. Chem.*, vol. 16, pp. 6519–6538, 2014.

[10] Q. Wang, "Carbon materials for high volumetric performance supercapacitors: design, progress, challenges and opportunities," *Energy Environ. Sci.*, vol. 9, pp. 729–762, 2016.

[11] O. Barbieri, M. Hahn, A. Herzog, and R. Kötz, "Capacitance limits of high surface area activated carbons for double layer capacitors," *Carbon N. Y.*, vol. 43, no. 6, pp. 1303–1310, 2005.

[12] B. E. E. Conway, V. Birss, and J. Wojtowicz, "The role and utilization of pseudocapacitance for energy storage by supercapacitors," *J. Power Sources*, vol. 66, no. 1–2, pp. 1–14, 1997.

[13] M. Seredych, M. Koscinski, M. Sliwinska-bartkowiak, and T. J. Bandosz, "Active pore space utilization in nanoporous carbon-based supercapacitors: Effects of conductivity and pore accessibility," *J. Power Sources*, vol. 220, pp. 243–252, 2012.

[14] K. Fic, M. Meller, and E. Frackowiak, "Interfacial Redox Phenomena for Enhanced Aqueous Supercapacitors," *J. Electrochem. Soc.*, vol. 162, no. 5, pp. 5140–5147, 2015.

[15] A. Ghosh and Y. Hee, "Carbon-Based Electrochemical Capacitors," *ChemSusChem*, vol. 5, pp. 480–499, 2012.

[16] Y. Oh *et al.*, "Oxygen functional groups and electrochemical capacitive behavior of incompletely reduced graphene oxides as a thin-film electrode of supercapacitor," *Electrochim. Acta*, vol. 116, pp. 118–128, 2014.

[17] Y. Fang *et al.*, "Renewing Functionalized Graphene as Electrodes for High-Performance Supercapacitors," *Adv. Mater.*, vol. 24, pp. 6348–6355, 2012.

[18] G. Salitra, A. Soffer, L. Eliad, Y. Cohen, and D. Aurbach, "Carbon Electrodes for Double-Layer Capacitors I. Relations Between Ion and Pore Dimensions," *J. Electrochem. Soc.*,

vol. 147, no. 7, pp. 2486–2493, 2000.
[19] J. Chmiola, G. Yushin, R. Dash, and Y. Gogotsi, "Effect of pore size and surface area of carbide derived carbons on specific capacitance," *J. Power Sources*, vol. 158, pp. 765–772, 2006.
[20] C. Vix-guterl, E. Frackowiak, K. Jurewicz, M. Friebe, J. Parmentier, and F. Béguin, "Electrochemical energy storage in ordered porous carbon materials," *Carbon N. Y.*, vol. 43, pp. 1293–1302, 2005.
[21] C. Merlet *et al.*, "On the molecular origin of supercapacitance in nanoporous carbon electrodes," *Nat. Mater.*, vol. 11, 2012.
[22] T. Ohkubo, T. Konishi, Y. Hattori, H. Kanoh, and T. Fujikawa, "Restricted Hydration Structures of Rb and Br Ions Confined in Slit-Shaped Carbon Nanospace," *J. Am. Chem. Soc.*, vol. 124, pp. 11860–11861, 2002.
[23] M. Eikerling, A. A. Kornyshev, and E. Lust, "Optimized Structure of Nanoporous Carbon-Based Double-Layer Capacitors," *J. Electrochem. Soc.*, vol. 152, no. 1, pp. E24–E33, 2005.
[24] L. Eliad, G. Salitra, A. Soffer, and D. Aurbach, "Ion Sieving Effects in the Electrical Double Layer of Porous Carbon Electrodes: Estimating Effective Ion Size in Electrolytic Solutions," *J. Phys. Chem.*, vol. 105, pp. 6880–6887, 2001.
[25] Y. Gogotsi, R. K. Dash, G. Yushin, T. Yildirim, G. Laudisio, and J. E. Fischer, "Tailoring of Nanoscale Porosity in Carbide-Derived Carbons for Hydrogen Storage," *J. Am. Chem. Soc.*, vol. 127, pp. 16006–16007, 2005.
[26] R. K. Kalluri *et al.*, "Unraveling the potential and pore-size dependent capacitance of slit-shaped graphitic carbon pores in aqueous electrolytes," *Phys. Chem. Chem. Phys.*, vol. 15, pp. 2309–2320, 2013.
[27] H. Yamada, H. Nakamura, F. Nakahara, and I. Moriguchi, "Electrochemical Study of High Electrochemical Double Layer Capacitance of Ordered Porous Carbons with Both Meso/Macropores and Micropores," *J. Phys. Chem.*, vol. 111, pp. 227–233, 2007.
[28] W. Xing *et al.*, "Hierarchical porous carbons with high performance for supercapacitor electrodes," *Carbon N. Y.*, vol. 47, no. 7, pp. 1715–1722, 2009.
[29] K. Xia, Q. Gao, J. Jiang, and J. Hu, "Hierarchical porous carbons with controlled micropores and mesopores for supercapacitor electrode materials," *Carbon N. Y.*, vol. 46, pp. 1718–1726, 2008.
[30] E. A. Müller and K. E. Gubbins, "Molecular simulation study of hydrophilic and hydrophobic behavior of activated carbon surfaces," *Carbon N. Y.*, vol. 36, no. 10, pp. 1433–1438, 1998.
[31] M. J. Bleda-Martinez, D. Lozano-Castello, E. Morallon, D. Cazorla-Amoros, and A. Linares-Solano, "Chemical and electrochemical characterization of porous carbon materials," *Carbon N. Y.*, vol. 44, pp. 2642–2651, 2006.
[32] A. G. Pandolfo and A. F. Hollenkamp, "Carbon properties and their role in supercapacitors," *J. Power Sources*, vol. 157, pp. 11–27, 2006.
[33] J. Bachmann, S. K. Woche, M. Goebel, M. B. Kirkham, and R. Horton, "Extended methodology for determining wetting properties of porous media," *Water Resour. Res.*, vol. 39, no. 12, pp. 1353–1367, 2003.
[34] W. J. Liu, H. Jiang, and H. Q. Yu, "Development of Biochar-Based Functional Materials: Toward a Sustainable Platform Carbon Material," *Chem. Rev.*, vol. 115, no. 22, pp. 12251–12285, 2015.

[35] L. J. Gibson, “The hierarchical structure and mechanics of plant materials,” *J. R. Soc. Interface*, vol. 9, pp. 2749–2766, 2012.
[36] J. Walker, *Primary wood processing: principles and practice*. Dordrecht, The Netherlands: Springer, 2006.
[37] S. Kloss *et al.*, “Characterization of Slow Pyrolysis Biochars: Effects of Feedstocks and Pyrolysis Temperature on Biochar Properties,” *J. Env. Qual.*, vol. 41, pp. 990–1000, 2012.
[38] S. Zhou, B. Pecha, M. Van Kuppevelt, A. G. Mcdonald, and M. Garcia-perez, “Slow and fast pyrolysis of Douglas-fir lignin: Importance of liquid-intermediate formation on the distribution of products,” *Biomass and Bioenergy*, vol. 66, pp. 398–409, 2014.
[39] D. C. Nagle and C. E. Byrne, “Carbonized wood and materials formed therefrom,” 6124028, 2000.
[40] C. E. Byrne and D. C. Nagle, “Carbonized wood monoliths - characterization,” *Carbon N. Y.*, vol. 35, no. 2, pp. 267–273, 1997.
[41] R. K. Sharma, J. B. Wooten, V. L. Baliga, X. Lin, W. G. Chan, and M. R. Hajaligol, “Characterization of chars from pyrolysis of lignin,” *Fuel*, vol. 83, pp. 1469–1482, 2004.
[42] W. Mu, H. Ben, A. Ragauskas, and Y. Deng, “Lignin Pyrolysis Components and Upgrading — Technology Review,” *Bioenerg. Res.*, vol. 6, pp. 1183–1204, 2013.
[43] X. Zhou, W. Li, R. Mabon, and L. J. Broadbelt, “A Critical Review on Hemicellulose Pyrolysis,” *Energy Technol.*, vol. 5, pp. 52–79, 2017.
[44] X. Wang, W. Zhou, G. Liang, D. Song, and X. Zhang, “Characteristics of maize biochar with different pyrolysis temperatures and its effects on organic carbon, nitrogen and enzymatic activities after addition to fluvo-aquic soil,” *Sci. Total Environ.*, vol. 538, pp. 137–144, 2015.
[45] F. Ronsse, S. van Hecke, D. Dickinson, and W. Prins, “Production and characterization of slow pyrolysis biochar: Influence of feedstock type and pyrolysis conditions,” *GCB Bioenergy*, vol. 5, no. 2, pp. 104–115, 2013.
[46] X. Cao *et al.*, “Characterization of wood chars produced at different temperatures using advanced solid-state 13C NMR spectroscopic techniques,” *Energy & Fuels*, vol. 26, pp. 5983–5991, 2012.
[47] L. Zhang, J. Jiang, N. Holm, and F. Chen, “Mini-chunk biochar supercapacitors,” *J. Appl. Electrochem.*, vol. 44, no. 10, pp. 1145–1151, 2014.
[48] D. Rehrah, R. R. Bansode, O. Hassan, and M. Ahmedna, “Physico-chemical characterization of biochars from solid municipal waste for use in soil amendment,” *J. Anal. Appl. Pyrolysis*, vol. 118, pp. 42–53, 2016.
[49] D. Fu, Z. Chen, D. Xia, L. Shen, Y. Wang, and Q. Li, “A novel solid digestate-derived biochar-Cu NP composite activating H2O2 system for simultaneous adsorption and degradation of tetracycline,” *Environ. Pollut.*, vol. 221, pp. 301–310, 2017.
[50] H. Jin, X. Wang, Z. Gu, and J. Polin, “Carbon materials from high ash biochar for supercapacitor and improvement of capacitance with HNO3 surface oxidation,” *J. Power Sources*, vol. 236, pp. 285–292, 2013.
[51] X. He, T. Zhang, H. Ren, G. Li, L. Ding, and L. Pawlowski, “Phosphorus recovery from biogas slurry by ultrasound/H2O2 digestion coupled with HFO/biochar adsorption process,” *Waste Manag.*, vol. 60, pp. 219–229, 2016.
[52] R. Kumar, M. Dubey, P. Kharel, Z. Gu, and Q. Hua, “Biochar activated by oxygen plasma for supercapacitors,” *J. Power Sources*, vol. 274, pp. 1300–1305, 2015.
[53] D. Phifer, L. Tuma, T. Vystavel, P. Wandrol, and R. J. Young, “Improving SEM Imaging

Performance Using Beam Deceleration," *Micros. Today*, vol. 17, no. 4, pp. 40–49, 2009.
[54] J. C. Bouwer, T. J. Deerinck, E. Bushong, V. Astakhov, R. Ramachandra, and S. T. Peltier, "Deceleration of probe beam by stage bias potential improves resolution of serial block‐face scanning electron microscopic images," *Adv. Struct. Chem. Imaging*, vol. 2, no. 11, 2016.
[55] J. N. Caguiat, D. W. Kirk, and C. Q. Jia, "Uncertainties in characterization of nanoporous carbons using density functional theory-based gas physisorption," *Carbon N. Y.*, vol. 72, pp. 47–56, 2014.
[56] A. J. Pahnshin and C. de Zeeuw, *Textbook of Wood Technology*. McGraw-Hill, 1980.
[57] J. M. Dinwoodie, *Wood: Nature's Cellular, Polymeric Fibre-Composite*. Institute of Metals, University of Michigan, 1989.
[58] T. J. Hilbers *et al.*, "Lignin interactions during slow and fast pyrolysis," *J. Anal. Appl. Pyrolysis*, vol. 114, pp. 197–207, 2015.
[59] M. Chen *et al.*, "Preparation of activated carbon from cotton stalk and its application in supercapacitor," *J. Solid State Electrochem.*, vol. 17, pp. 1005–1012, 2013.
[60] M. Sevilla and R. Mokaya, "Energy storage applications of activated carbons: supercapacitors and hydrogen storage," *Energy Environ. Sci.*, vol. 7, pp. 1250–1280, 2014.
[61] X. Zhang, C. Peng, R. Wang, and J. Lang, "High-performance supercapacitors based on novel carbons derived from Sterculia lychnophora," *RSC Adv.*, vol. 5, pp. 32159–32167, 2015.
[62] G. Dobele, T. Dizhbite, M. V Gil, A. Volperts, and T. A. Centeno, "Production of nanoporous carbons from wood processing wastes and their use in supercapacitors and CO 2 capture," *Biomass and Bioenergy*, vol. 46, pp. 145–154, 2012.
[63] S. K. Ramasahayam, A. L. Clark, Z. Hicks, and T. Viswanathan, "Spent coffee grounds derived P, N co-doped C as electrocatalyst for supercapacitor applications," *Electrochim. Acta*, vol. 168, pp. 414–422, 2015.
[64] A. M. Dehkhoda and N. Ellis, "Electrosorption on activated biochar: effect of thermo-chemical activation treatment on the electric double layer capacitance," *J. Appl. Electrochem.*, vol. 44, pp. 141–157, 2014.
[65] A. Garcia-Gomez, P. Miles, T. A. Centeno, and J. M. Rojo, "Why Carbon Monoliths are Better Supercapacitor Electrodes than Compacted Pellets," *Electrochem. Solid-State Lett.*, vol. 13, no. 8, pp. 112–114, 2010.
[66] M. Liu, L. Kong, P. Zhang, Y. Luo, and L. Kang, "Porous wood carbon monolith for high-performance supercapacitors," *Electrochim. Acta*, vol. 60, pp. 443–448, 2012.
[67] B. Ridout, *Timber Decay in Buildings: The Conservation Approach to Treatment*. Taylor & Francis, 1999.
[68] E. Wheeler, "WPS 202: Wood Anatomy and Properties," *NCSU.edu*, 2015. [Online]. Available: http://www4.ncsu.edu/~xylem/WPS202/softwood/ray.htm. [Accessed: 04-Aug-2017].
[69] "Microscopic Structure of Wood," *Mendel University in Brno*. [Online]. Available: https://is.mendelu.cz/eknihovna/opory/zobraz_cast.pl?cast=19204. [Accessed: 04-Aug-2017].
[70] B. Choat, B. Choat, A. R. Cobb, and S. Jansen, "Structure and function of bordered pits : new discoveries and impacts on whole-plant hydraulic function," *New Phytol.*, vol. 177, pp. 608–626, 2008.

[71] Y. Lee, P. R. B. Eum, C. Ryu, Y. K. Park, J. H. Jung, and S. Hyun, “Characteristics of biochar produced from slow pyrolysis of Geodae-Uksae 1,” *Bioresour. Technol.*, vol. 130, pp. 345–350, 2013.
[72] K. Tsay, L. Zhang, and J. Zhang, “Effects of electrode layer composition/thickness and electrolyte concentration on both specific capacitance and energy density of supercapacitor,” *Electrochim. Acta*, vol. 60, pp. 428–436, 2012.
[73] Y. Yamada, T. Sasaki, N. Tatsuda, D. Weingarth, K. Yano, and R. Kötz, “A novel model electrode for investigating ion transport inside pores in an electrical double-layer capacitor: Monodispered microporous starburst carbon spheres,” *Electrochim. Acta*, vol. 81, pp. 138–148, 2012.
[74] S. Yoon, J. H. Jang, B. H. Ka, and S. M. Oh, “Complex capacitance analysis on rate capability of electric-double layer capacitor (EDLC) electrodes of different thickness,” *Electrochim. Acta*, vol. 50, pp. 2255–2262, 2005.
[75] A. P. Ranade, D. Y. Jung, B. G. Sammakia, T. Eilersten, and T. Davis, “Optimization Study of Supercapacitor Electrode Material Composition and Thickness for Enhanced Performance of the Supercapacitor,” *Clean Technol.*, vol. 20, pp. 171–174, 2011.
[76] C. Zhong *et al.*, *Electrolyte for Electrochemical Supercapacitors*. CRC Press, 2016.
[77] Y. Marcus, “Volumes of aqueous hydrogen and hydroxide ions at 0 to 200°C Volumes of aqueous hydrogen and hydroxide ions at 0 to 200°C,” *J. Chem. Phys.*, vol. 137, pp. 0–5, 2012.
[78] A. Laheäär, P. Przygocki, Q. Abbas, and F. Béguin, “Appropriate methods for evaluating the efficiency and capacitive behavior of different types of supercapacitors,” *Electrochem. commun.*, vol. 60, pp. 21–25, 2015.
[79] G. Xiong, C. Meng, R. G. Reifenberger, P. P. Irazoqui, and T. S. Fisher, “A Review of Graphene-Based Electrochemical Microsupercapacitors,” *Electroanalysis*, vol. 26, pp. 30–51, 2014.
[80] J. E. Zuliani, J. N. Caguiat, D. W. Kirk, and C. Q. Jia, “Considerations for consistent characterization of electrochemical double-layer capacitor performance,” *J. Power Sources*, vol. 290, pp. 136–143, 2015.
[81] M. E. Suss *et al.*, “Impedance-based study of capacitive porous carbon electrodes with hierarchical and bimodal porosity,” *J. Power Sources*, vol. 241, pp. 266–273, 2013.
[82] J. Bisquert and A. Compte, “Theory of the electrochemical impedance of anomalous diffusion,” *J. Electroanal. Chem.*, vol. 499, pp. 112–120, 2001.
[83] M. Gaberscek, J. Moskon, B. Erjavec, R. Dominko, and J. Jamnik, “The Importance of Interphase Contacts in Li Ion Electrodes: The Meaning of the High-Frequency Impedance Arc,” *Electrochem. Solid-State Lett.*, vol. 11, p. A170, 2008.
[84] J. P. Zheng, P. C. Goonetilleke, C. M. Pettit, and D. Roy, “Probing the electrochemical double layer of an ionic liquid using voltammetry and impedance spectroscopy: A comparative study of carbon nanotube and glassy carbon electrodes in [EMIM]+[EtSO4]-,” *Talanta*, vol. 81, pp. 1045–1055, 2010.
[85] C. Zhai, D. Hanaor, G. Proust, L. Brassart, and Y. Gan, “Interfacial electro-mechanical behaviour at rough surfaces,” *Extrem. Mech. Lett.*, vol. 9, pp. 422–429, 2016.
[86] G. Gourdin, A. Meehan, T. Jiang, P. Smith, and D. Qu, “Investigation of the impact of stacking pressure on a double-layer supercapacitor,” *J. Power Sources*, vol. 196, pp. 523–529, 2011.
[87] H. Wang and L. Pilon, “Intrinsic limitations of impedance measurements in determining

electric double layer capacitances," *Electrochim. Acta*, vol. 63, pp. 55–63, 2012.
[88] W. Suliman, J. B. Harsh, N. I. Abu-Lail, A. M. Fortuna, I. Dallmeyer, and M. Garcia-Perez, "Influence of feedstock source and pyrolysis temperature on biochar bulk and surface properties," *Biomass and Bioenergy*, vol. 84, pp. 37–48, 2016.
[89] J. M. Chem, M. Yang, Q. Yang, M. Wang, Y. Yang, and R. Schl, "Hierarchically aminated graphene honeycombs for electrochemical capacitive energy storage †‡," pp. 14076–14084, 2012.
[90] "Technical Note 201: Corrections for Potentiostat Response."
[91] R. Rodgers and W. Eggers, "Correction for Potentiostat Response in Impedance Measurements," in *Paper #228, 183rd Meeting of the Electrochemistry Society*, 1993.
[92] R. Rodgers, "Impedance Measurements with Real Potentiostats: Corrections for Potentiostat Response," in *Paper #134, 2nd International Symposium on Electrochemical Impedance Spectroscopy*, 1992.
[93] D. Qu and H. Shi, "Studies of the activated carbons used in double-layer supercapacitors," *J. Power Sources*, vol. 74, pp. 99–107, 1998.
[94] S. Fletcher, V. J. Black, and I. Kirkpatrick, "A universal equivalent circuit for carbon-based supercapacitors," *J. Solid State Electrochem.*, vol. 18, no. 5, pp. 1377–1387, 2014.
[95] S. Osswald and J. M. E. Bastian, "Oxidation and Purification of Carbon Nanostructures," in *Carbon Nanomaterials*, 2nd ed., Y. Gogotsi and V. Presser, Eds. CRC Press, 2013, pp. 355–394.
[96] J. E. Zuliani, "Effect of Activated Carbon Structure and Chemistry on the Performance of Electrochemical Double-Layer Capacitors," University of Toronto, 2017.
[97] M. A. Brown, A. Goel, and Z. Abbas, "Effect of Electrolyte Concentration on the Stern Layer Thickness at a Charged Interface," *Angew. Chemie - Int. Ed.*, vol. 55, pp. 3790–3794, 2016.
[98] B. E. Conway, *Electrochemical Supercapacitors: Scientific Fundamentals and Technological Applications*. Springer, 1999.
[99] J. E. Zuliani, D. W. Kirk, C. Q. Jia, and S. Tong, "Activated oil sands fluid coke for electrical double-layer capacitors," *J. Power Sources*, vol. 271, pp. 326–333, 2014.
[100] Y. J. Kim *et al.*, "Edge-Enriched, Porous Carbon-Based, High Energy Density Supercapacitors for Hybrid Electric Vehicles," *ChemSusChem*, vol. 5, pp. 535–541, 2012.
[101] F. Sun, J. Gao, X. Liu, X. Pi, Y. Yang, and S. Wu, "Porous carbon with a large surface area and an ultrahigh carbon purity via templating carbonization coupling with KOH activation as excellent supercapacitor electrode materials," *Appl. Surf. Sci.*, vol. 387, pp. 857–863, 2016.

8. Appendices

8.1 Appendix A: Python Script of EIS Equivalent Circuit Model Fitting Tool

```
#Useful References:

#fit uses the Levenberg-Marquardt algorithm
#help lmfit video: https://www.youtube.com/watch?v=PL3TdpZwKLQ
#help lmfit site: https://lmfit.github.io/lmfit-py/fitting.html
#statistical correlation meaning: https://explorable.com/statistical-correlation



import numpy as np
import matplotlib.pylab as plt
from lmfit import minimize, Parameters, report_fit
from scipy.stats import chisquare



#Before Running the program:

#Check model type
#Check data file import
#Check data file export
#Set L in units



#Data import

data = np.genfromtxt("data_file_name.txt", delimiter=',')
frequency = data[1:][:,1]
real = data[1:][:,2]
imag = data[1:][:,3]
totalZ = data[1:][:,4]
angle = data[1:][:,5]
w = frequency*2*np.pi


#Data export file
par_file = open("data_file_name_params.txt", "a")
```

```
#CNLS fitting:

params = Parameters()
params.add('R_esr_m', value = 0.18, min = 0.)
params.add('R_int_m', value = 0.2, min = 0.)
params.add('Q_int_m', value= 0.0001, min = 0.)
params.add('n_int_m', value= 0.65, min = 0., max = 1.)
params.add('R_t_m', value= 4.7, min = 0.)
params.add('C_t_m', value= 0.19, min = 0.)
params.add('R_s_m', value= 22.12, min = 0.)
params.add('C_s_m', value= 0.73, min = 0.)

#_t is the notation for a larger transport pore
#_s is the notation for a smaller storage pore


def get_residual(params, real, imag):

    R_esr_m = params['R_esr_m'].value
    R_int_m = params['R_int_m'].value
    Q_int_m = params['Q_int_m'].value

    n_int_m = params['n_int_m'].value
    R_t_m = params['R_t_m'].value
    C_t_m = params['C_t_m'].value
    R_s_m = params['R_s_m'].value
    C_s_m = params['C_s_m'].value


   Z_int_m = (1./R_int_m + Q_int_m*(1.j*w)**n_int_m)**-1.

   Z_s_m = (1-1.j)*(R_s_m/(2*w*C_s_m))**0.5*1./np.tanh((1+1.j)*(w*R_s_m*C_s_m/2)**0.5)

   Z_t_m = Z_s_m*1.j/(1.j-w*C_t_m*Z_s_m)

   Z_carbon_m = (R_t_m*Z_t_m)**0.5*1./np.tanh((R_t_m/Z_t_m)**0.5)

    model = R_esr_m + Z_int_m + Z_carbon_m

    model_Z = np.sqrt(np.real(model)**2 + np.imag(model)**2)

    resid = (real - np.real(model)) + (imag - np.imag(-model))

return resid
```

```
out = minimize(get_residual, params, args=(real, imag))

R_esr_m = out.params['R_esr_m'].value
R_int_m = out.params['R_int_m'].value
Q_int_m = out.params['Q_int_m'].value
n_int_m = out.params['n_int_m'].value
R_s_m = out.params['R_s_m'].value
C_s_m = out.params['C_s_m'].value
R_t_m = out.params['R_t_m'].value
C_t_m = out.params['C_t_m'].value


Z_int_m = (1./R_int_m + Q_int_m*(1.j*w)**n_int_m)**-1.

Z_s_m = (1-1.j)*(R_s_m/(2*w*C_s_m))**0.5*1./np.tanh((1+1.j)*(w*R_s_m*C_s_m/2)**0.5)

Z_t_m = Z_s_m*1.j/(1.j-w*C_t_m*Z_s_m)

Z_carbon_m = (R_t_m*Z_t_m)**0.5*1./np.tanh((R_t_m/Z_t_m)**0.5)

model = R_esr_m + Z_int_m + Z_carbon_m

model_phase_rad = np.arctan((np.imag(model))/(np.real(model)))
model_phase = model_phase_rad*180./np.pi


#RMSE of CNLS fit

Imped_fit = np.sqrt(np.real(model)**2 + np.imag(model)**2)
difference_fit = totalZ - Imped_fit                    #the DIFFERENCEs.
differences_fit = difference_fit[1:]
differences_squared_fit = differences_fit ** 2                  #the SQUAREs of ^
mean_of_differences_squared_fit = differences_squared_fit.mean()  #the MEAN of ^
rmse_val_fit = np.sqrt(mean_of_differences_squared_fit)          #ROOT of ^
print "CNLS fit RMSE = ", rmse_val_fit
print "Chi-squared of CNLS fit = ", out.chisqr


#Chi squared of manual fit

chi_sqr = sum(((np.real(Z) - real)**2)/real + ((np.imag(Z) + imag)**2)/(imag))
print "Chi-squared of manual fit =", chi_sqr

np.imag(chisquare(Z,Imped))

report_fit(out)
```

```
#Plotting

plt.figure(1)
plt.plot(real, imag, 'gs', label = 'Raw Data')
plt.suptitle('Nyquist Plot', fontsize='20')
plt.xlabel('Real Z (Ohms)', fontsize='16')
plt.ylabel('Imaginary -Z (Ohms)', fontsize='16')
plt.grid(True)
plt.plot(np.real(model), np.imag(-model), linestyle='-', linewidth ='3', color = 'r', label = 'CNLS
Fit')
plt.legend(loc = 'upper left')
plt.show()


plt.figure(2)
plt.subplot(2,1,1)
plt.plot(frequency, totalZ, 'gs', label = 'Raw Data')
plt.plot(frequency, np.abs(model), linestyle='-', linewidth ='2',color = 'r', label = 'CNLS Fit')
plt.xscale('log')
plt.yscale('log')
plt.legend(loc = 'lower left')
plt.suptitle('Bode Plot', fontsize='20')
plt.ylabel('Total Z (Ohms)', fontsize='16')
plt.subplot(2,1,2)
plt.plot(frequency, angle, 'gs', label = 'Raw Data')
plt.plot(frequency,-model_phase, linestyle='-', linewidth ='2',color = 'r', label = 'CNLS Fit')
plt.xscale('log')
plt.xlabel('Frequency (Hz)', fontsize='16')
plt.ylabel('-Phase Angle (deg)', fontsize='16')
plt.show()



# Send fitting parameters and rmse value to text file:

par_file.write('\n' + str(model_type) + ',' + str(R_esr) + ',' + str(R_int) + ',' + str(Q_int) + ',' +
str(n_int) + ',' + str(R_t) + ',' + str(C_t) + ',' + str(R_s) + ',' + str(C_s) +',' + str(rmse_val))
par_file.close()
```

8.2 Appendix B: N_2 Physisorption Isotherms

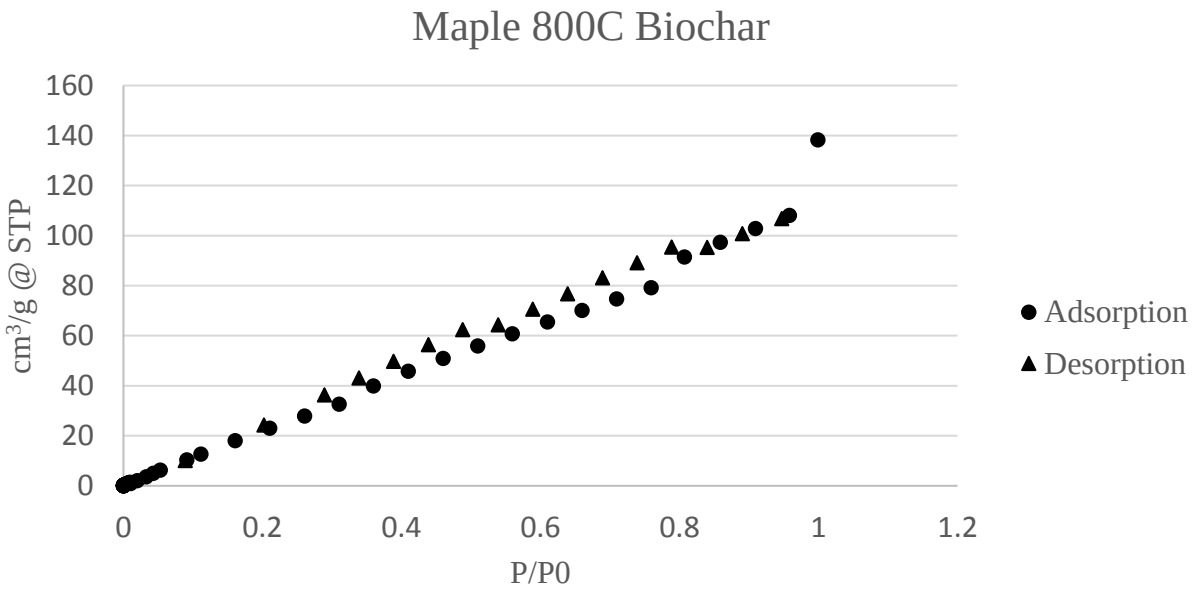

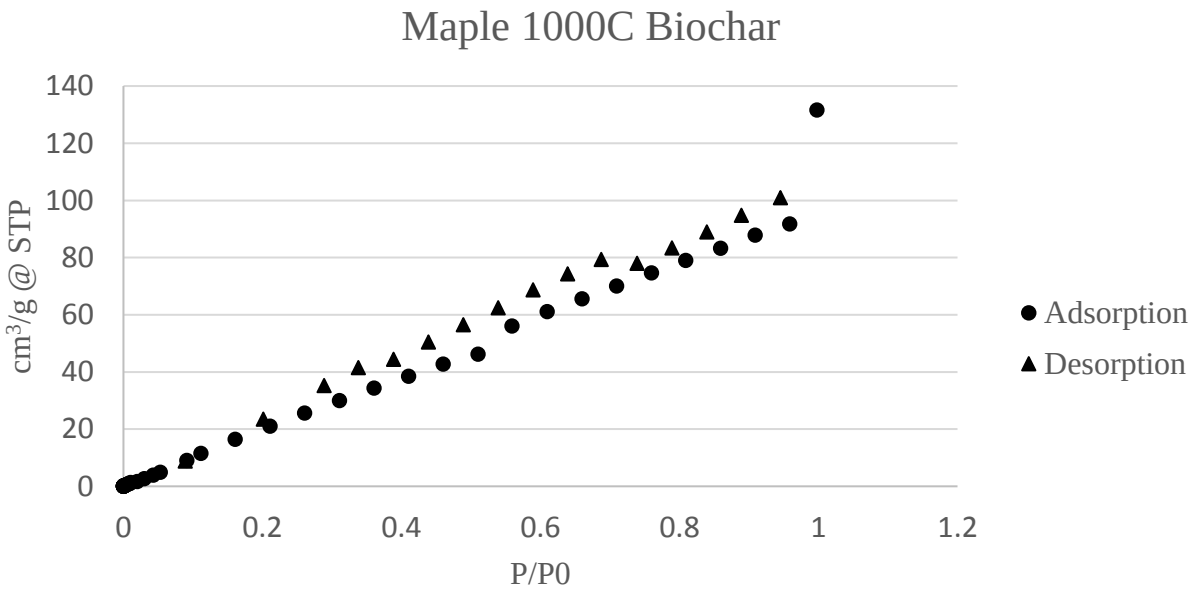

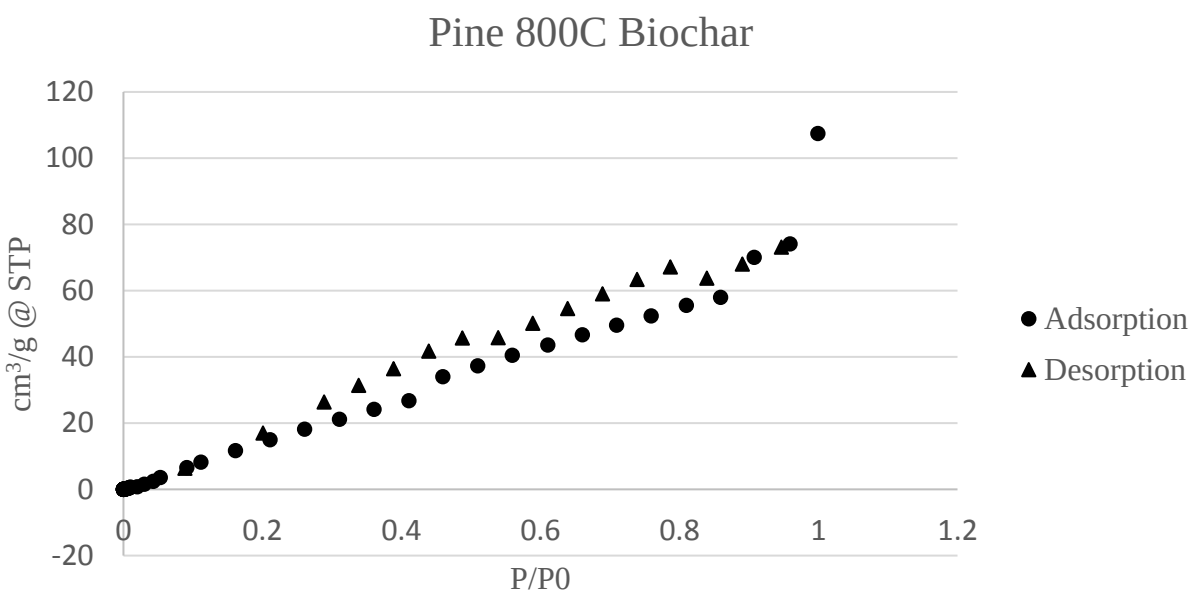
Pine 800C Biochar
120
100
80
60
40
20
0
-20
0
0.2
0.4
0.6
0.8
1
1.2
cm3/g @ STP
P/P0
Adsorption
Desorption

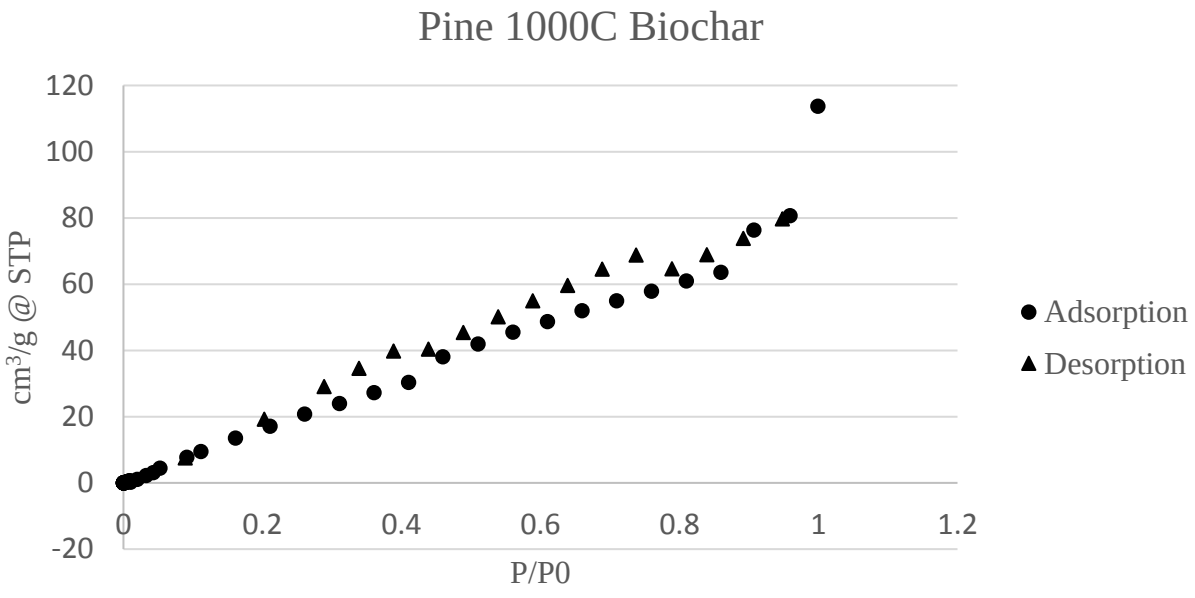
Pine 1000C Biochar
120
100
80
60
40
20
0
-20
0
0.2
0.4
0.6
0.8
1
1.2
cm3/g @ STP
P/P0
Adsorption
Desorption

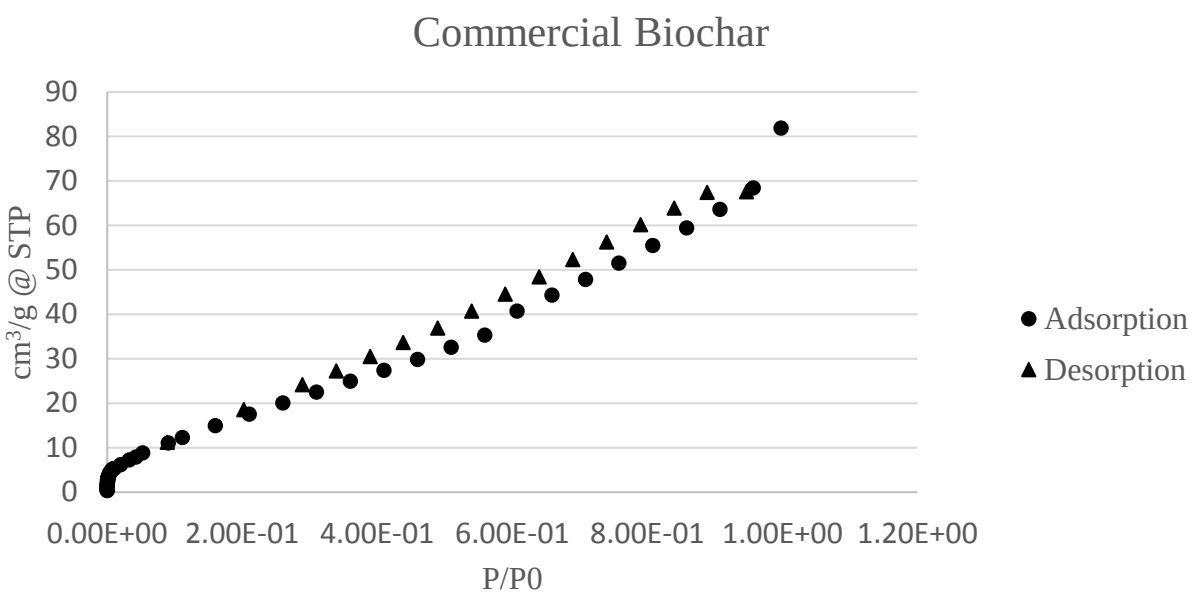
Commercial Biochar
90
80
70
60
50
40
30
20
10
0
cm3/g @ STP
0.00E+00
2.00E-01
4.00E-01
6.00E-01
8.00E-01
1.00E+00
1.20E+00
P/P0
Adsorption
Desorption

8.3 Appendix C: CO_2 Physisorption NLDFT Slit Pore Model Pore Size Distributions

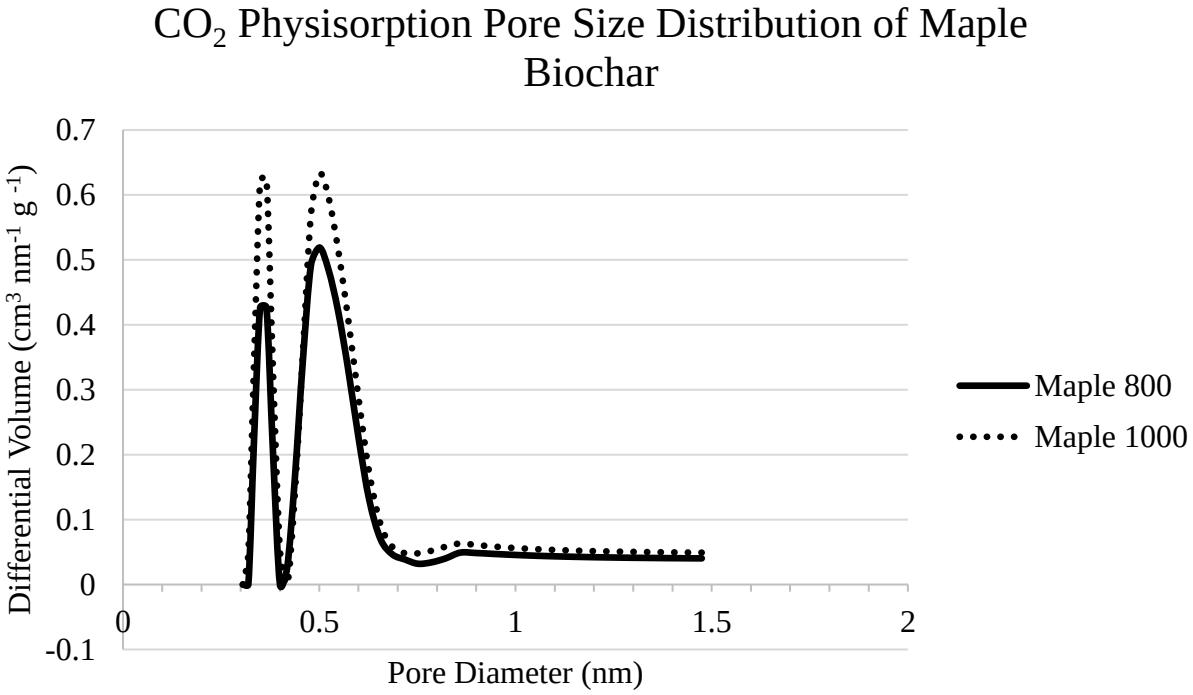

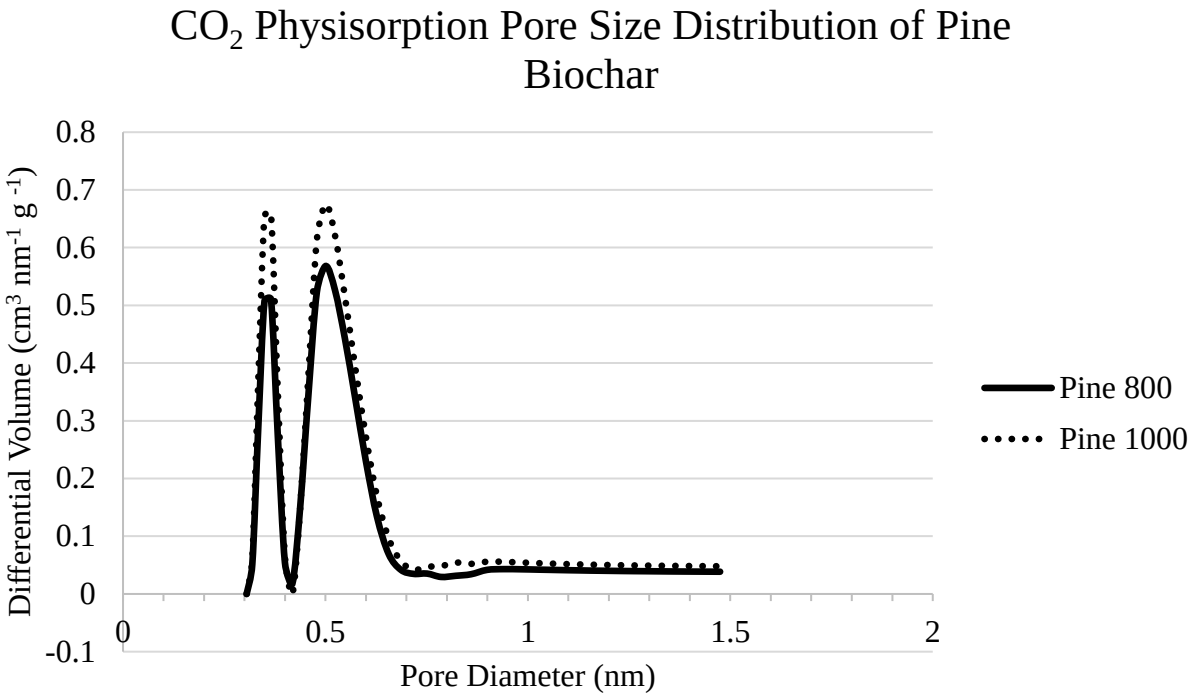
CO_2 Physisorption Pore Size Distribution of Pine Biochar
Differential Volume (cm^3 nm^{-1} g^{-1})
0.8
0.7
0.6
0.5
0.4
0.3
0.2
0.1
0
-0.1
0
0.5
1
1.5
2
Pore Diameter (nm)
Pine 800
Pine 1000

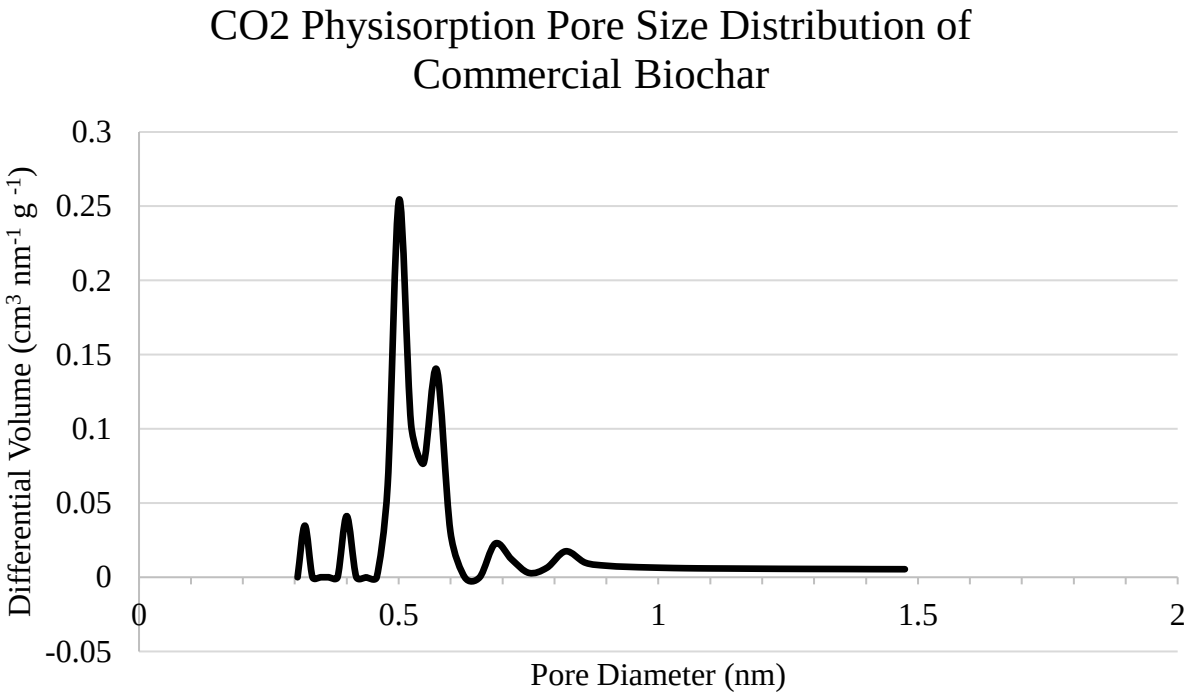
CO2 Physisorption Pore Size Distribution of Commercial Biochar
Differential Volume (cm^3 nm^{-1} g^{-1})
0.3
0.25
0.2
0.15
0.1
0.05
0
-0.05
0
0.5
1
1.5
2
Pore Diameter (nm)

8.4 Appendix D: Galvanostatic Cycling Voltage Versus Time Response Curve Examples

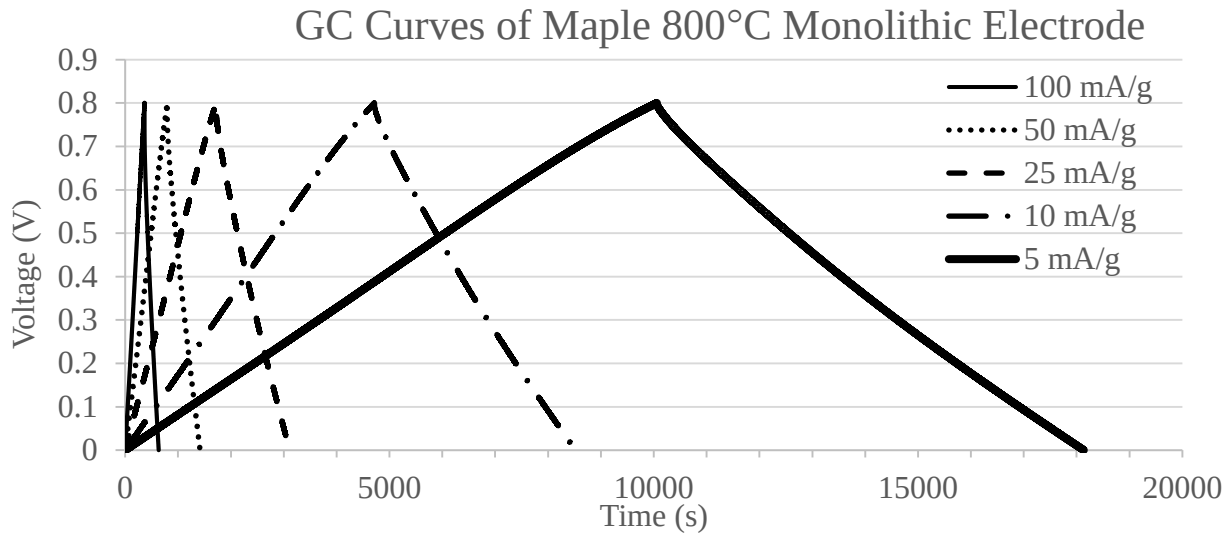

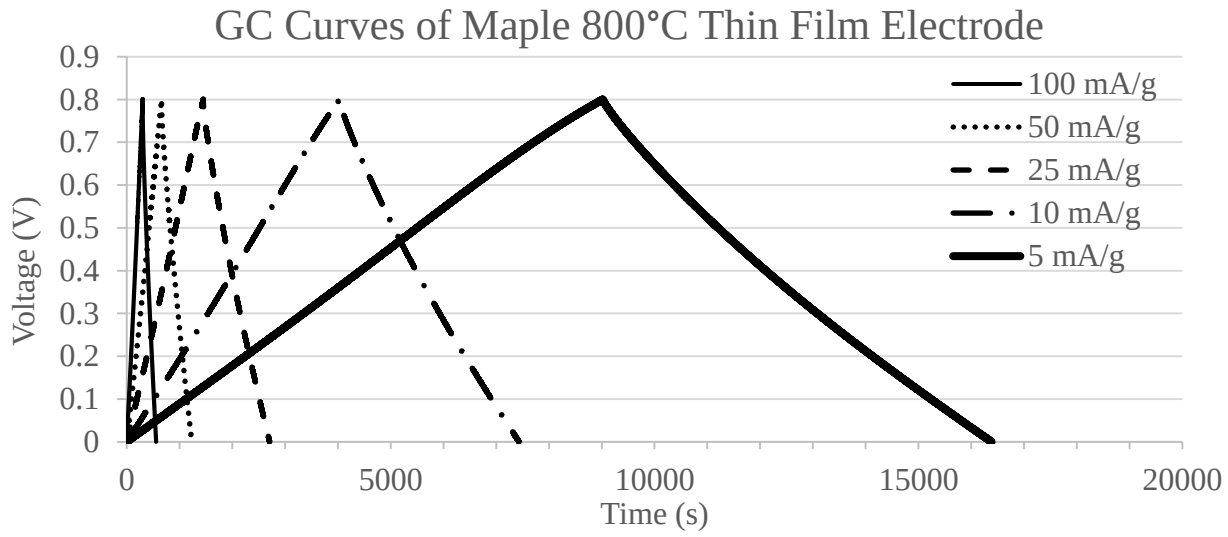

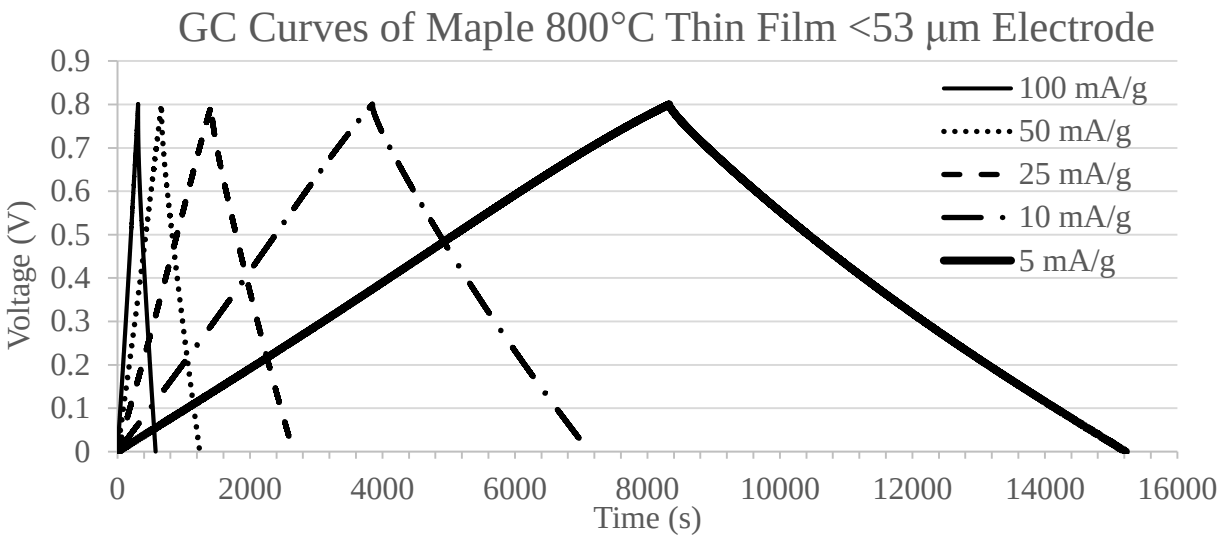
GC Curves of Maple 800°C Thin Film <53 μm Electrode
Voltage (V)
Time (s)
0
0.1
0.2
0.3
0.4
0.5
0.6
0.7
0.8
0.9
0
2000
4000
6000
8000
10000
12000
14000
16000
100 mA/g
50 mA/g
25 mA/g
10 mA/g
5 mA/g

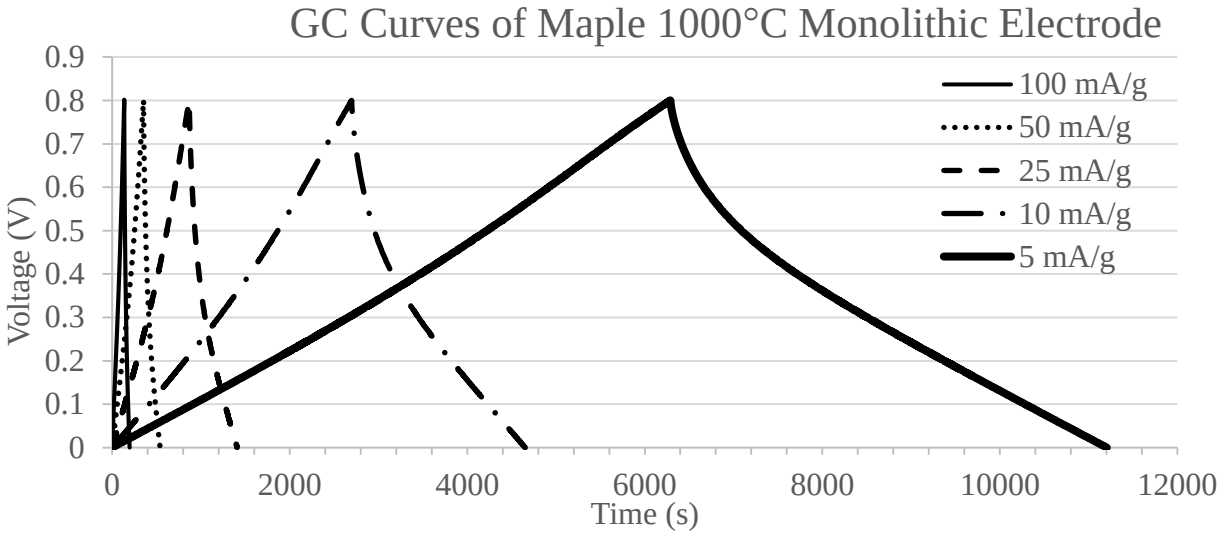
GC Curves of Maple 1000°C Monolithic Electrode
Voltage (V)
Time (s)
0
0.1
0.2
0.3
0.4
0.5
0.6
0.7
0.8
0.9
0
2000
4000
6000
8000
10000
12000
100 mA/g
50 mA/g
25 mA/g
10 mA/g
5 mA/g

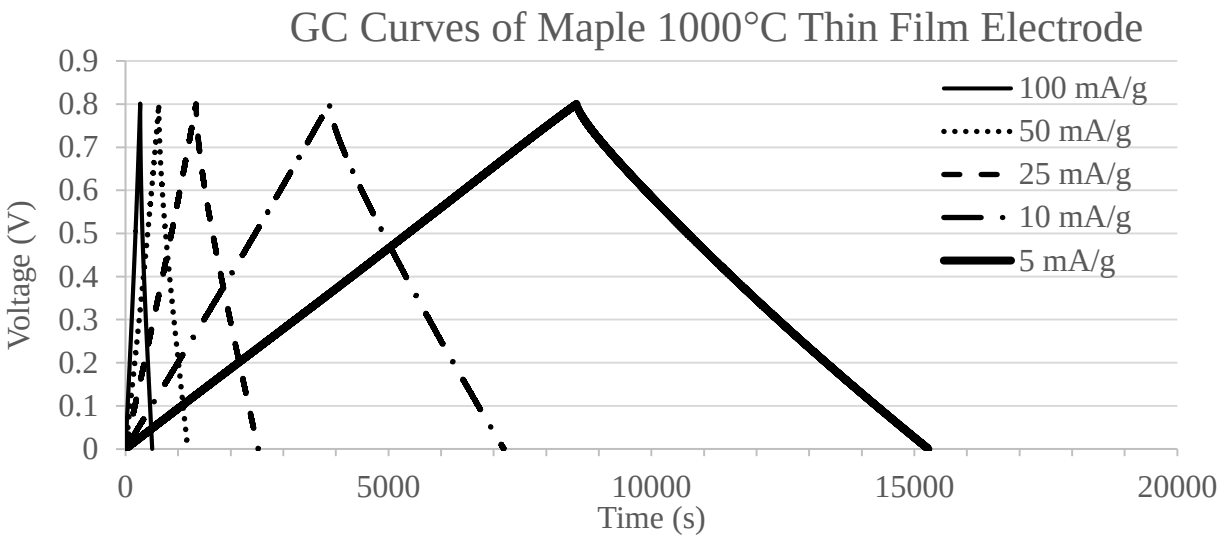
GC Curves of Maple 1000°C Thin Film Electrode
Voltage (V)
Time (s)
0
0.1
0.2
0.3
0.4
0.5
0.6
0.7
0.8
0.9
0
5000
10000
15000
20000
100 mA/g
50 mA/g
25 mA/g
10 mA/g
5 mA/g

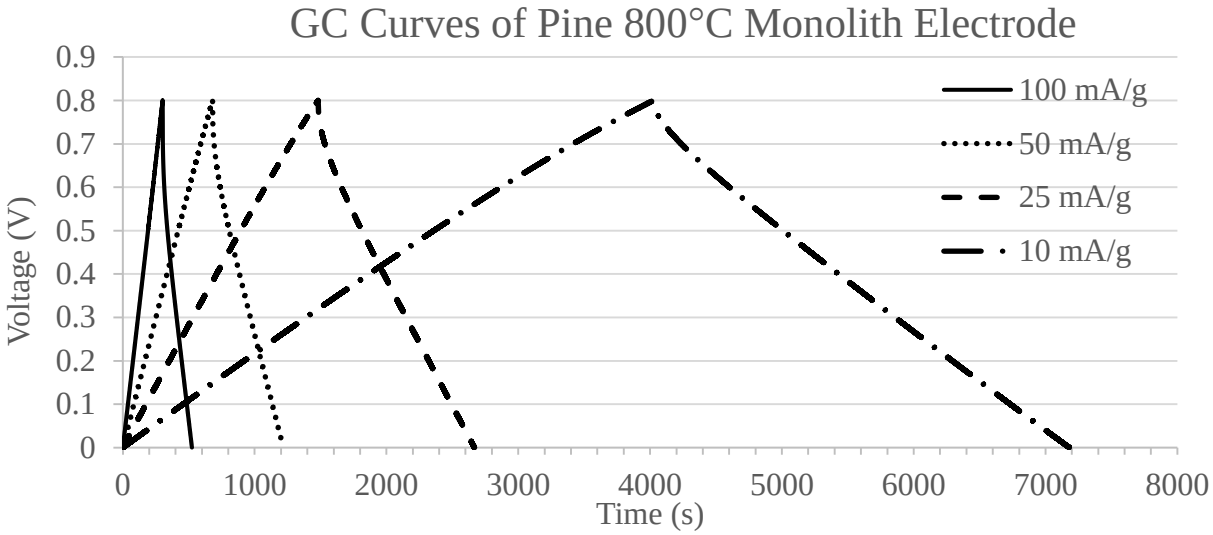
GC Curves of Pine 800°C Monolith Electrode
Voltage (V)
Time (s)
0
0.1
0.2
0.3
0.4
0.5
0.6
0.7
0.8
0.9
0
1000
2000
3000
4000
5000
6000
7000
8000
100 mA/g
50 mA/g
25 mA/g
10 mA/g

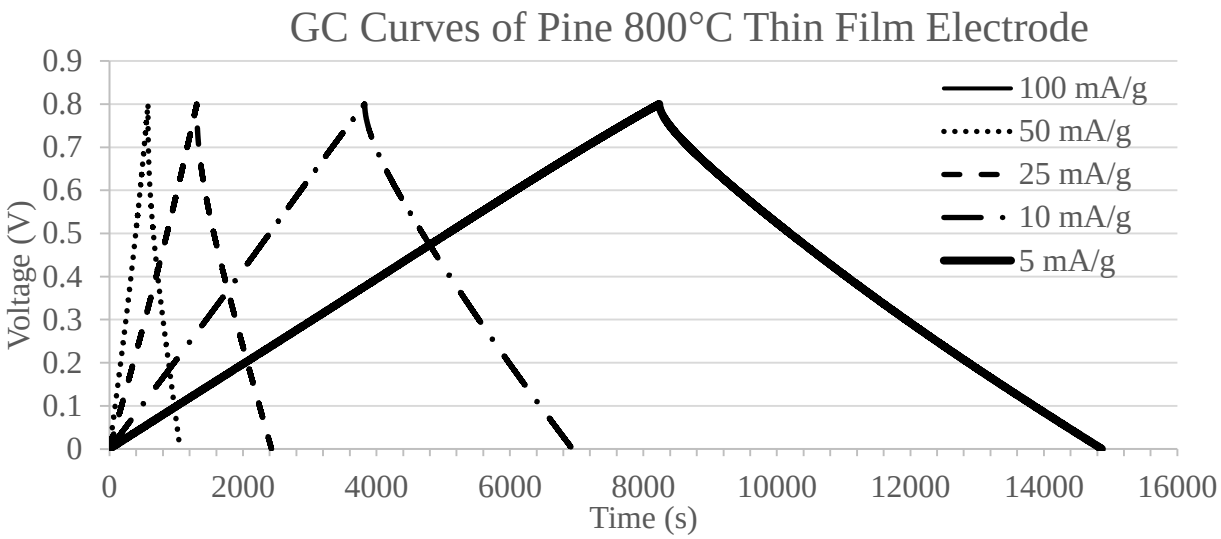
GC Curves of Pine 800°C Thin Film Electrode
Voltage (V)
Time (s)
0
0.1
0.2
0.3
0.4
0.5
0.6
0.7
0.8
0.9
0
2000
4000
6000
8000
10000
12000
14000
16000
100 mA/g
50 mA/g
25 mA/g
10 mA/g
5 mA/g

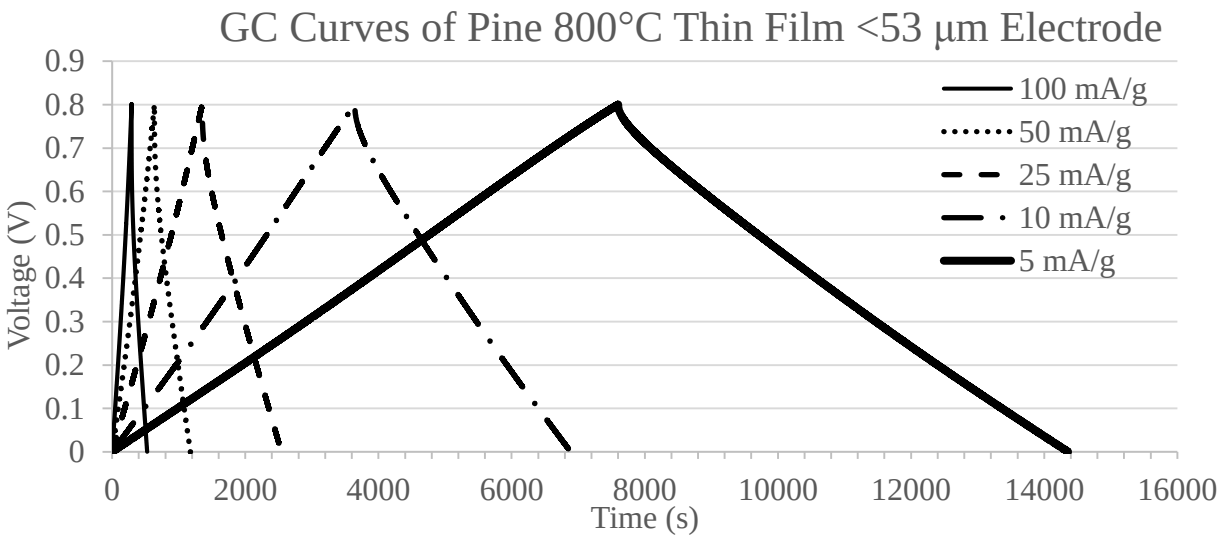
GC Curves of Pine 800°C Thin Film <53 μm Electrode
Voltage (V)
Time (s)
0
0.1
0.2
0.3
0.4
0.5
0.6
0.7
0.8
0.9
0
2000
4000
6000
8000
10000
12000
14000
16000
100 mA/g
50 mA/g
25 mA/g
10 mA/g
5 mA/g

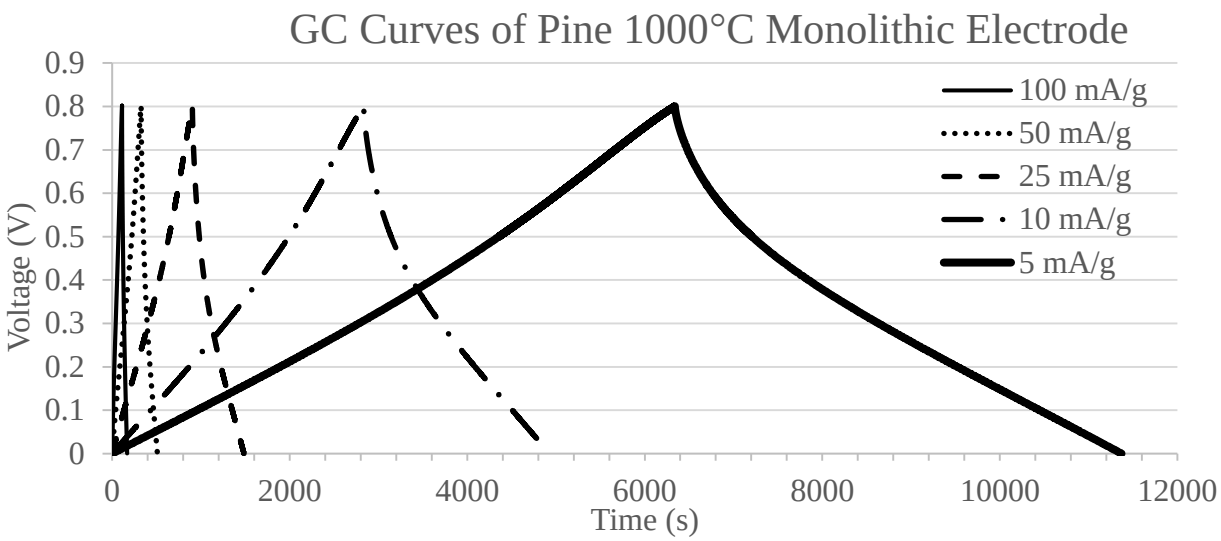
GC Curves of Pine 1000°C Monolithic Electrode
Voltage (V)
Time (s)
0
0.1
0.2
0.3
0.4
0.5
0.6
0.7
0.8
0.9
0
2000
4000
6000
8000
10000
12000
100 mA/g
50 mA/g
25 mA/g
10 mA/g
5 mA/g

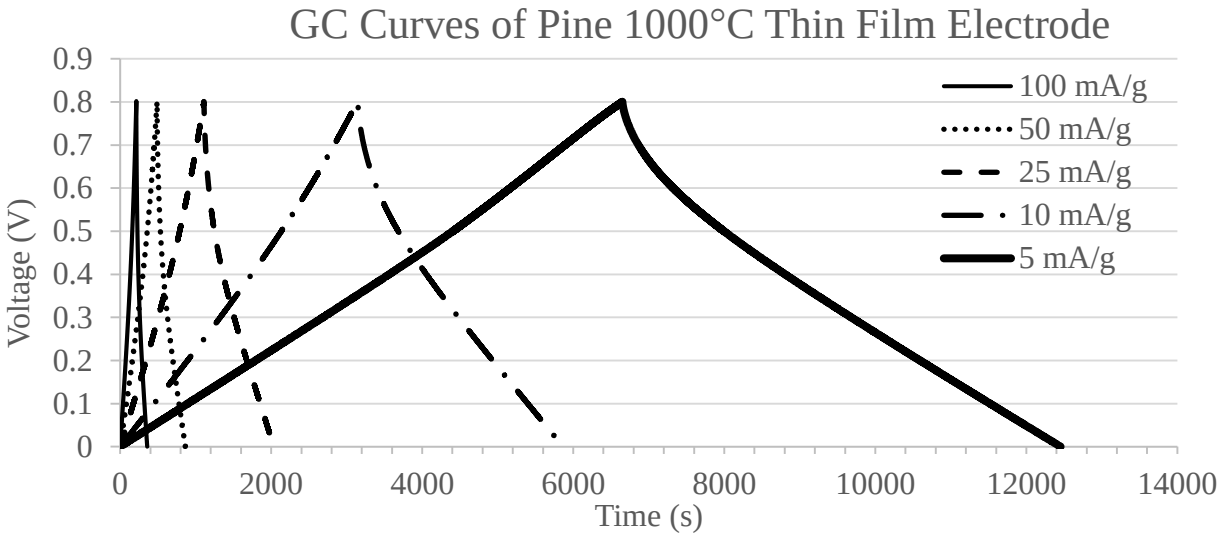
GC Curves of Pine 1000°C Thin Film Electrode
Voltage (V)
Time (s)
0
0.1
0.2
0.3
0.4
0.5
0.6
0.7
0.8
0.9
0
2000
4000
6000
8000
10000
12000
14000
100 mA/g
50 mA/g
25 mA/g
10 mA/g
5 mA/g

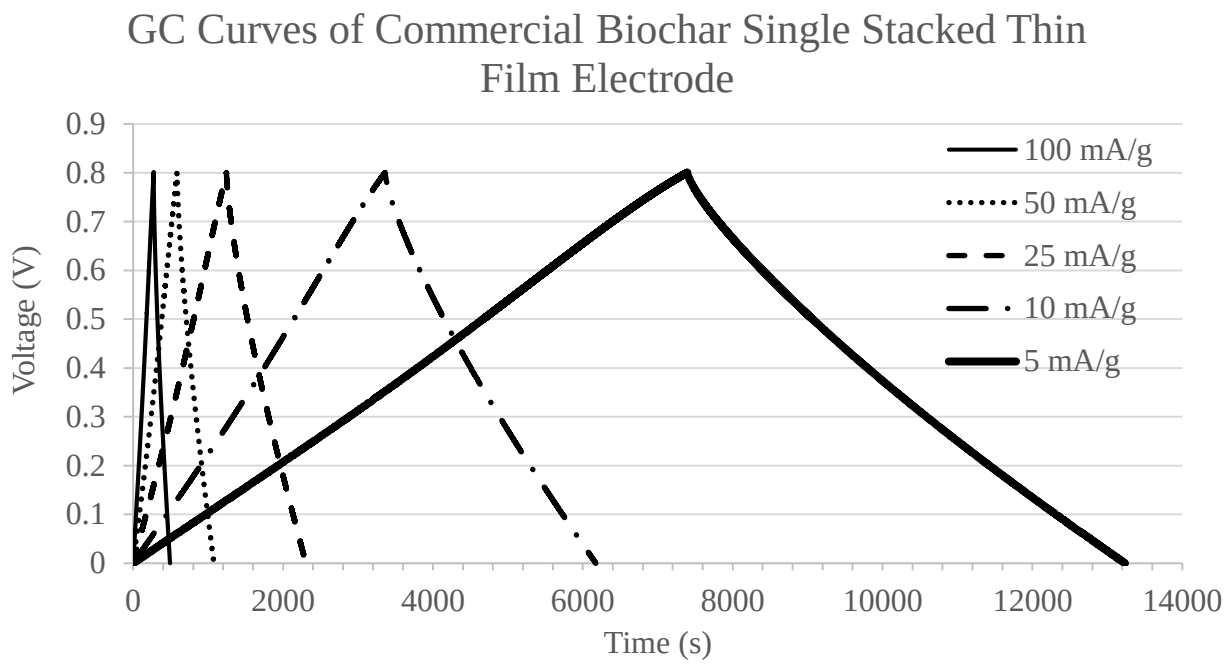
GC Curves of Commercial Biochar Single Stacked Thin Film Electrode
Voltage (V)
0.9
0.8
0.7
0.6
0.5
0.4
0.3
0.2
0.1
0
0
2000
4000
6000
8000
10000
12000
14000
Time (s)
100 mA/g
50 mA/g
25 mA/g
10 mA/g
5 mA/g

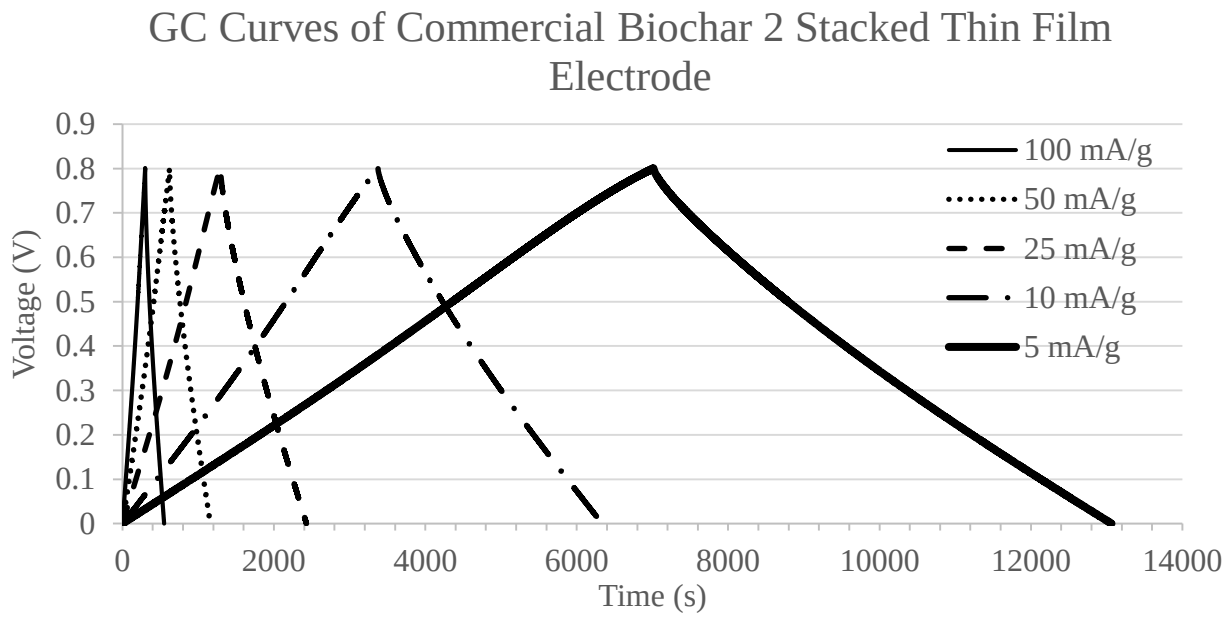
GC Curves of Commercial Biochar 2 Stacked Thin Film Electrode
Voltage (V)
0.9
0.8
0.7
0.6
0.5
0.4
0.3
0.2
0.1
0
0
2000
4000
6000
8000
10000
12000
14000
Time (s)
100 mA/g
50 mA/g
25 mA/g
10 mA/g
5 mA/g

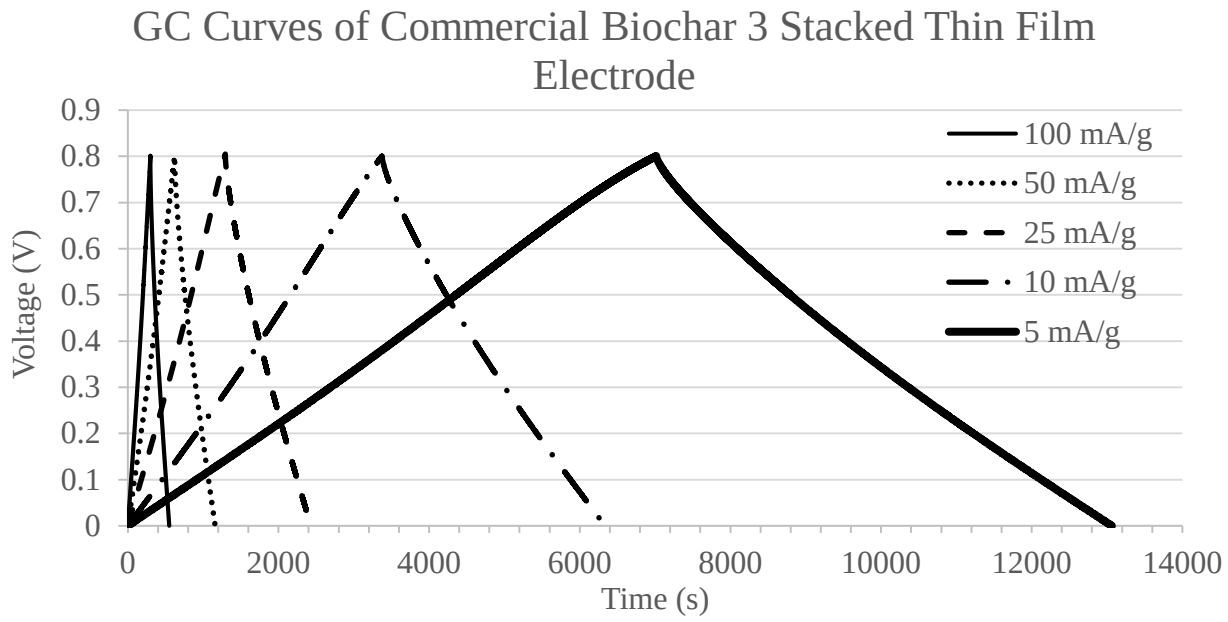
GC Curves of Commercial Biochar 3 Stacked Thin Film Electrode
Voltage (V)
0.9
0.8
0.7
0.6
0.5
0.4
0.3
0.2
0.1
0
0
2000
4000
6000
8000
10000
12000
14000
Time (s)
100 mA/g
50 mA/g
25 mA/g
10 mA/g
5 mA/g

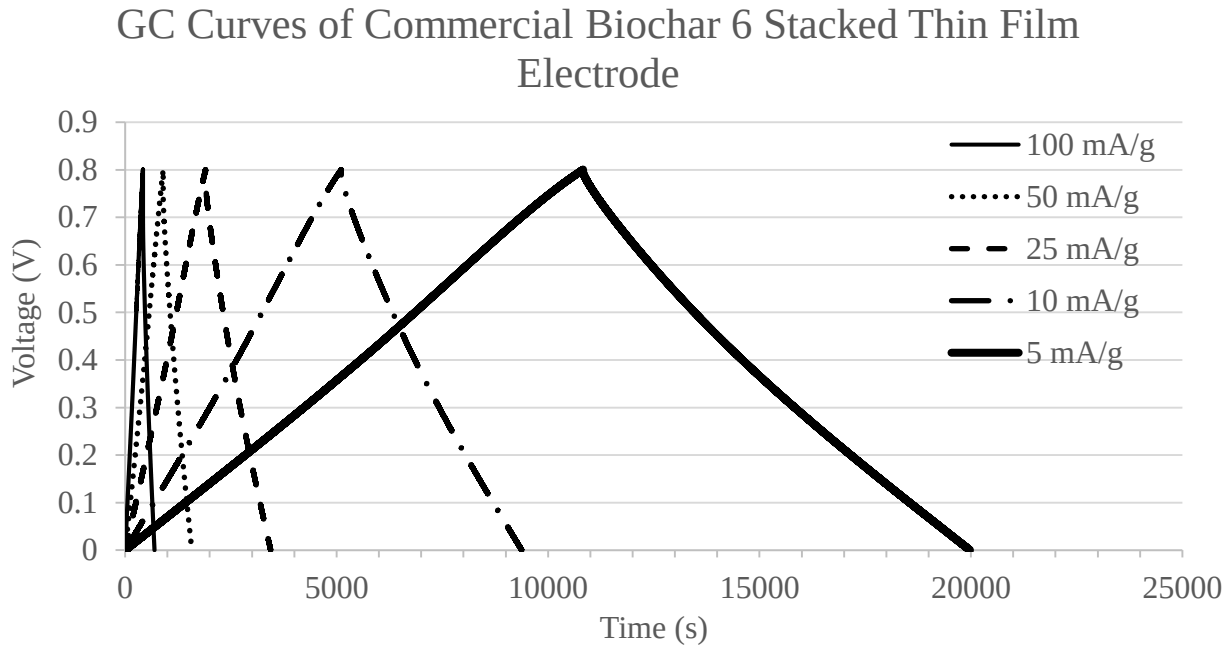
GC Curves of Commercial Biochar 6 Stacked Thin Film Electrode
Voltage (V)
0.9
0.8
0.7
0.6
0.5
0.4
0.3
0.2
0.1
0
0
5000
10000
15000
20000
25000
Time (s)
100 mA/g
50 mA/g
25 mA/g
10 mA/g
5 mA/g

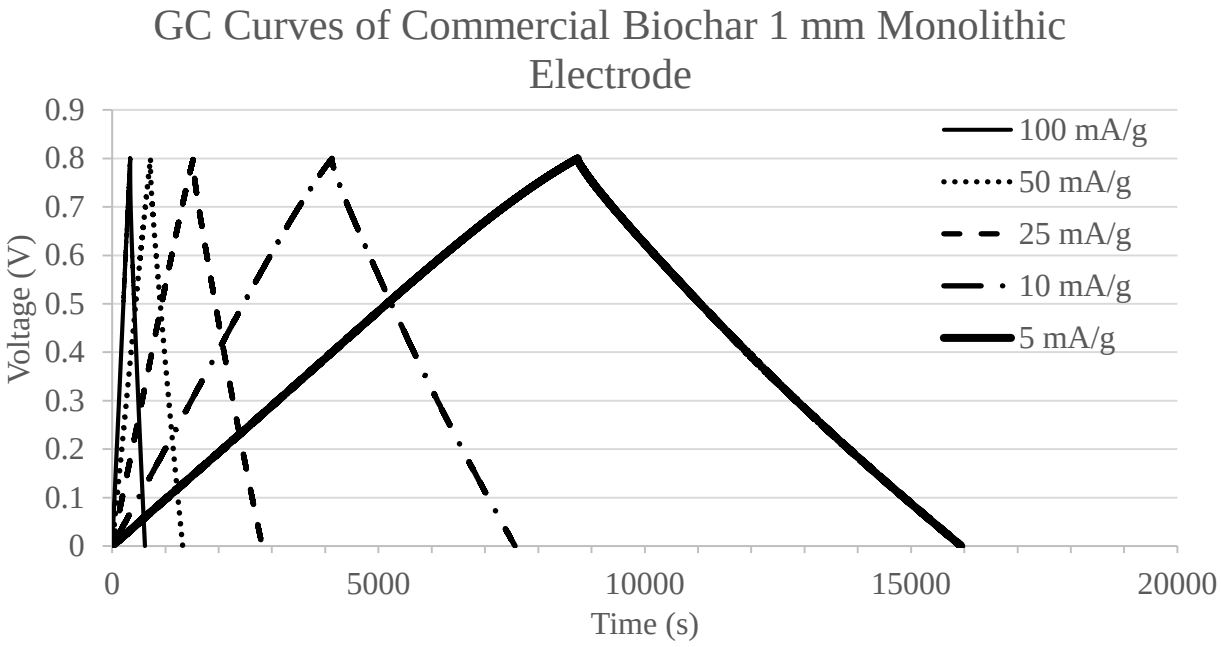
GC Curves of Commercial Biochar 1 mm Monolithic Electrode
Voltage (V)
0.9
0.8
0.7
0.6
0.5
0.4
0.3
0.2
0.1
0
0
5000
10000
15000
20000
Time (s)
100 mA/g
50 mA/g
25 mA/g
10 mA/g
5 mA/g

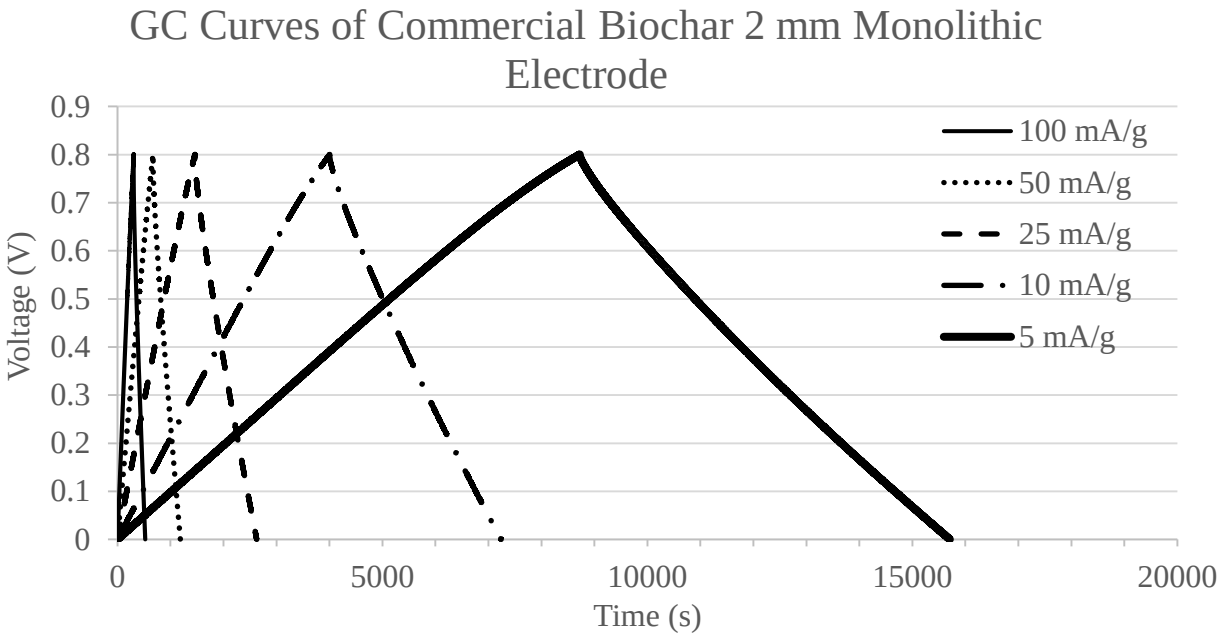
GC Curves of Commercial Biochar 2 mm Monolithic Electrode
Voltage (V)
0.9
0.8
0.7
0.6
0.5
0.4
0.3
0.2
0.1
0
0
5000
10000
15000
20000
Time (s)
100 mA/g
50 mA/g
25 mA/g
10 mA/g
5 mA/g

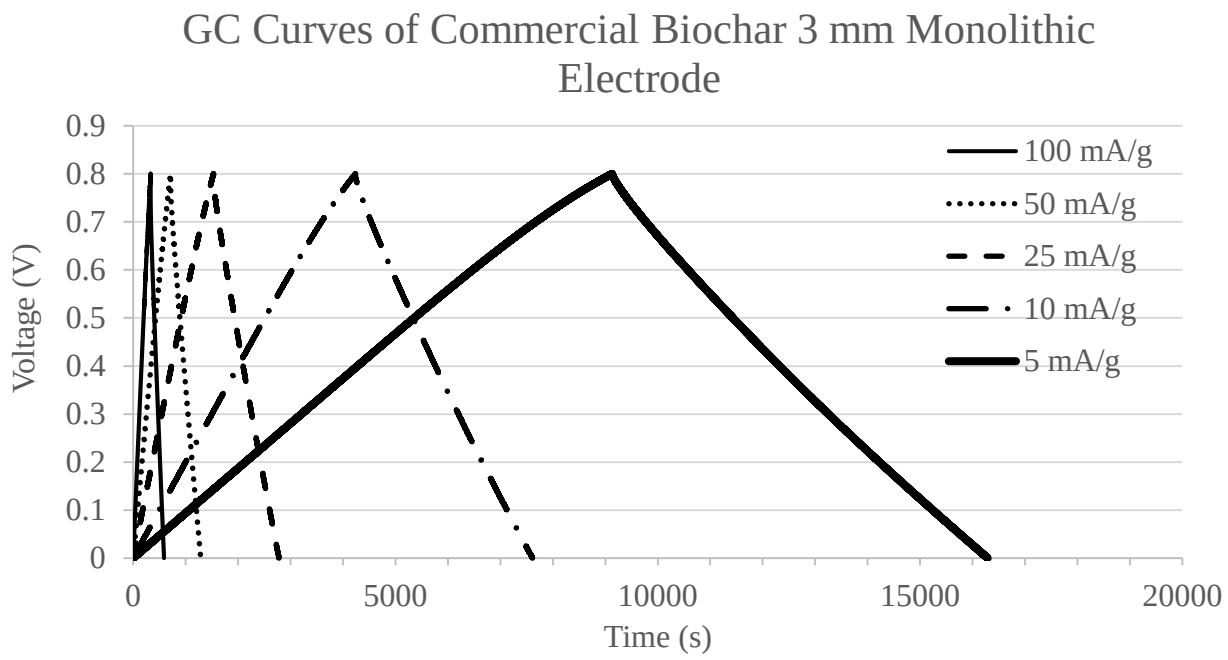

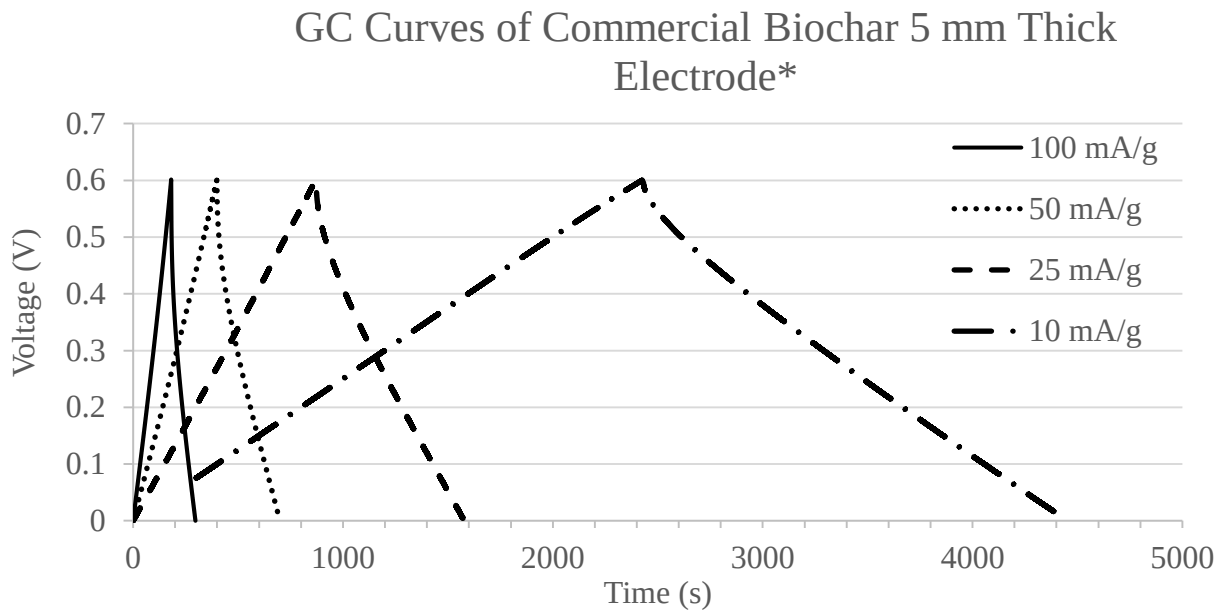

*This plot cube was tested before the testing method changed from -0.6 V – 0.6 V to – 0.8 V – 0.8 V

8.5 Appendix E: X-ray Photoelectron Spectroscopy Surface Chemistry Results

XPS data below is presented as a general overview of relative atomic %, a detailed look at carbon surface groups (C1s spectra), and a detailed look at oxygen surface groups (O1s spectra).

Summary of Relative Atomic % taken from high resolution fit:

Biochar	K2p3	Ca2p	C1s	O1s
Position (Pos)	Rel At.%	Rel At.%	Rel At.%	Rel At.%
Commercial	0.03	N/A	88.13	11.84
Maple 800	0.00	N/A	87.06	12.94
Maple 1000	0.02	N/A	90.87	9.12
Pine 800	0.00	N/A	92.73	7.27
Pine 1000	0.13	N/A	93.07	6.80
Maple 1000 post CVx2	N/A	0.45	89.21	10.34
Pine 1000 post CVx2	N/A	0.62	83.93	15.45

C1s and O1s Spectra:

Commercial Biochar:

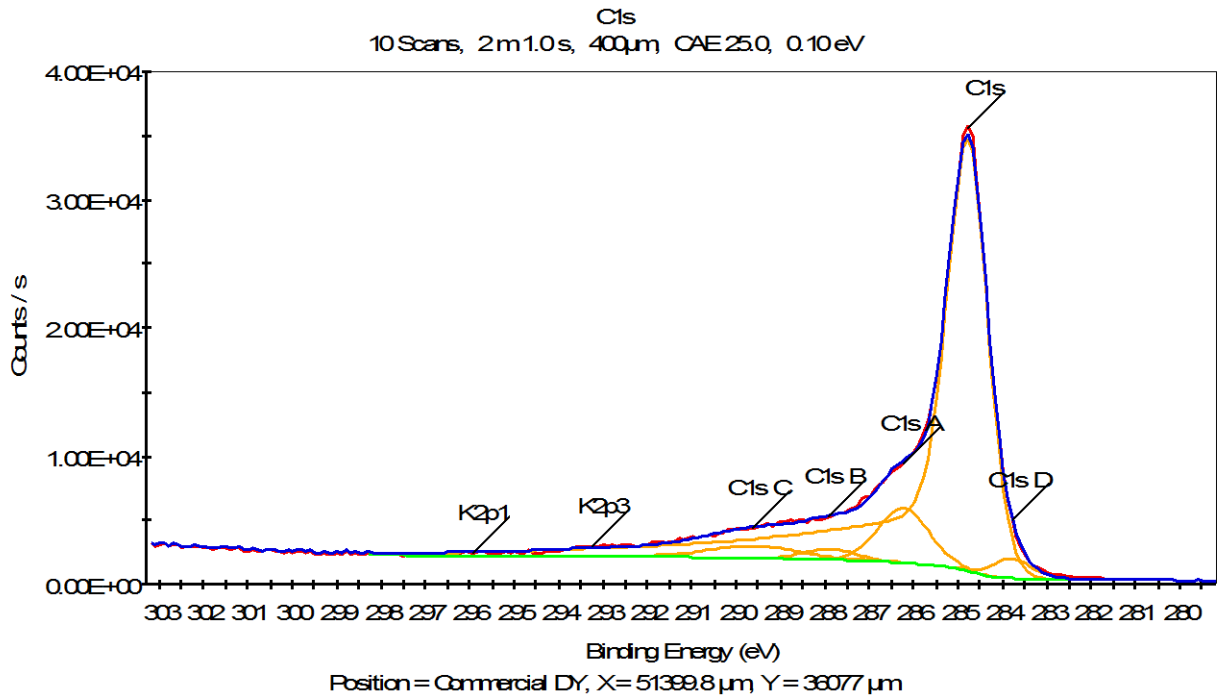

Elemental ID and Quantification

Name	*Peak BE*	*FWHM eV*	*Area (P) CPS.eV*	*Atomic %*	*Q*
C1s	284.78	1.10	55073.37	82.50	1
C1s A	286.23	1.35	6200.84	9.30	1
C1s B	287.90	1.35	1244.31	1.87	1
C1s C	289.61	2.40	2472.14	3.71	1
K2p3	293.23	1.38	72.26	0.04	1
K2p1	295.93	1.38	36.13	0.00	0
C1s D	283.78	1.04	1723.59	2.58	1

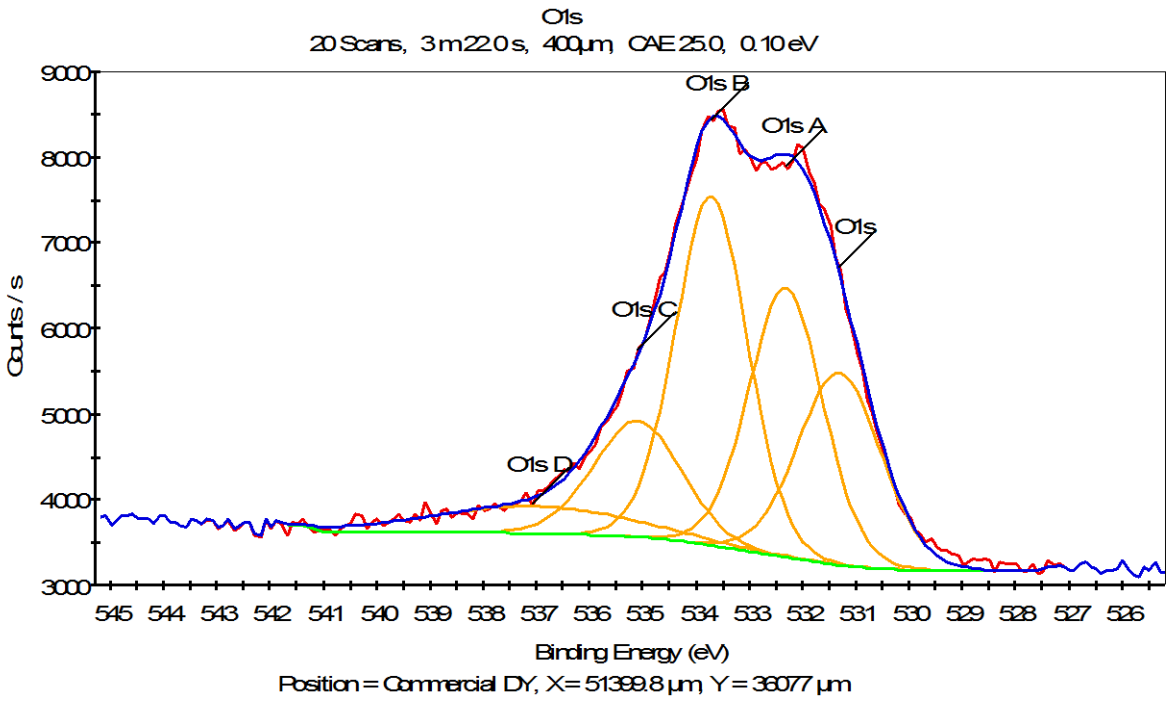

Elemental ID and Quantification

Name	*Peak BE*	*FWHM eV*	*Area (P) CPS.eV*	*Atomic %*	*Q*
O1s	531.30	1.82	4453.21	20.68	1
O1s A	532.31	1.64	5579.18	25.93	1
O1s B	533.71	1.60	7076.33	32.93	1
O1s C	535.09	1.94	2845.31	13.25	1
O1s D	537.07	4.51	1544.65	7.21	1

Maple 800℃:

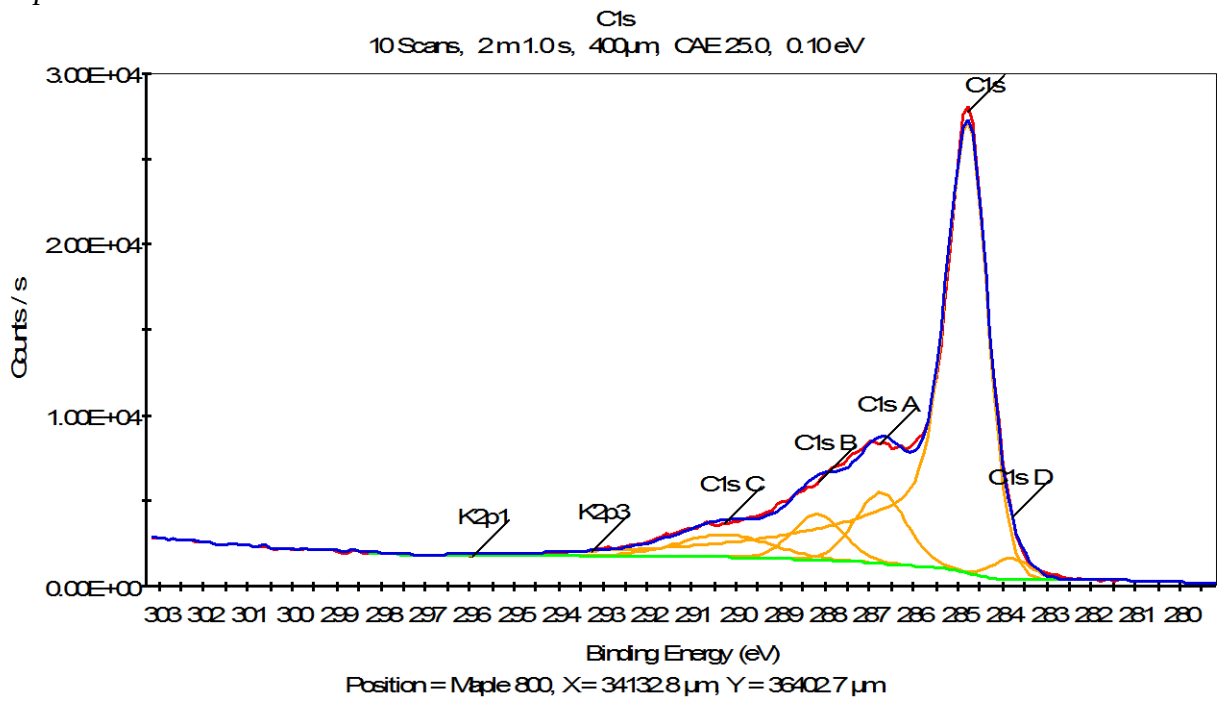

Elemental ID and Quantification

Name	*Peak BE*	*FWHM eV*	*Area (P) CPS.eV*	*Atomic %*	*Q*
C1s	284.78	1.14	43840.86	74.69	1
C1s A	286.74	1.35	6052.84	10.33	1
C1s B	288.15	1.35	3900.67	6.66	1
C1s C	290.26	2.40	3481.36	5.95	1
K2p3	293.23	1.43	0.00	0.00	1
K2p1	295.93	1.43	0.00	0.00	0
C1s D	283.78	1.04	1392.07	2.37	1

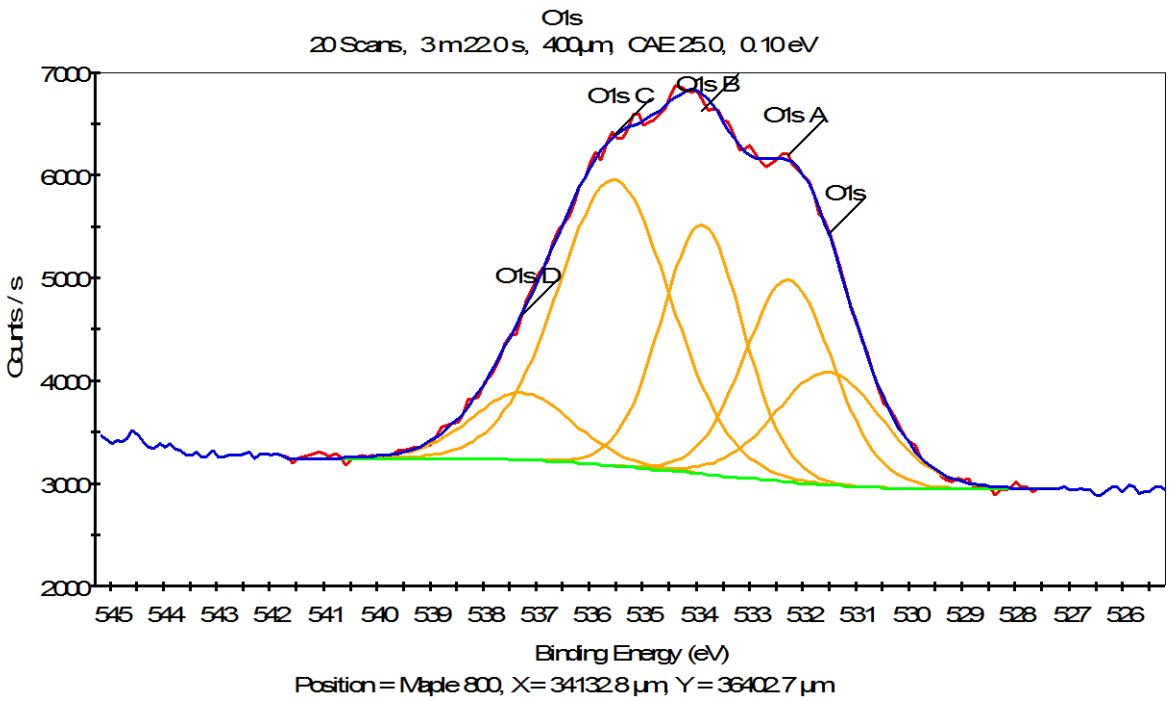

Elemental ID and Quantification

Name	*Peak BE*	*FWHM eV*	*Area (P) CPS.eV*	*Atomic %*	*Q*
O1s	531.50	2.35	2802.44	13.38	1
O1s A	532.26	1.97	4185.49	20.00	1
O1s B	533.88	1.82	4781.07	22.88	1
O1s C	535.53	2.50	7544.40	36.14	1
O1s D	537.27	2.23	1583.80	7.60	1

Maple 1000℃:

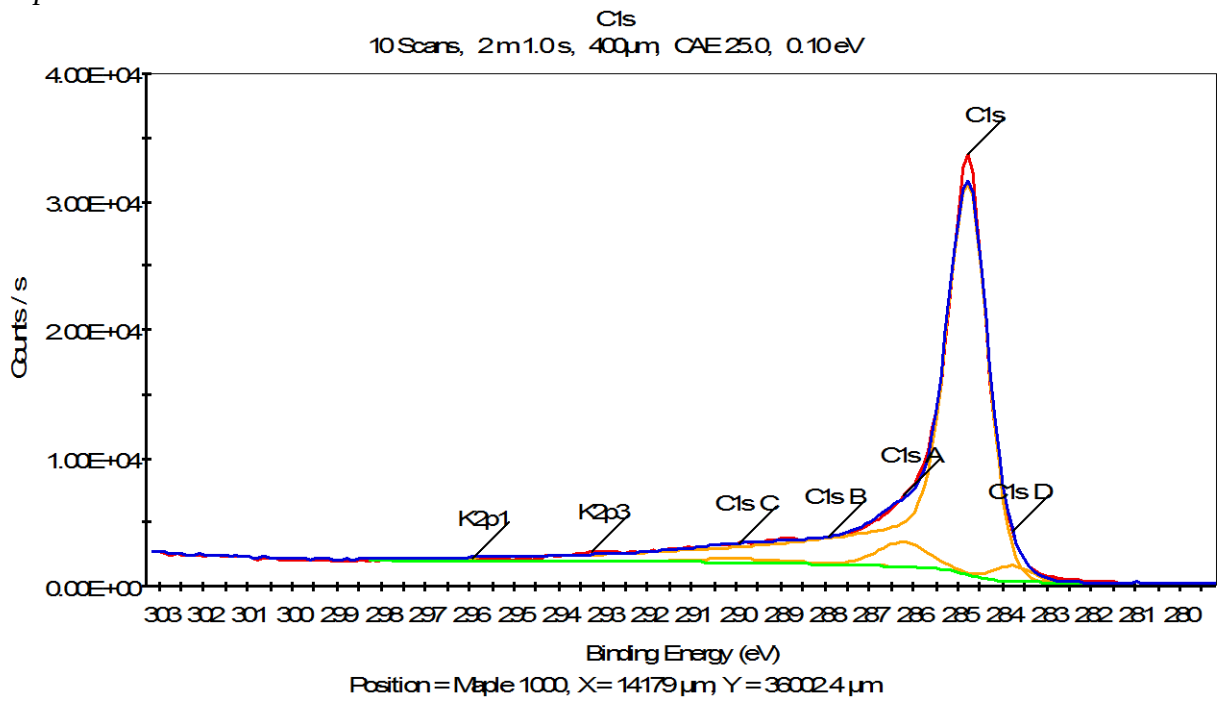

Elemental ID and Quantification

Name	*Peak BE*	*FWHM eV*	*Area (P) CPS.eV*	*Atomic %*	*Q*
C1s	284.78	1.10	49772.93	90.76	1
C1s A	286.23	1.35	2784.09	5.08	1
C1s B	287.90	1.40	0.00	0.00	1
C1s C	289.94	2.40	855.08	1.56	1
K2p3	293.23	1.38	33.09	0.02	1
K2p1	295.93	1.38	16.55	0.00	0
C1s D	283.78	1.04	1414.99	2.58	1

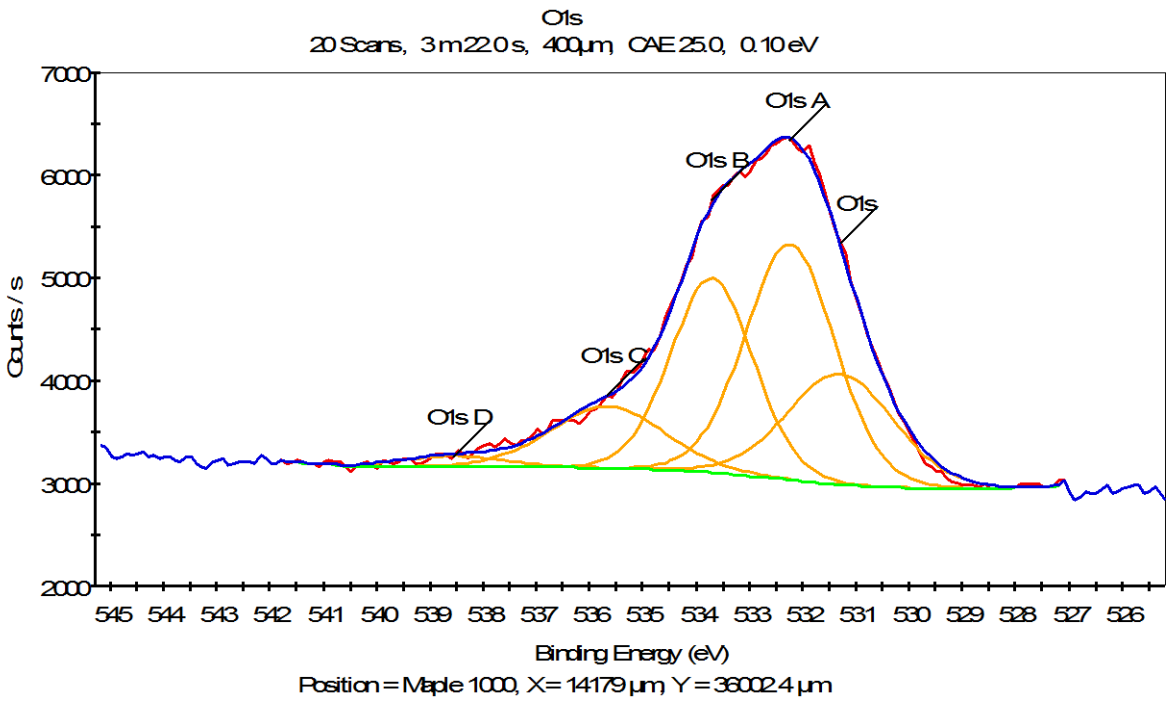

Elemental ID and Quantification

Name	*Peak BE*	*FWHM eV*	*Area (P) CPS.eV*	*Atomic %*	*Q*
O1s	531.29	2.35	2747.98	20.70	1
O1s A	532.23	1.97	4903.32	36.96	1
O1s B	533.70	1.82	3727.94	28.13	1
O1s C	535.65	2.51	1627.75	12.30	1
O1s D	538.57	2.23	252.35	1.91	1

Pine 800℃:

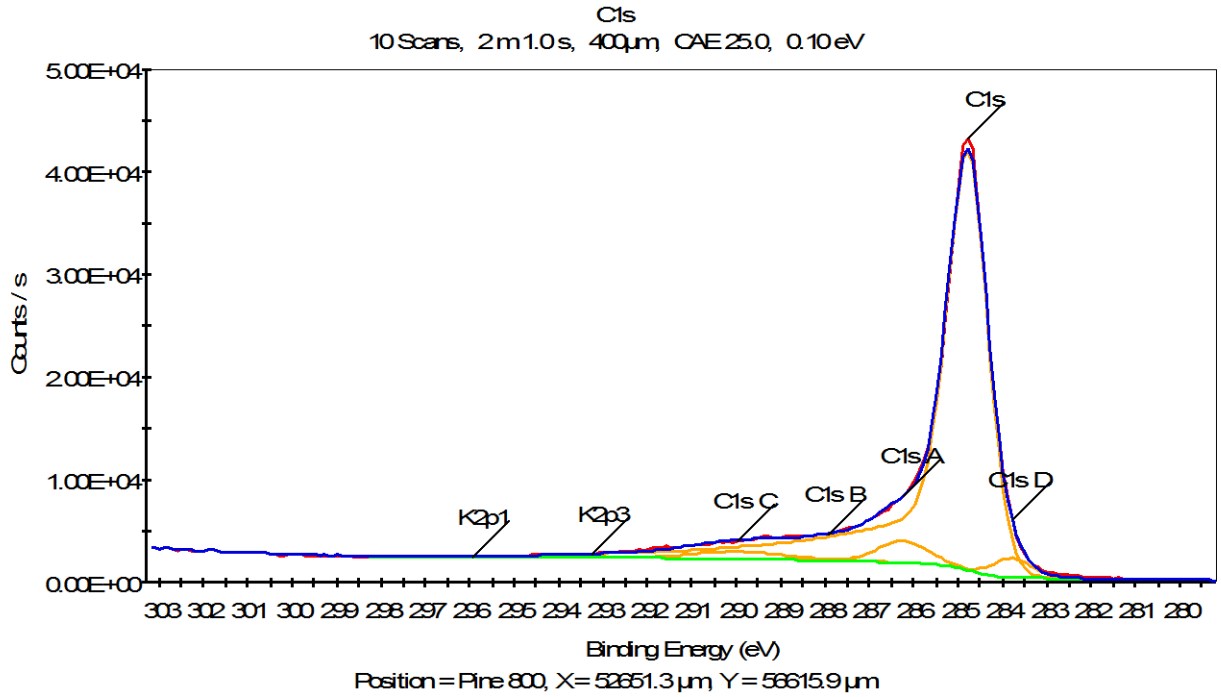

Elemental ID and Quantification

Name	*Peak BE*	*FWHM eV*	*Area (P) CPS.eV*	*Atomic %*	*Q*
C1s	284.78	1.10	62507.12	89.50	1
C1s A	286.23	1.35	3025.05	4.34	1
C1s B	287.90	1.35	254.46	0.37	1
C1s C	289.96	2.40	1921.43	2.76	1
K2p3	293.23	1.43	0.00	0.00	1
K2p1	295.93	1.43	0.00	0.00	0
C1s D	283.78	1.04	2122.43	3.04	1

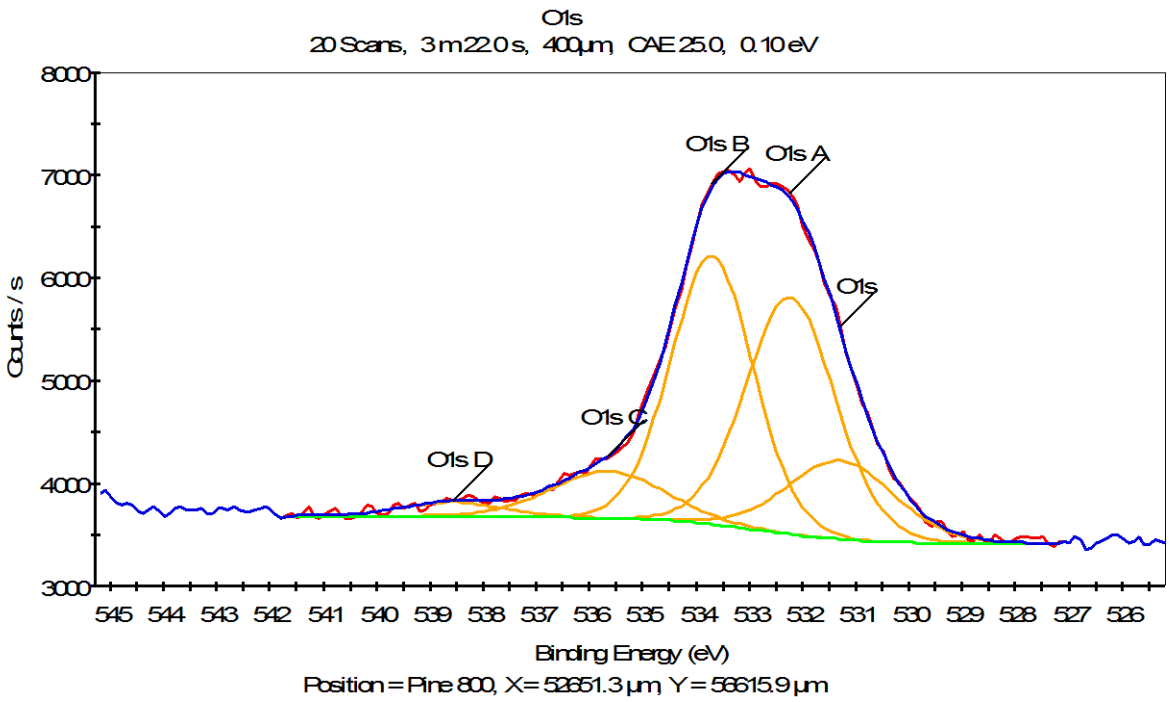

Elemental ID and Quantification

Name	*Peak BE*	*FWHM eV*	*Area (P) CPS.eV*	*Atomic %*	*Q*
O1s	531.29	2.35	1950.04	14.33	1
O1s A	532.23	1.97	4921.92	36.19	1
O1s B	533.70	1.82	5147.89	37.90	1
O1s C	535.65	2.50	1238.59	9.13	1
O1s D	538.57	2.23	331.17	2.45	1

Pine 1000℃:

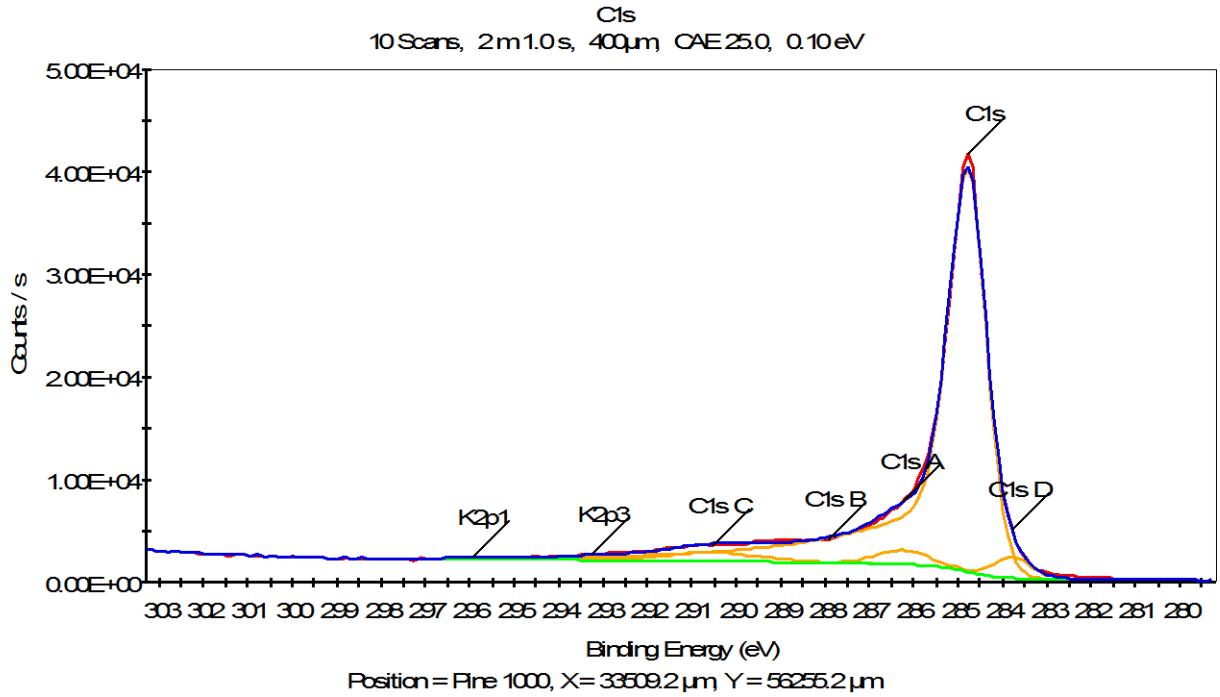

Elemental ID and Quantification

Name	*Peak BE*	*FWHM eV*	*Area (P) CPS.eV*	*Atomic %*	*Q*
C1s	284.78	1.04	58288.26	90.14	1
C1s A	286.23	1.35	2047.07	3.17	1
C1s B	287.90	1.40	0.00	0.00	1
C1s C	290.53	2.40	2099.31	3.26	1
K2p3	293.23	1.38	271.81	0.14	1
K2p1	295.93	1.38	135.90	0.00	0
C1s D	283.78	0.97	2136.06	3.30	1

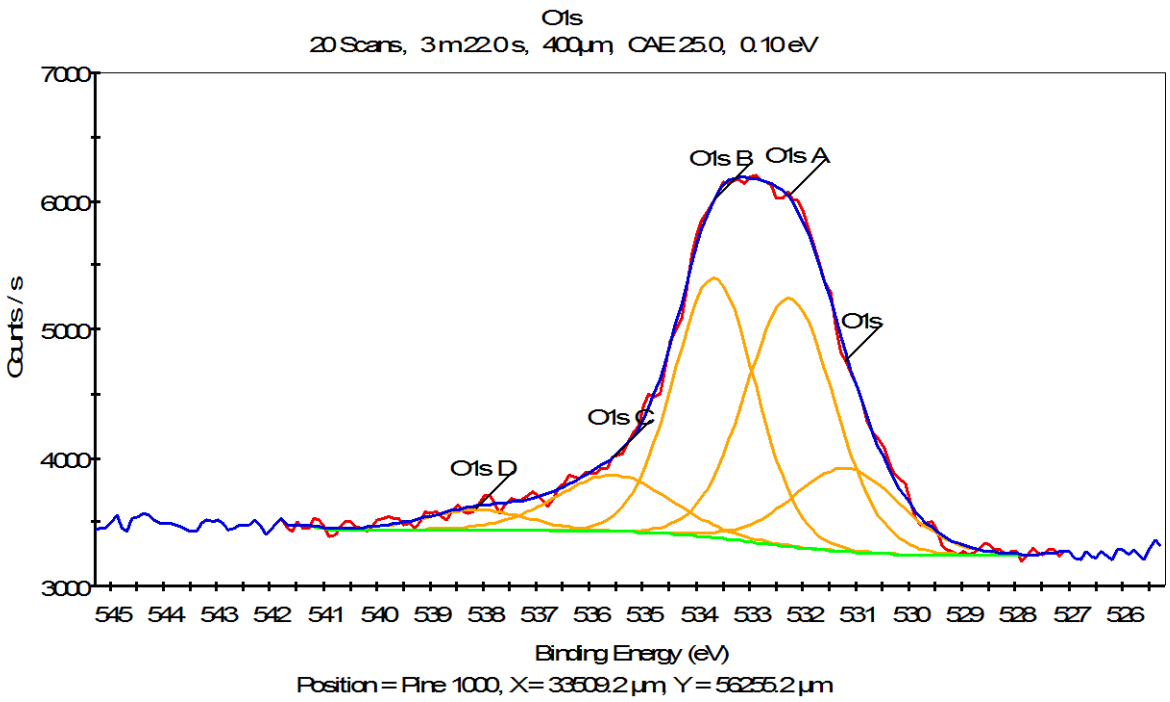

Elemental ID and Quantification

Name	*Peak BE*	*FWHM eV*	*Area (P) CPS.eV*	*Atomic %*	*Q*
O1s	531.18	2.35	1656.65	14.59	1
O1s A	532.24	1.97	4125.74	36.36	1
O1s B	533.65	1.82	3976.39	35.09	1
O1s C	535.55	2.51	1199.89	10.60	1
O1s D	538.12	2.23	379.60	3.36	1

Maple 1000℃ post CVx2:

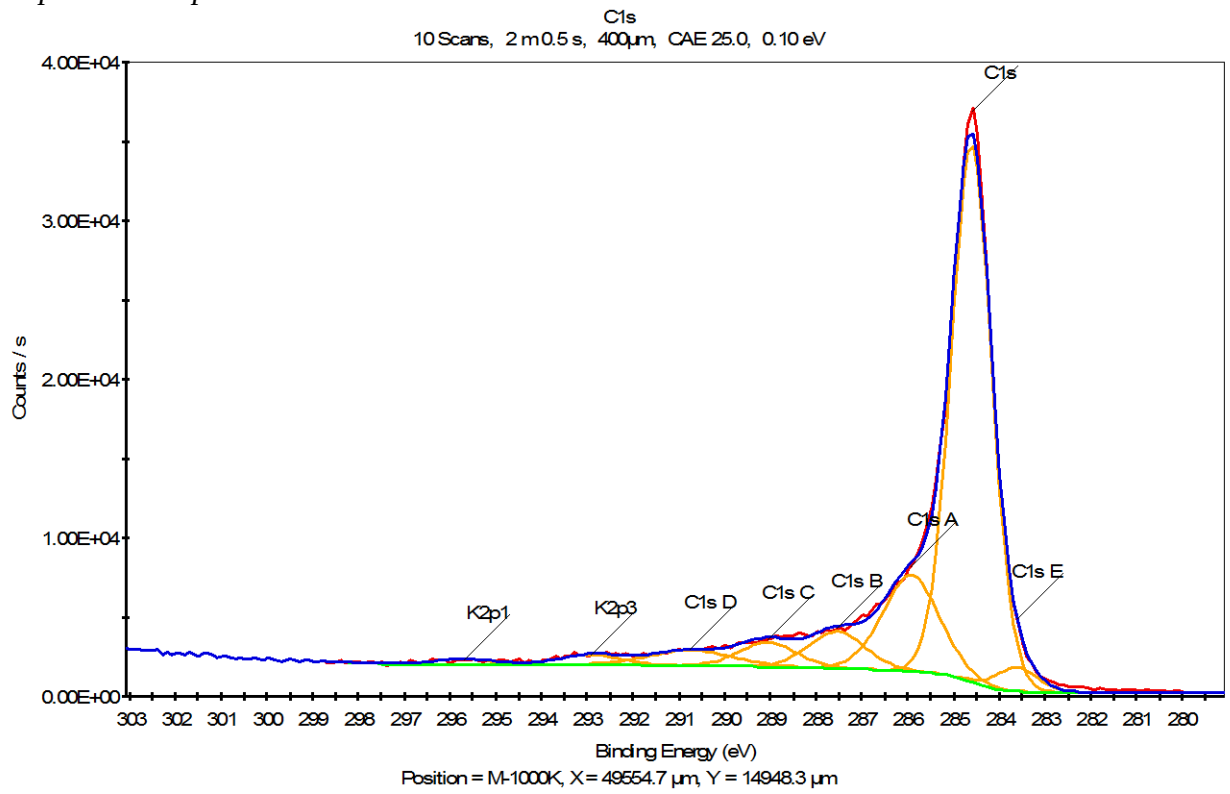

Elemental ID and Quantification

Name	*Peak BE*	*FWHM eV*	*Area (P) CPS.eV*	*Atomic %*	*Q*
C1s	284.61	1.04	37902.84	66.08	1
C1s A	285.92	1.44	9497.25	16.57	1
C1s B	287.54	1.44	3629.41	6.34	1
C1s C	289.05	1.44	2413.61	4.22	1
K2p3	292.92	1.54	1057.62	0.00	0
K2p1	295.69	1.54	528.81	0.00	0
C1s D	290.74	2.11	2216.55	3.88	1
C1s E	283.61	1.04	1666.73	2.90	1

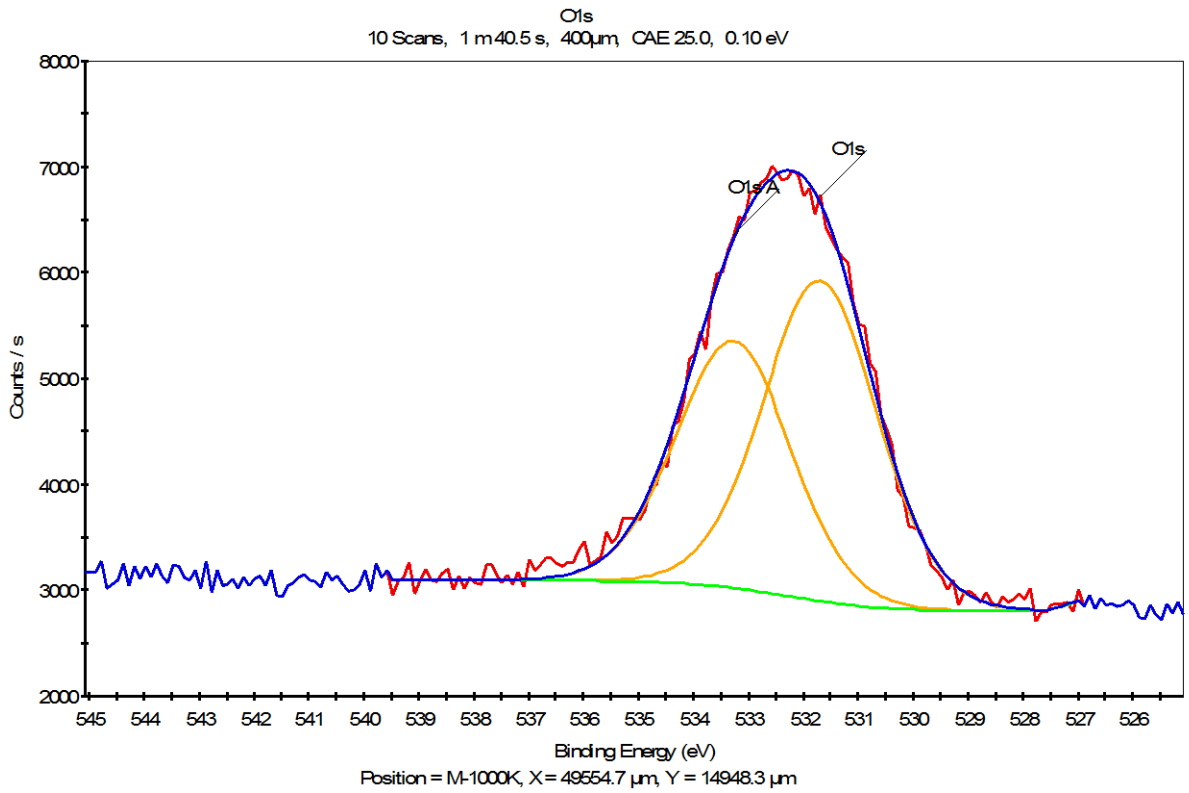

Elemental ID and Quantification

Name	*Peak BE*	*FWHM eV*	*Area (P) CPS.eV*	*Atomic %*	*Q*
O1s	531.69	2.45	8009.68	56.39	1
O1s A	533.27	2.45	6187.51	43.61	1

Pine 1000℃ post CVx2:

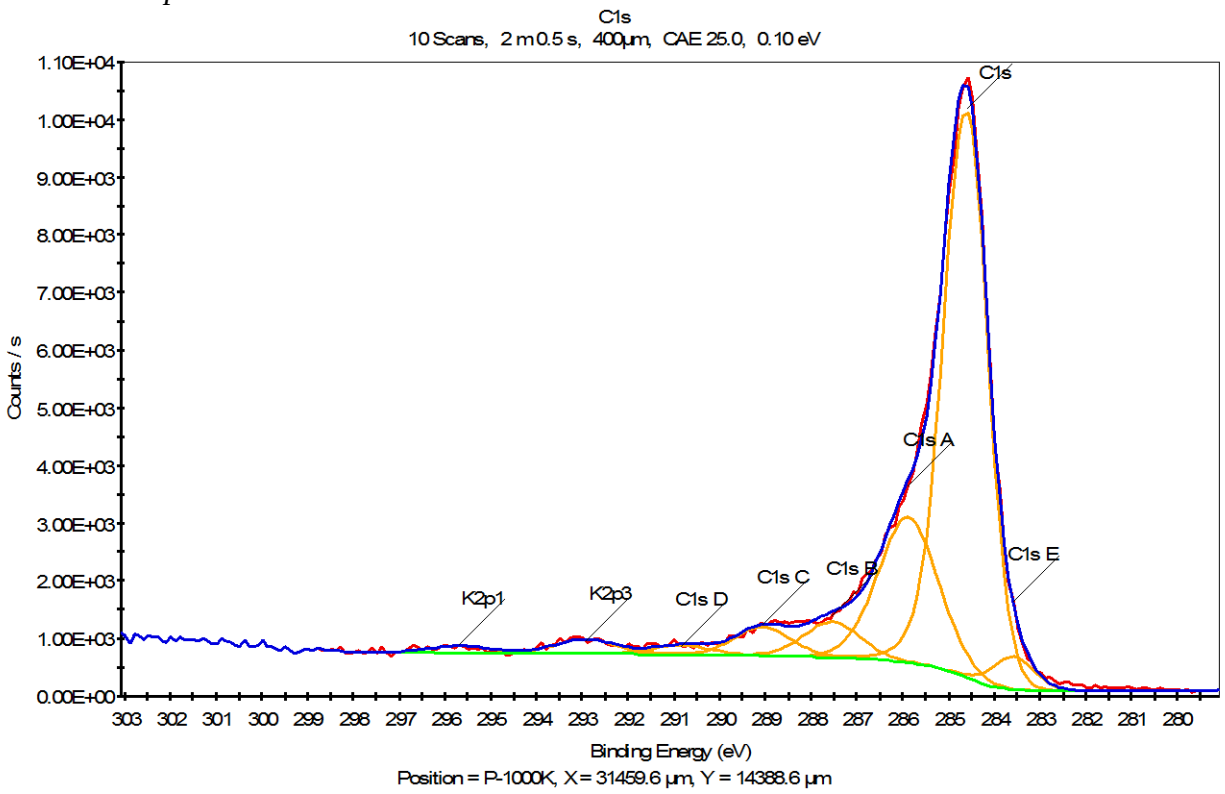

Elemental ID and Quantification

Name	*Peak BE*	*FWHM eV*	*Area (P) CPS.eV*	*Atomic %*	*Q*
C1s	284.58	1.13	12159.18	63.96	1
C1s A	285.88	1.54	4207.55	22.15	1
C1s B	287.54	1.44	966.37	5.09	1
C1s C	289.05	1.44	779.34	4.11	1
K2p3	292.92	1.54	421.72	0.00	0
K2p1	295.69	1.54	210.86	0.00	0
C1s D	290.85	1.45	256.51	1.35	1
C1s E	283.58	1.04	634.14	3.33	1

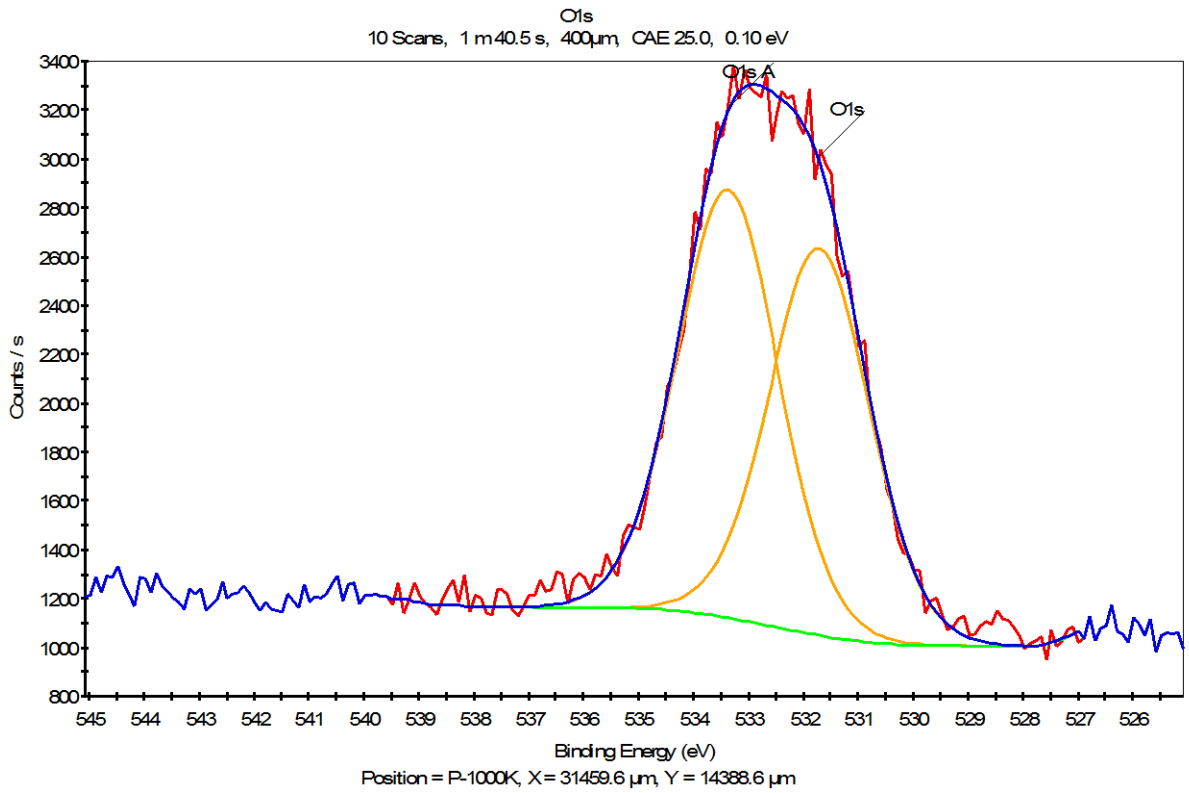

Elemental ID and Quantification

Name	*Peak BE*	*FWHM eV*	*Area (P) CPS.eV*	*Atomic %*	*Q*
O1s	531.70	2.16	3704.91	47.42	1
O1s A	533.38	2.16	4103.22	52.58	1

8.6 Appendix F: Cyclic Voltammetry Pre-treatment Cycle Progression Curves

The y-axes of the CV pre-treatment plots are current, in Amperes. They have not been normalized to the electrode masses, and therefore a range of y-values are seen between the different cells. The focus of these plots is to qualitatively show the progression and resulting shape of the CV curve, which hints at pseudocapacitance.

"Thin Film" electrodes noted in the plot title are those with particle sizes of 53 – 212 μm. Thin films with particles <53 μm are specified. The number following the wood type in the plot titles in the pyrolysis temperature in degrees Celsius.

Unfortunately, the CV pre-treatment data for the Pine 800°C thin film with particles < 53μm was lost.

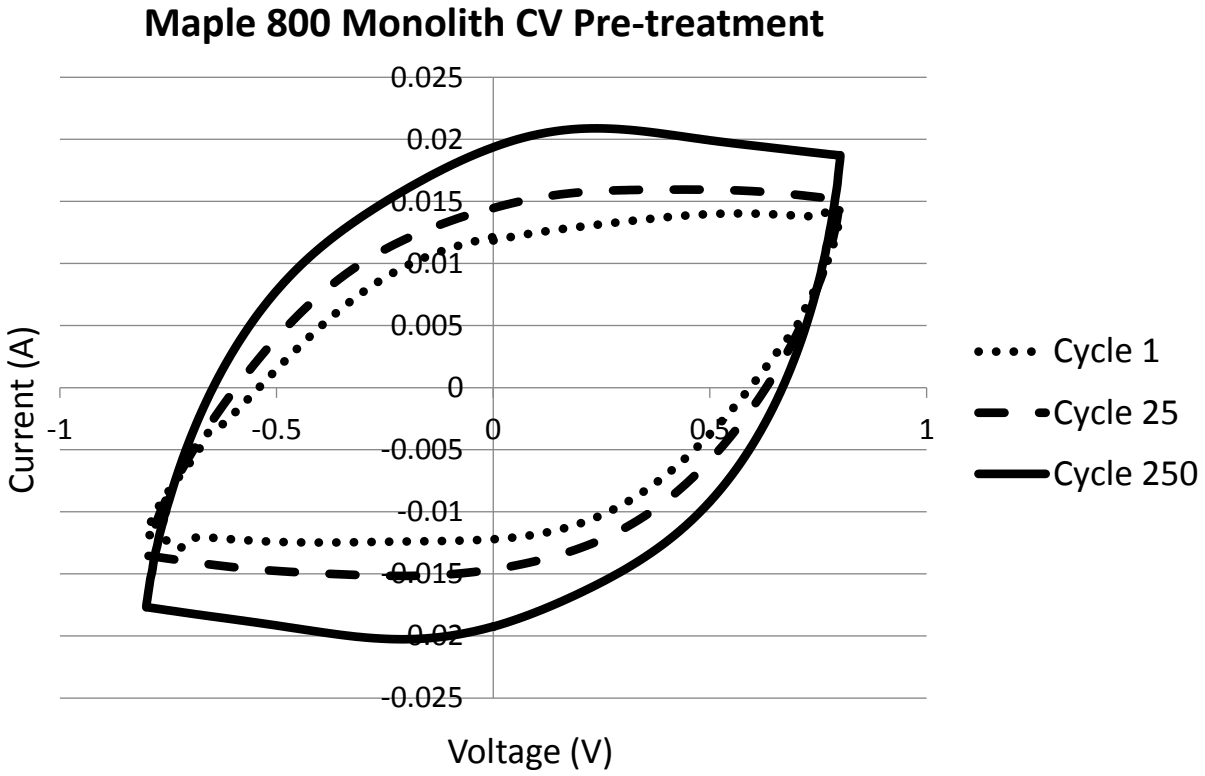

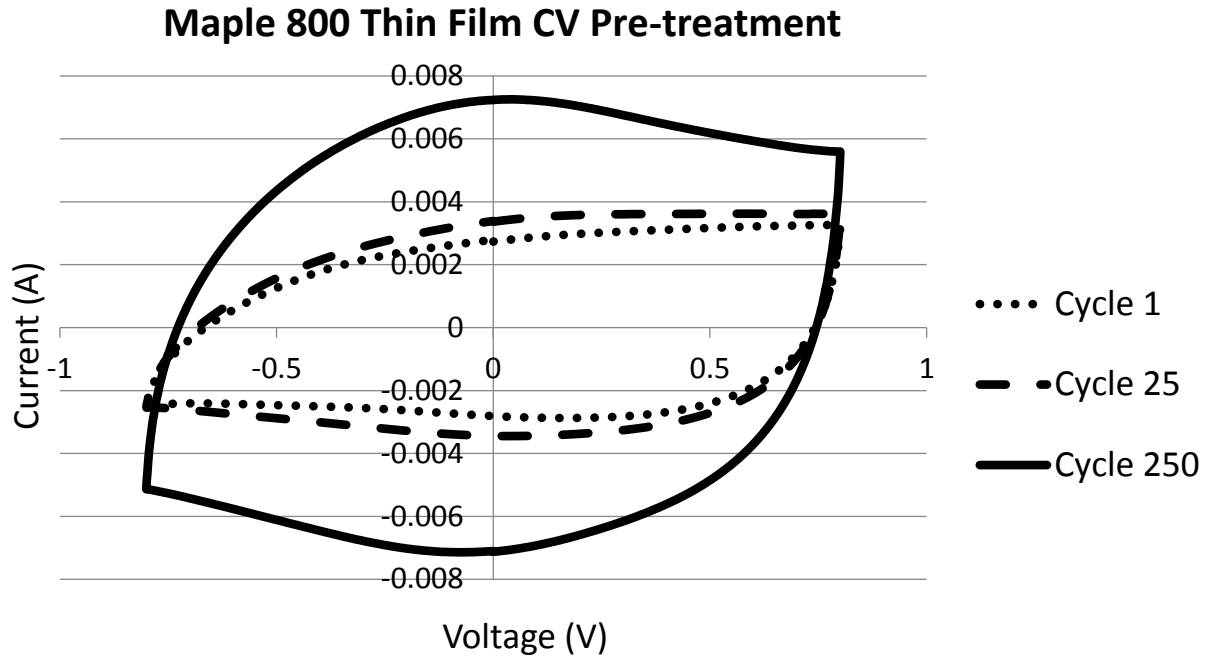

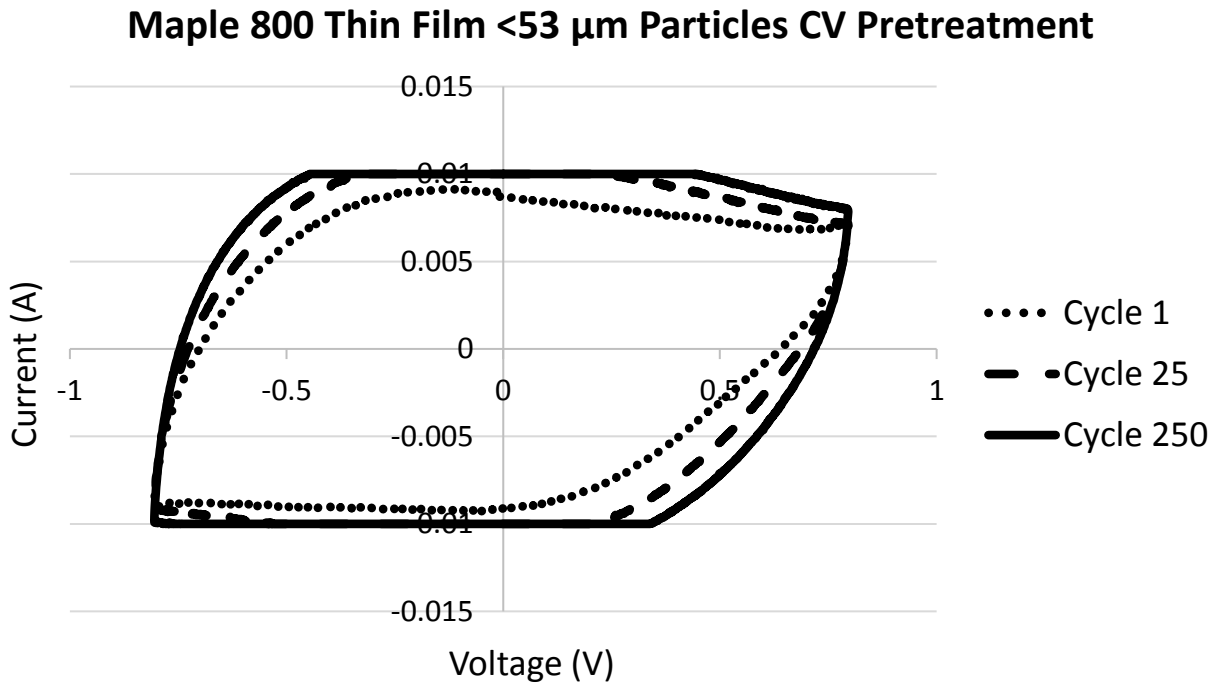

The Maple 800 Thin Film <53 µm cell was run on the older, analog potentiostat. During the CV run, the current went outside of the manually set current range as displayed in the above plot by the plateaus. Repeating the measurement would have changed the results. As such, the original data is shown above.

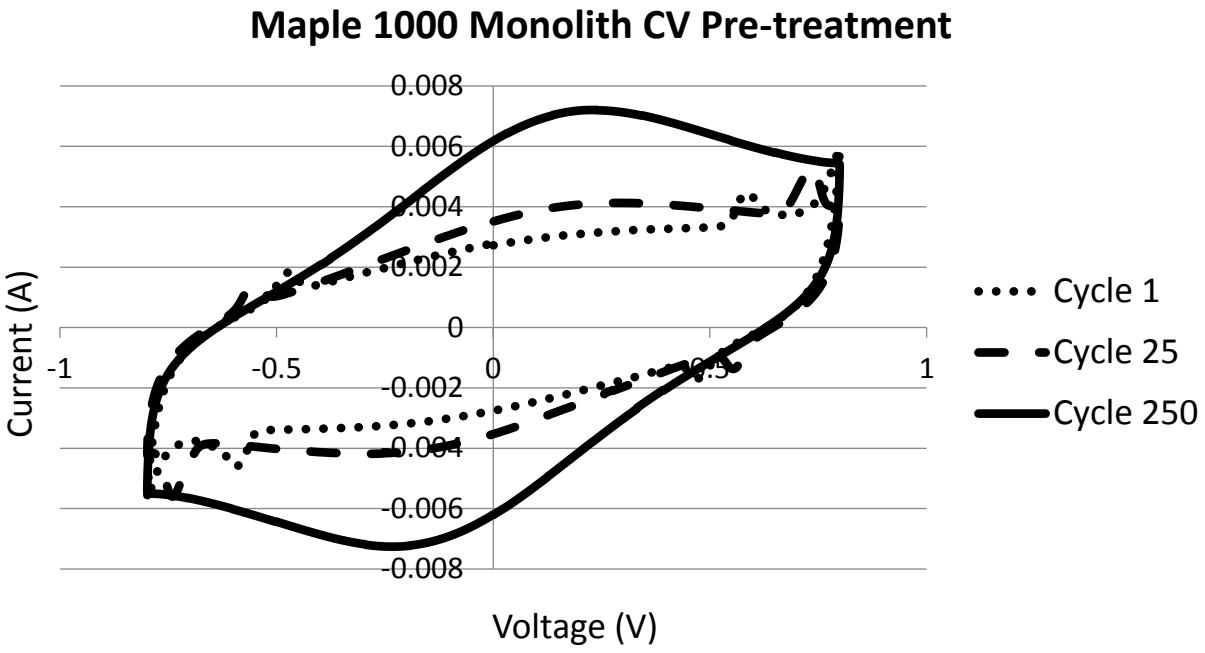
Maple 1000 Monolith CV Pre-treatment
0.008
0.006
0.004
0.002
0
-0.002
-0.004
-0.006
-0.008
-1
-0.5
0
0.5
1
Current (A)
Voltage (V)
Cycle 1
Cycle 25
Cycle 250

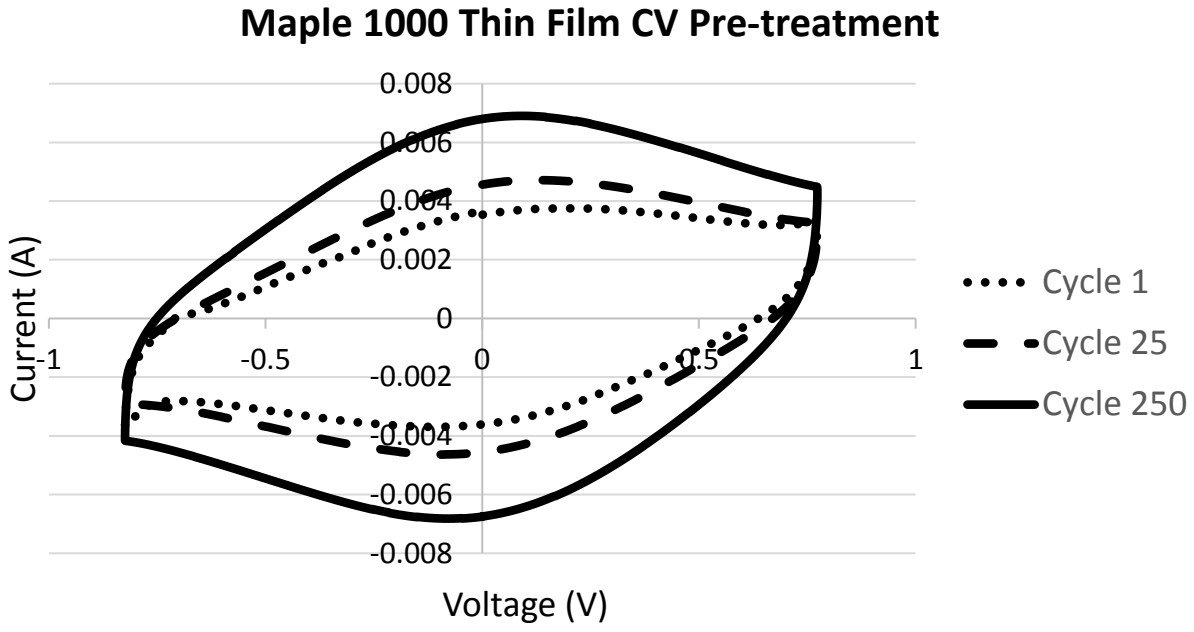
Maple 1000 Thin Film CV Pre-treatment
0.008
0.006
0.004
0.002
0
-0.002
-0.004
-0.006
-0.008
-1
-0.5
0
0.5
1
Current (A)
Voltage (V)
Cycle 1
Cycle 25
Cycle 250

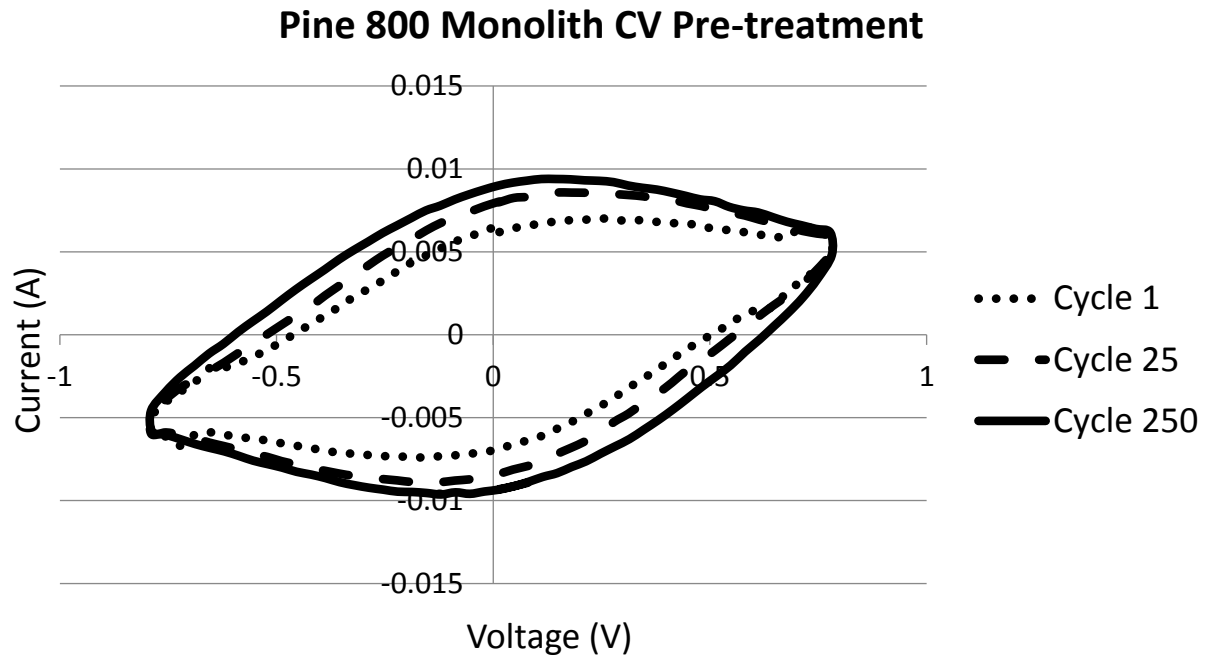
Pine 800 Monolith CV Pre-treatment
0.015
0.01
0.005
0
-0.005
-0.01
-0.015
-1
-0.5
0
0.5
1
Current (A)
Voltage (V)
Cycle 1
Cycle 25
Cycle 250

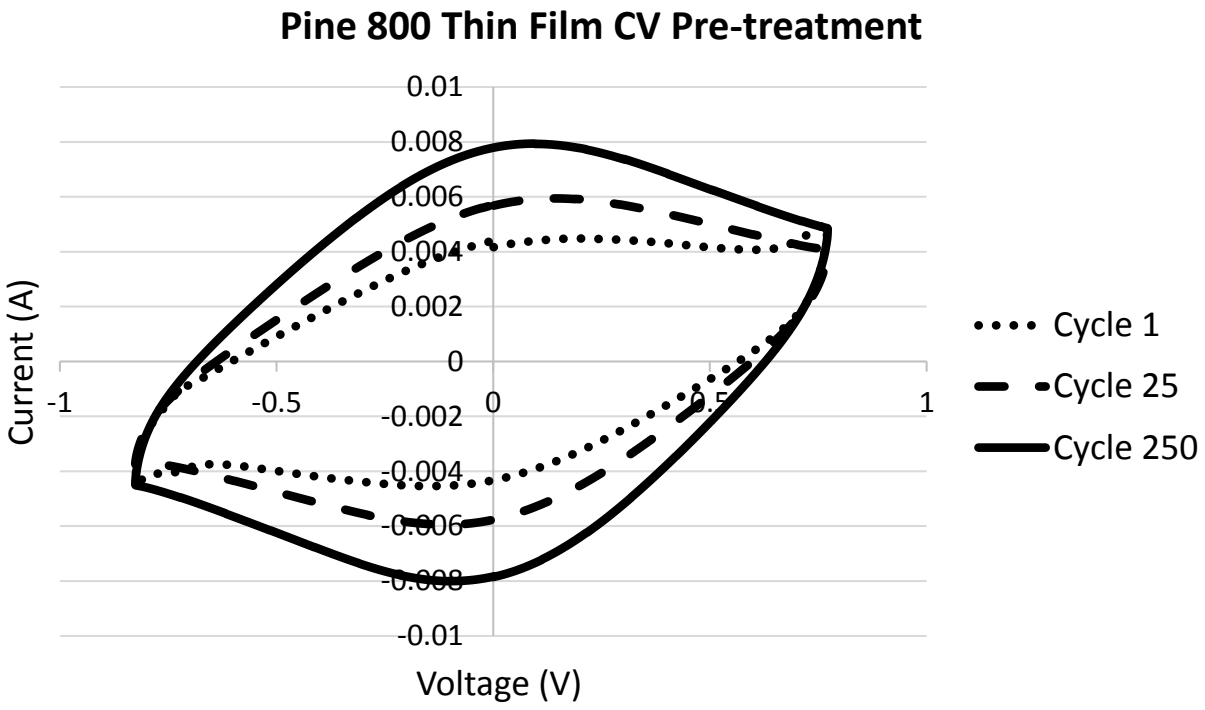
Pine 800 Thin Film CV Pre-treatment
0.01
0.008
0.006
0.004
0.002
0
-0.002
-0.004
-0.006
-0.008
-0.01
-1
-0.5
0
0.5
1
Current (A)
Voltage (V)
Cycle 1
Cycle 25
Cycle 250

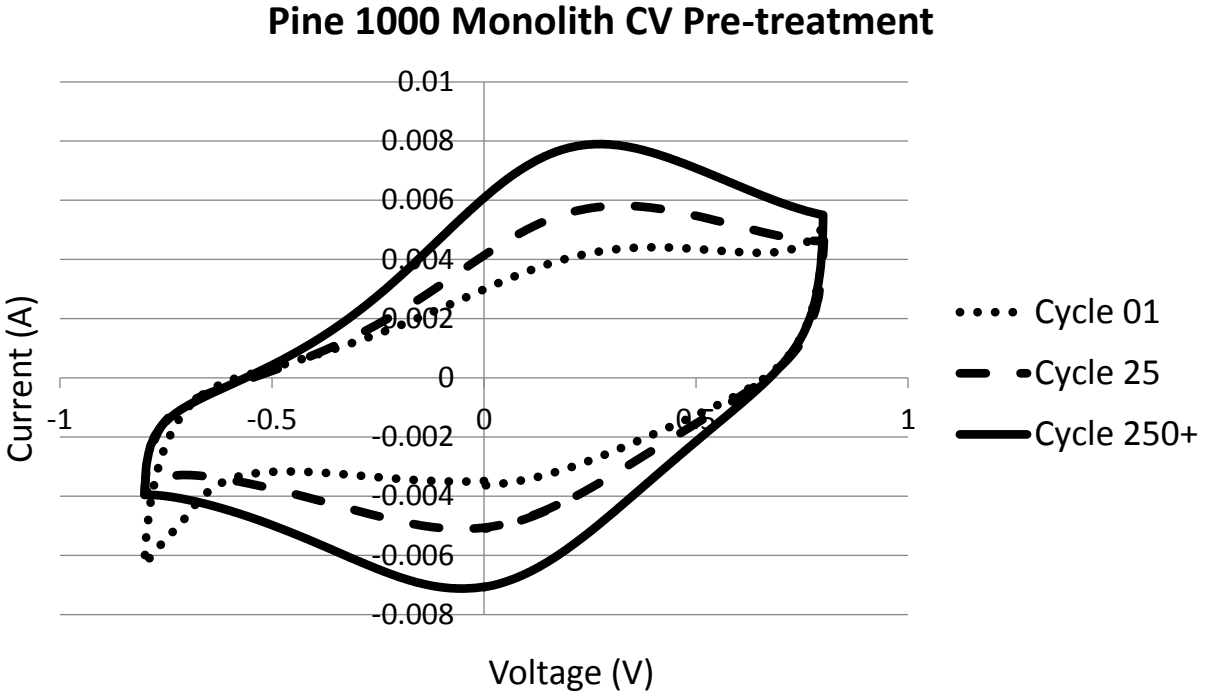
Pine 1000 Monolith CV Pre-treatment
0.01
0.008
0.006
0.004
0.002
0
-0.002
-0.004
-0.006
-0.008
-1
-0.5
0
0.5
1
Current (A)
Voltage (V)
Cycle 01
Cycle 25
Cycle 250+

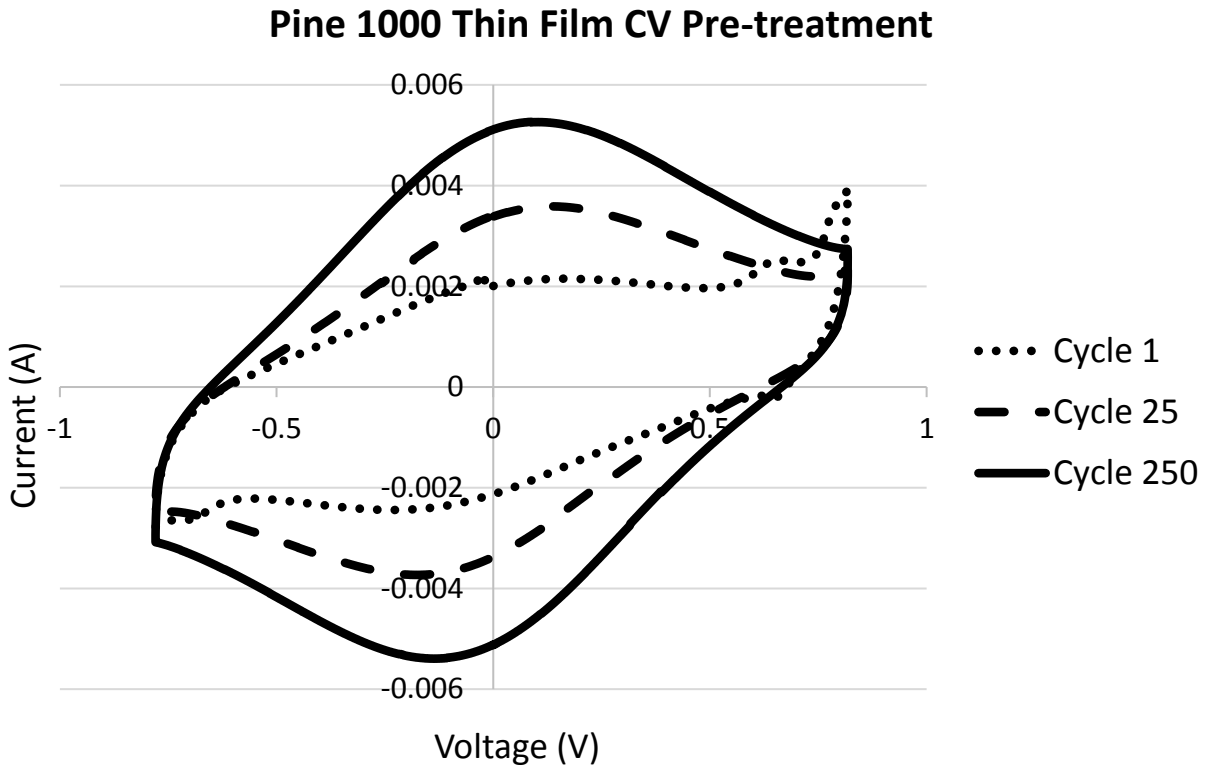
Pine 1000 Thin Film CV Pre-treatment
0.006
0.004
0.002
0
-0.002
-0.004
-0.006
-1
-0.5
0
0.5
1
Current (A)
Voltage (V)
Cycle 1
Cycle 25
Cycle 250

8.7 Appendix G: SSA Normalized Capacitance versus Current Density with Rate Capability Fitting

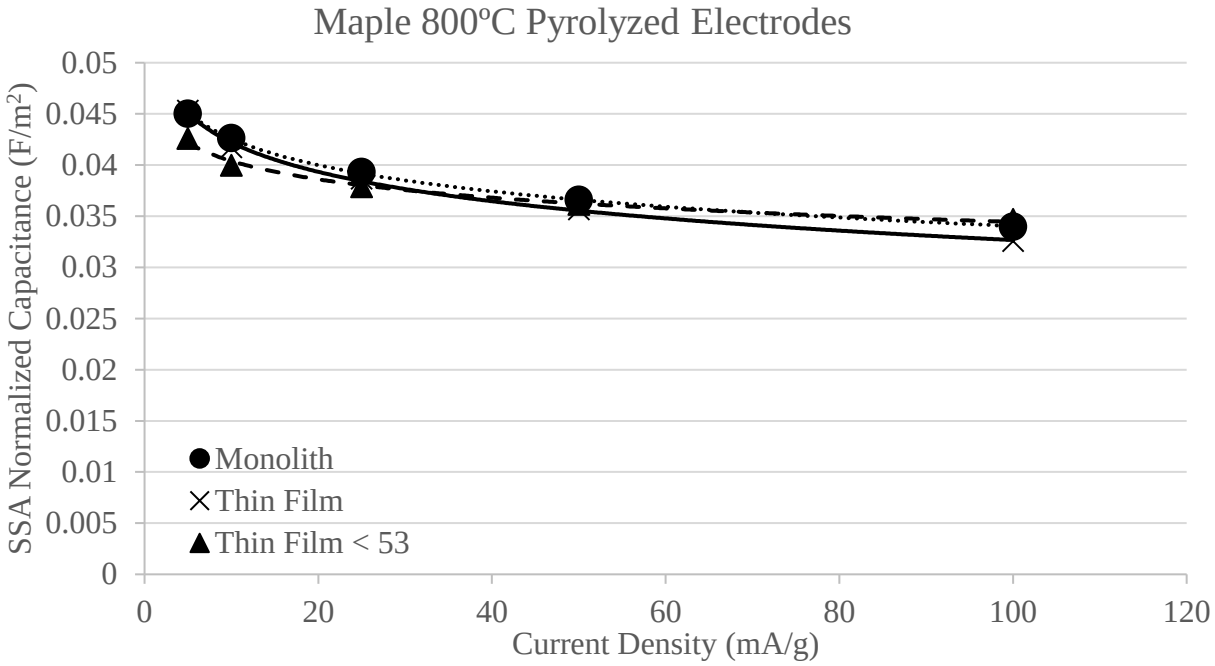

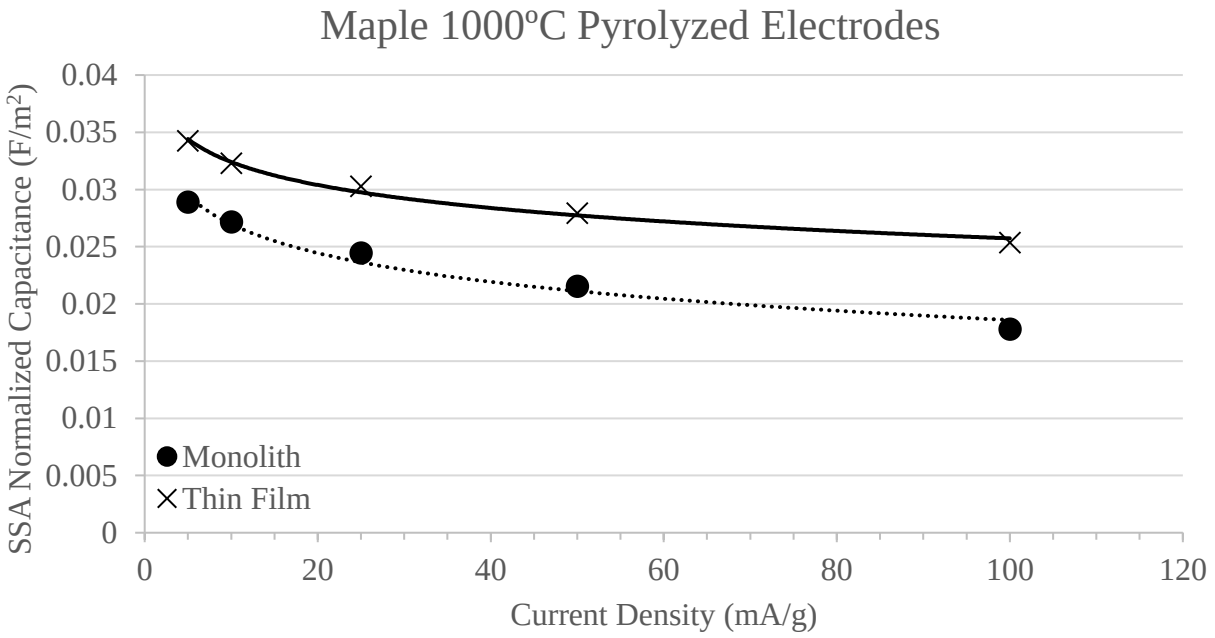

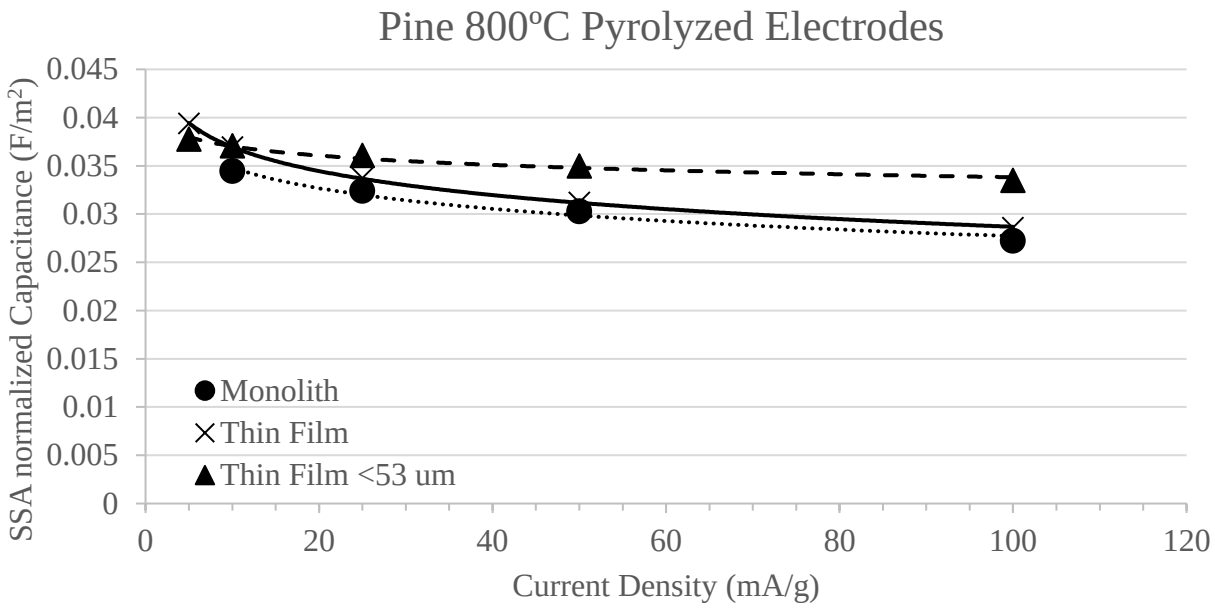
Pine 800ºC Pyrolyzed Electrodes
SSA normalized Capacitance (F/m²)
0.045
0.04
0.035
0.03
0.025
0.02
0.015
0.01
0.005
0
0
20
40
60
80
100
120
Current Density (mA/g)
Monolith
Thin Film
Thin Film <53 um

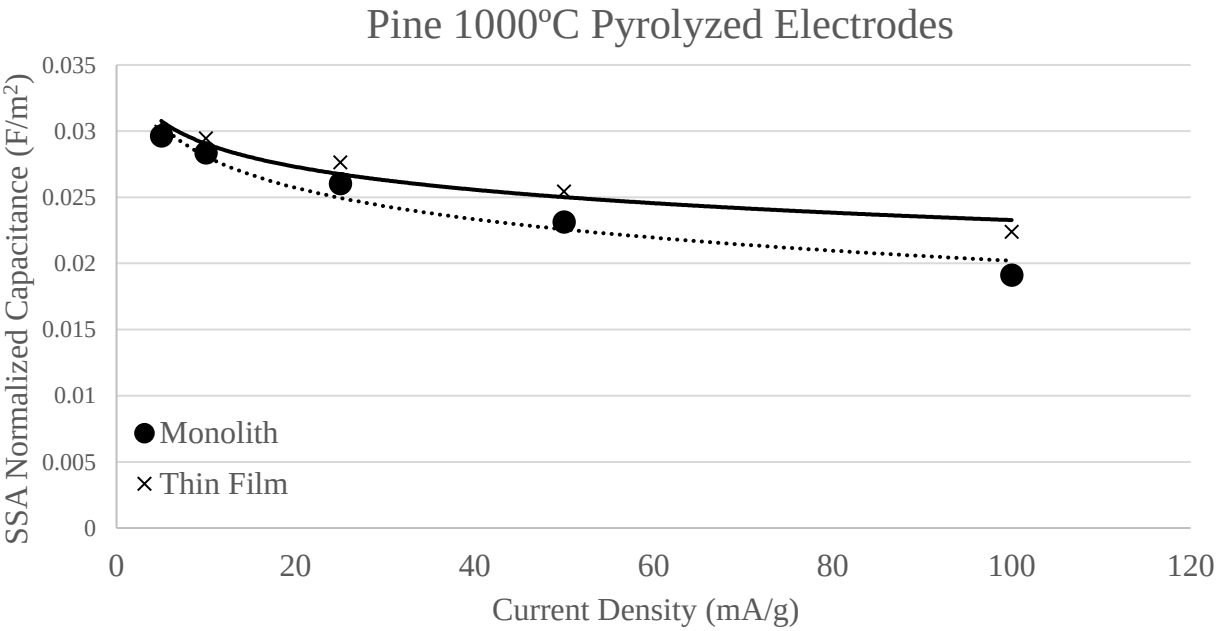
Pine 1000ºC Pyrolyzed Electrodes
SSA Normalized Capacitance (F/m²)
0.035
0.03
0.025
0.02
0.015
0.01
0.005
0
0
20
40
60
80
100
120
Current Density (mA/g)
Monolith
Thin Film

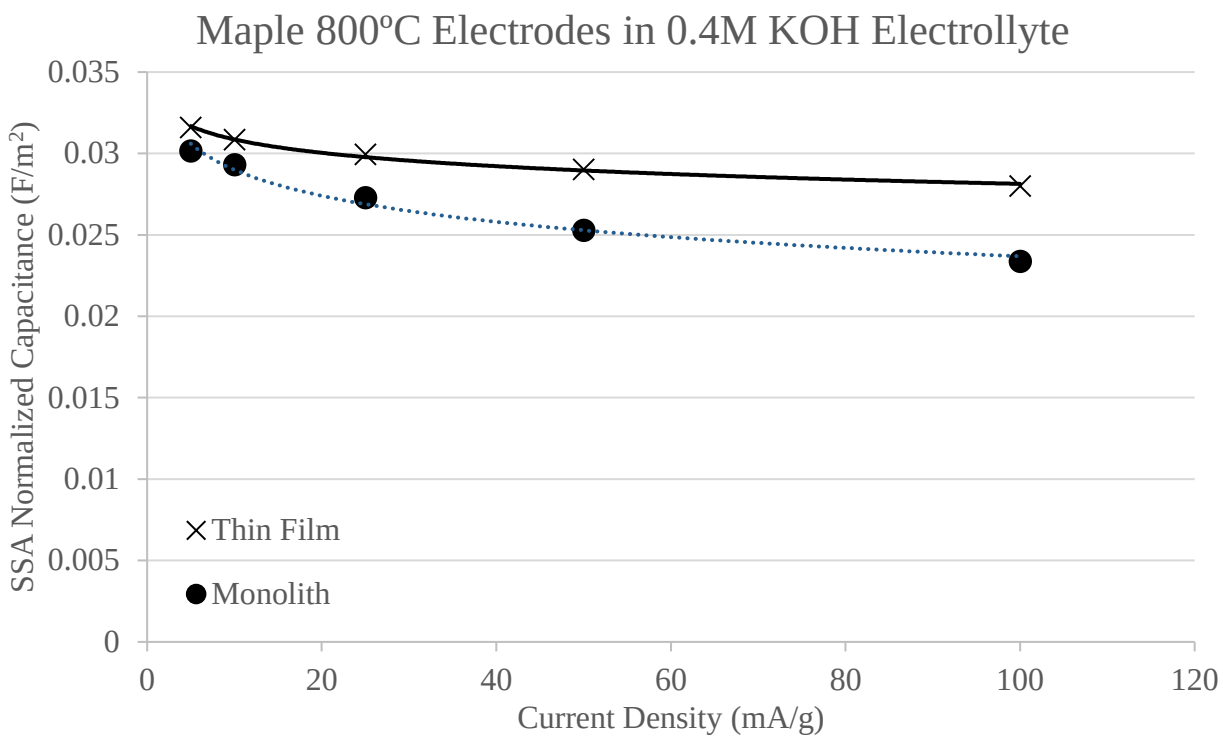
Maple 800ºC Electrodes in 0.4M KOH Electrollyte
SSA Normalized Capacitance (F/m²)
0.035
0.03
0.025
0.02
0.015
0.01
0.005
0
Thin Film
Monolith
0
20
40
60
80
100
120
Current Density (mA/g)

8.8 Appendix H: Kramers-Kronig Analysis

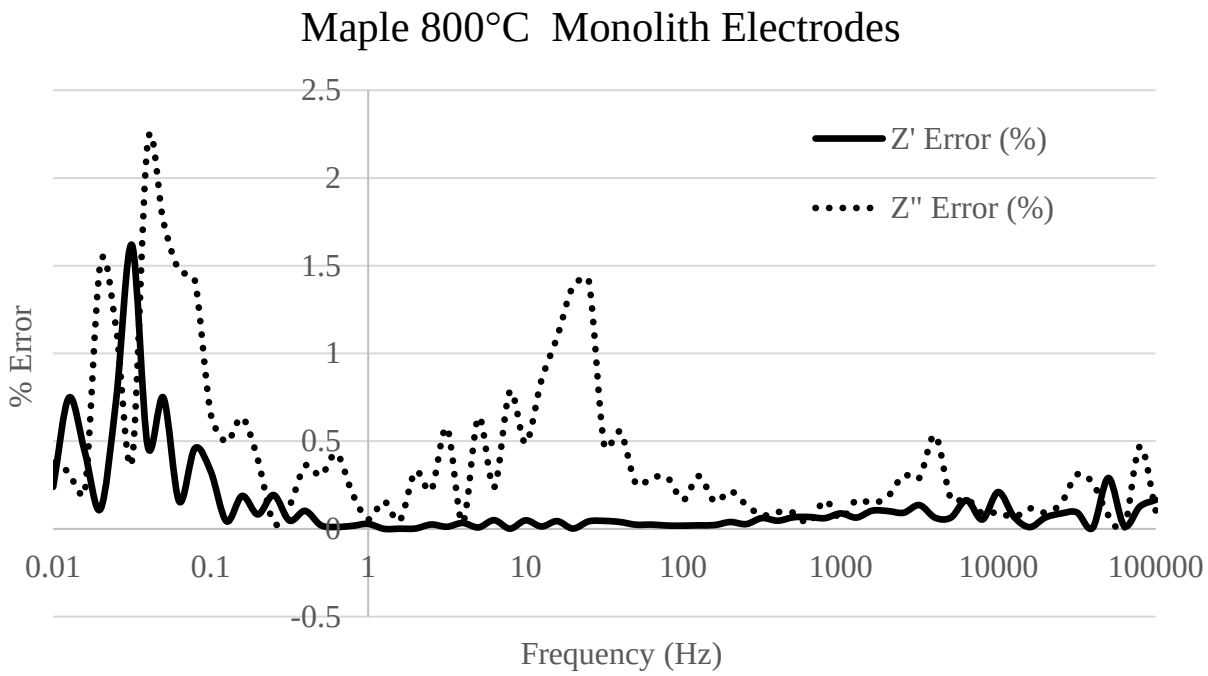

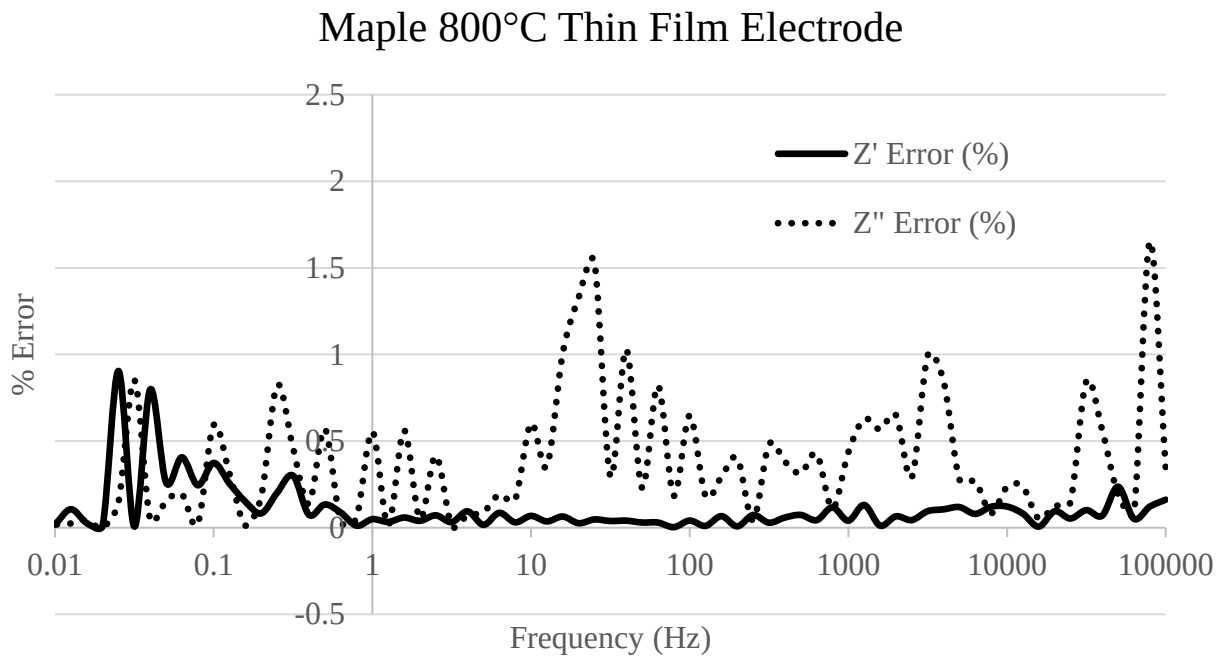

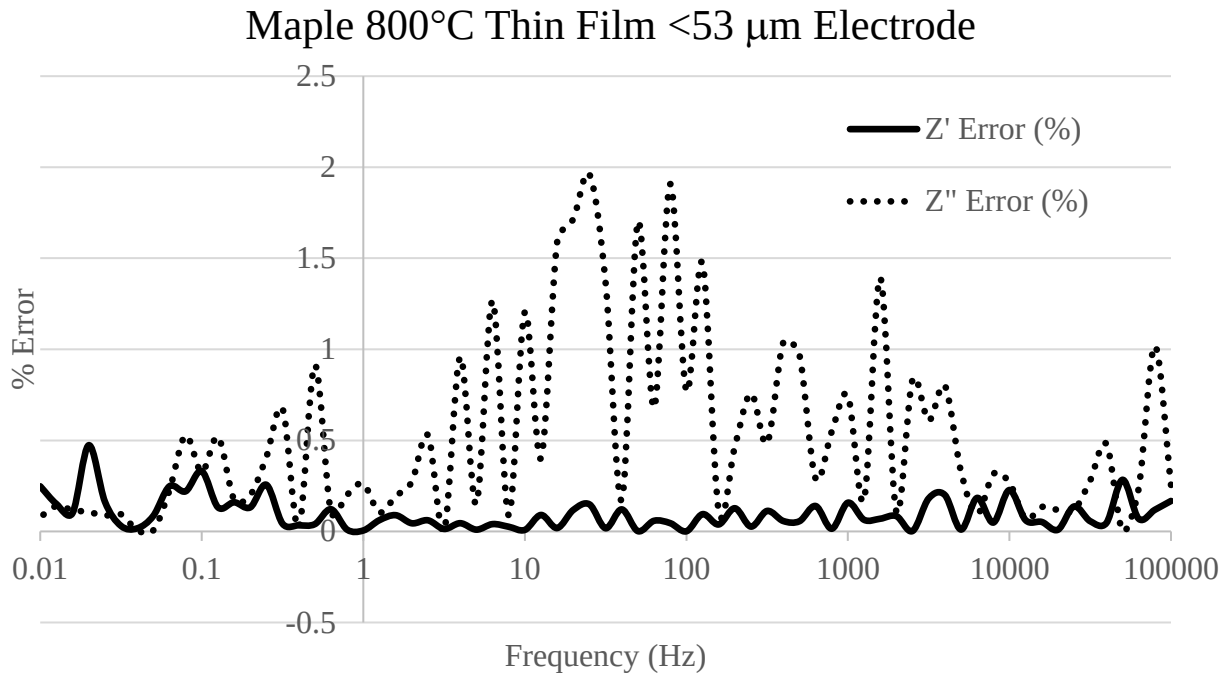
Maple 800°C Thin Film <53 μm Electrode
2.5
2
1.5
1
0.5
0
-0.5
% Error
0.01
0.1
1
10
100
1000
10000
100000
Frequency (Hz)
Z' Error (%)
Z'' Error (%)

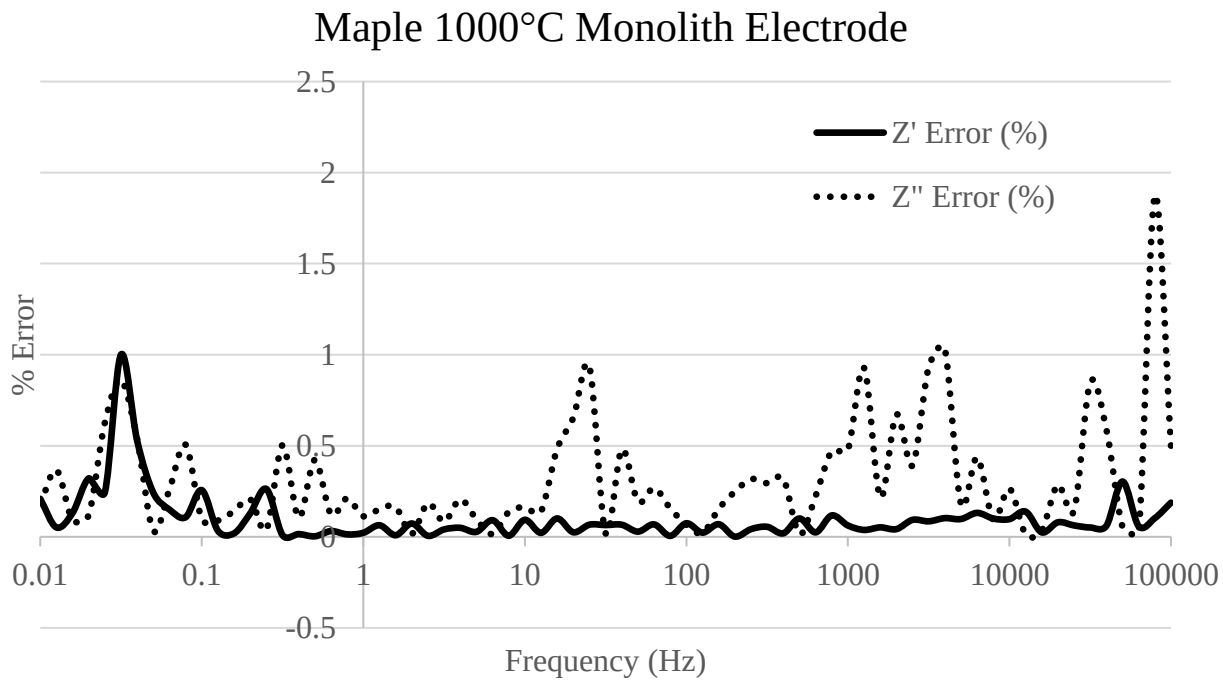
Maple 1000°C Monolith Electrode
2.5
2
1.5
1
0.5
0
-0.5
% Error
0.01
0.1
1
10
100
1000
10000
100000
Frequency (Hz)
Z' Error (%)
Z'' Error (%)

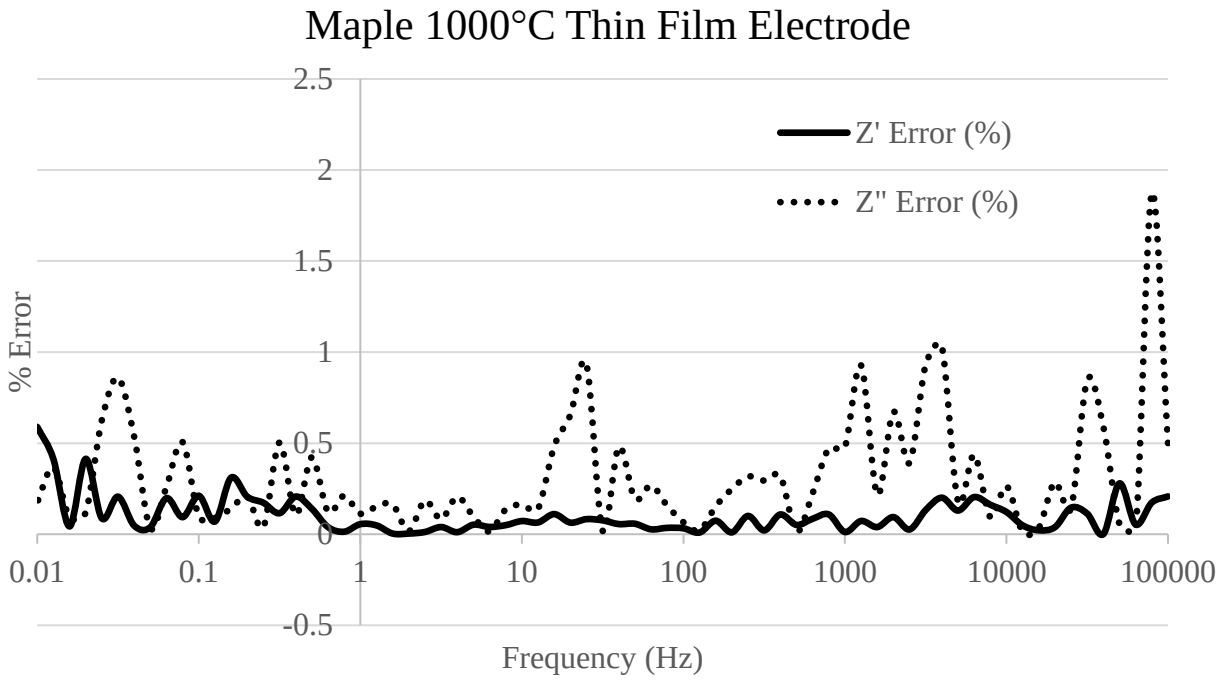
Maple 1000°C Thin Film Electrode
2.5
2
1.5
1
0.5
0
-0.5
% Error
0.01
0.1
1
10
100
1000
10000
100000
Frequency (Hz)
Z' Error (%)
Z'' Error (%)

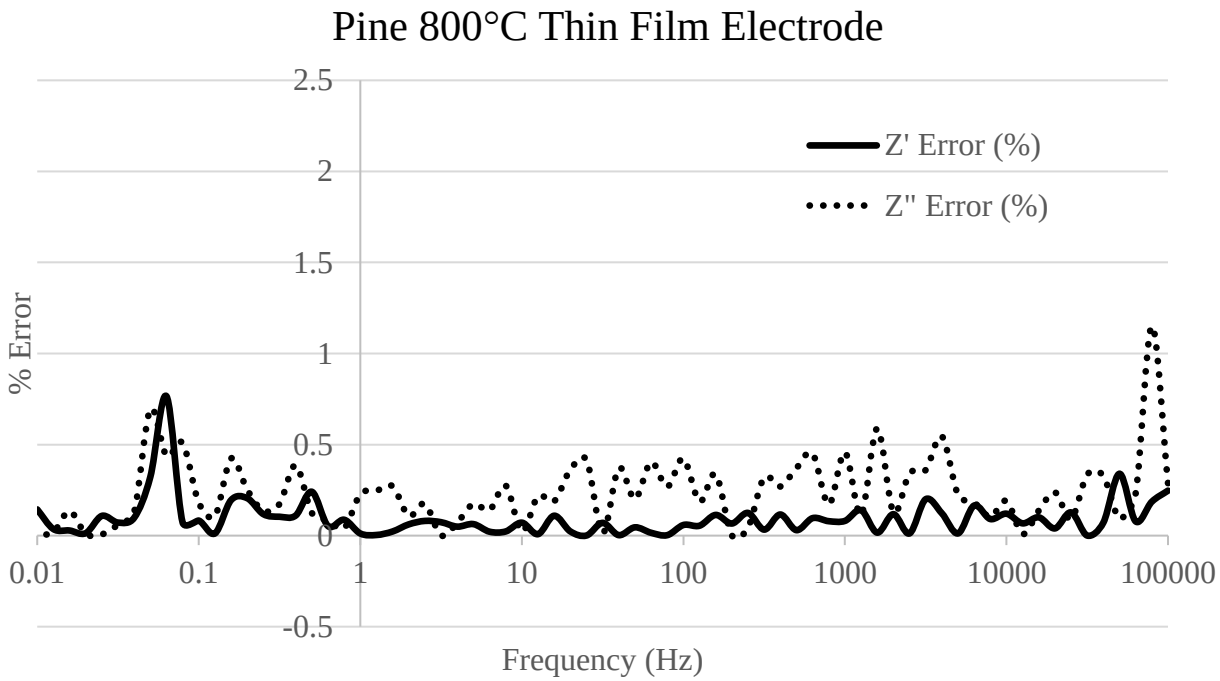
Pine 800°C Thin Film Electrode
2.5
2
1.5
1
0.5
0
-0.5
% Error
0.01
0.1
1
10
100
1000
10000
100000
Frequency (Hz)
Z' Error (%)
Z'' Error (%)

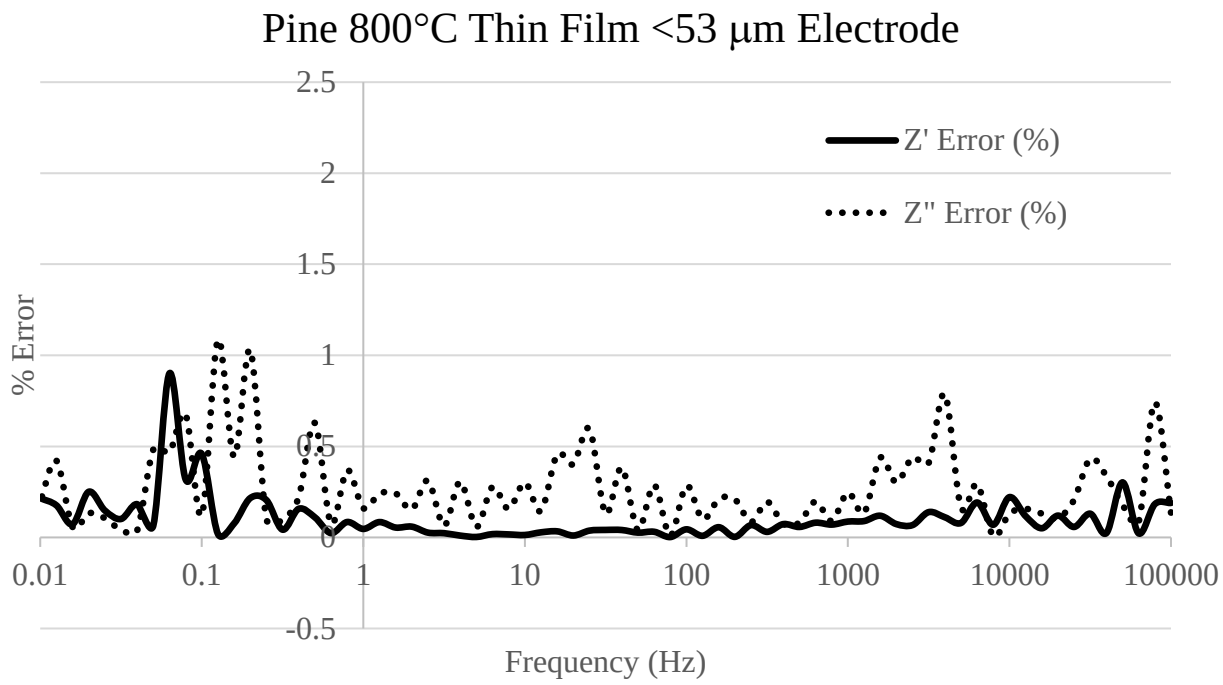
Pine 800°C Thin Film <53 μm Electrode
2.5
2
1.5
1
0.5
0
-0.5
% Error
0.01
0.1
1
10
100
1000
10000
100000
Frequency (Hz)
Z' Error (%)
Z" Error (%)

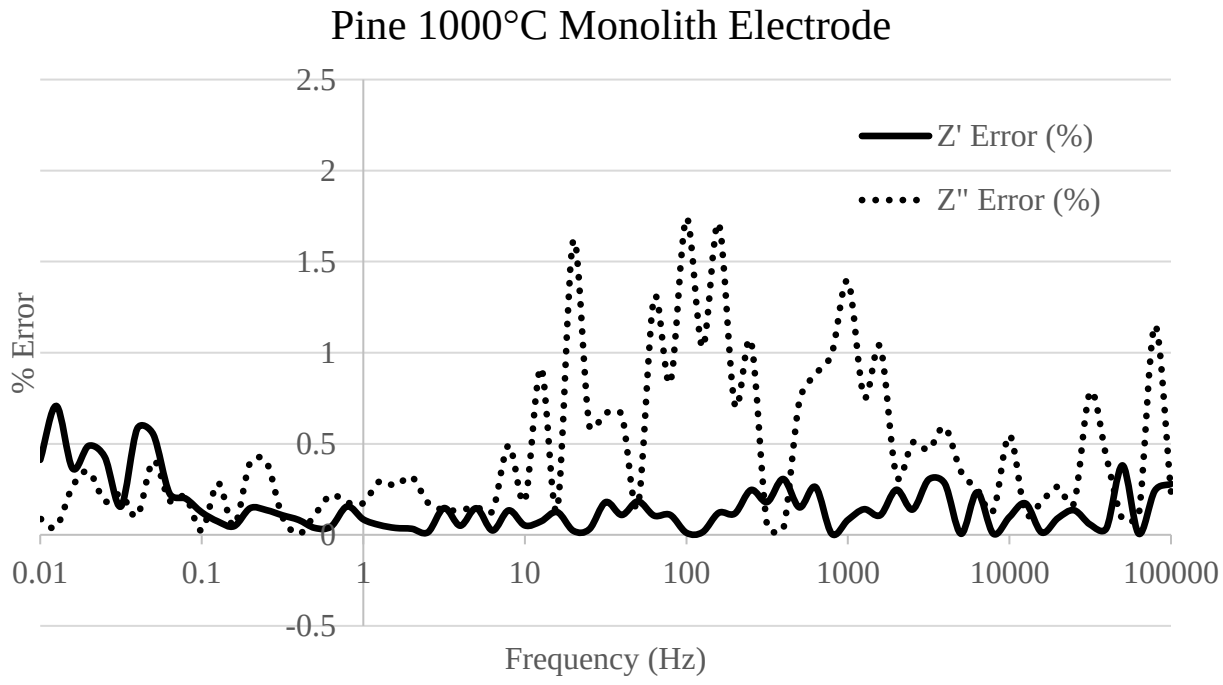
Pine 1000°C Monolith Electrode
2.5
2
1.5
1
0.5
0
-0.5
% Error
0.01
0.1
1
10
100
1000
10000
100000
Frequency (Hz)
Z' Error (%)
Z" Error (%)

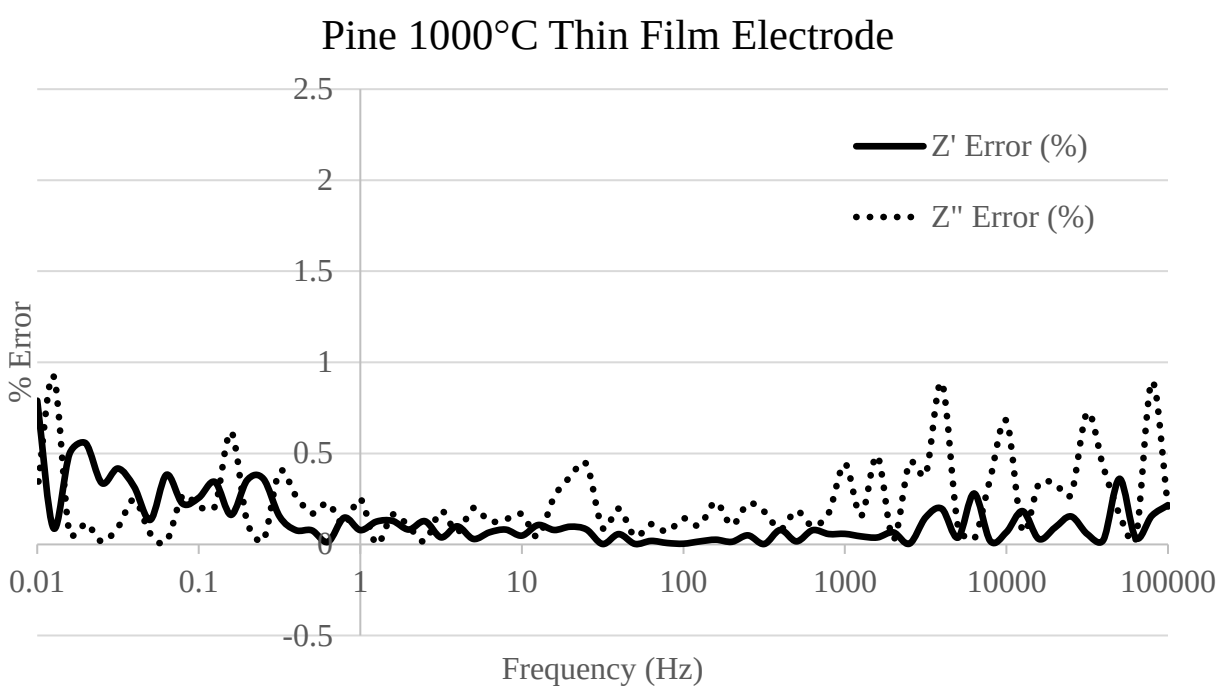
Pine 1000°C Thin Film Electrode
2.5
2
1.5
1
0.5
0
-0.5
% Error
0.01
0.1
1
10
100
1000
10000
100000
Frequency (Hz)
Z' Error (%)
Z'' Error (%)

8.9 Appendix I: Preliminary Chemical Activation Work of Monolithic Biochar

8.9.1 Introduction

Of all the carbon materials being tested for supercapacitor application, unactivated biochar ranks quite low on the performance scale. While it's low cost and potential for large monolithic electrodes are attractive features, both the specific and volumetric capacitances have to improve in order for biochar to be competitive with current commercial solutions. One way to improve these values is through chemical activation treatments.

Chemical activation of biochar for EDLC devices is conducted to achieve either of two goals. The first is to exfoliate the carbon surfaces, creating higher specific surface area and often manipulating the nanoscale pore size distribution. The second is to create different chemical surface groups, usually to take part in rapid faradaic reactions, resulting in pseudocapacitance contributions to energy storage. This chapter focuses on the first goal.

Preliminary work on the activation of monolithic commercially purchased maple biochar was conducted. Although there are not enough significant findings at this point for journal publication, the information learned will support our lab's future work and so it is documented herein.

Several studies have reported the successful activation of carbon powders from various feedstocks, including biochar, with potassium hydroxide to increase the materials' SSA [7], [28], [99]–[101]. Due to readily accessible equipment and experience, the AFC-3 sample method developed by Zuliani et al. in [99] for petroleum coke carbon powders (our lab group) was applied to monolithic biochar. Upon completion of this activation process however, the monolithic structure had broken down into a powder. Monolithic biochar faces a unique problem with these types of chemical activations: how to increase the material's SSA without losing the monolithic structure.

8.9.2 Experimental

A less aggressive procedure was developed for activation of monolithic biochar with KOH:

1. Biochar monoliths were soaked in a 4M KOH solution for at least two weeks – ideally, these porous structures are fully saturated with electrolyte.
2. The monoliths were then removed from the solution, and placed into an oven at ~110°C for 24 hours. Drying was conducted in an oven, instead of at room temperature, to speed up the process so that the electrolyte would not have time to drain out of the biochar. Ideally, KOH crystals are evenly deposited on the carbon surfaces after drying.
3. The dried biochar was then put into a tubular furnace with an inert N_2 environment (300 cm^3/min flow rate). The furnace was heated at a rate of 4°C/min up to 700°C, where the temperature was held for 60 minutes. The melting temperature of solid KOH is ~380°C.
4. The activated monolithic biochar product was then cut and shaped into electrode geometries (2mm x 7mm x 7mm, thickness x length x height) for electrochemical testing.

8.9.3 Results

The activated biochar maintained its monolithic structure with this procedure. Physisorption results showed an increase in both the N_2 and CO_2 calculated SSAs in the activated sample compared to the untreated commercial biochar (Table XIX). In addition, a plot of calculated specific capacitance values versus current density (Figure 8.1) from galvanostatic cycling measurements, shows superior total capacitance and rate capability of the activated biochar monolith electrode. SSA normalized capacitances in $\mu F/cm^2$ were calculated for both samples (Table XIX). The slightly larger value for the untreated biochar electrode indicates that the SSA difference caused by the activation process was responsible for the energy storage improvement.

Table XIX. Summary of physisorption measurements and capacitive performance for activated and unactivated commercial biochar monolithic electrodes

Biochar Electrode Material	Specific Capacitance at 5 mA/g	N_2 BET SSA (m^2/g)	CO_2 SSA (m^2/g)	Total SSA (m^2/g)	SSA Normalized Capacitance ($\mu F/cm^2$)
4M KOH Activated	30.01	188	573	761	3.94
2mm Thick Commercially Purchased	25.37	95	387	482	5.26

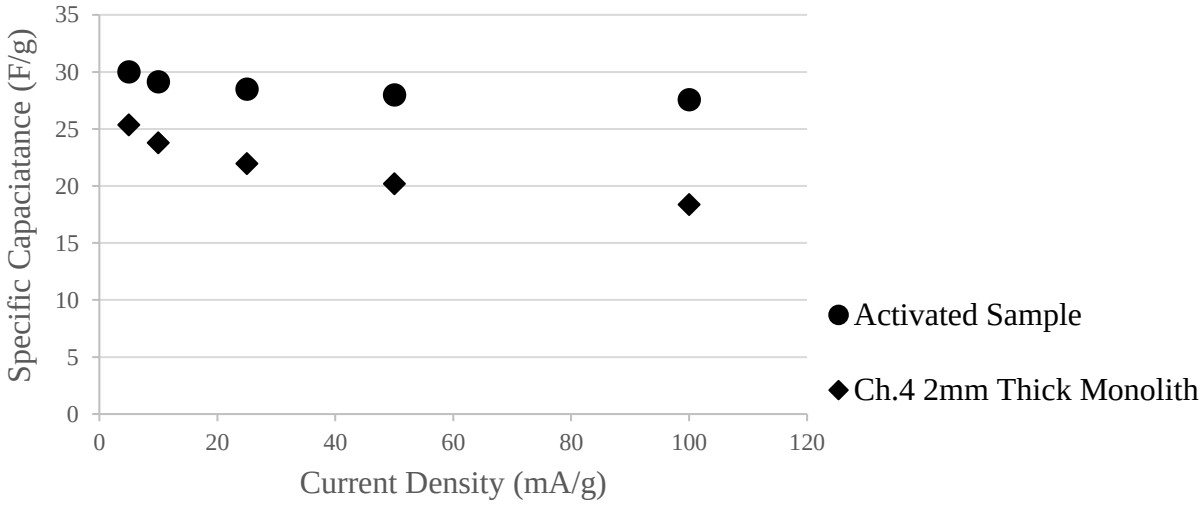

Figure 8.1. Specific capacitance comparison of KOH activated commercially purchased monolithic biochar and its controls

There was mass loss of ~20% in the product monoliths after activation, indicating the removal of some carbon, but this difference was not detected in the electrode bulk density. This means that there was likely some dimensional shrinkage of the monolithic piece in the activation process. Moving forward, this has to be more closely monitored to ensure both a specific and volumetric capacitive performance improvement.

8.9.4 Conclusions

A modest increase in the specific capacitance performance (~15%) is seen due to the applied activation process while successfully retaining the monolithic structure. However, the values

achieved are still not competitive with commercial activated carbon powders, and so there is substantial room for optimization. The ideal activation process would uniformly roughen the surface of the carbon while removing negligible amounts of mass.